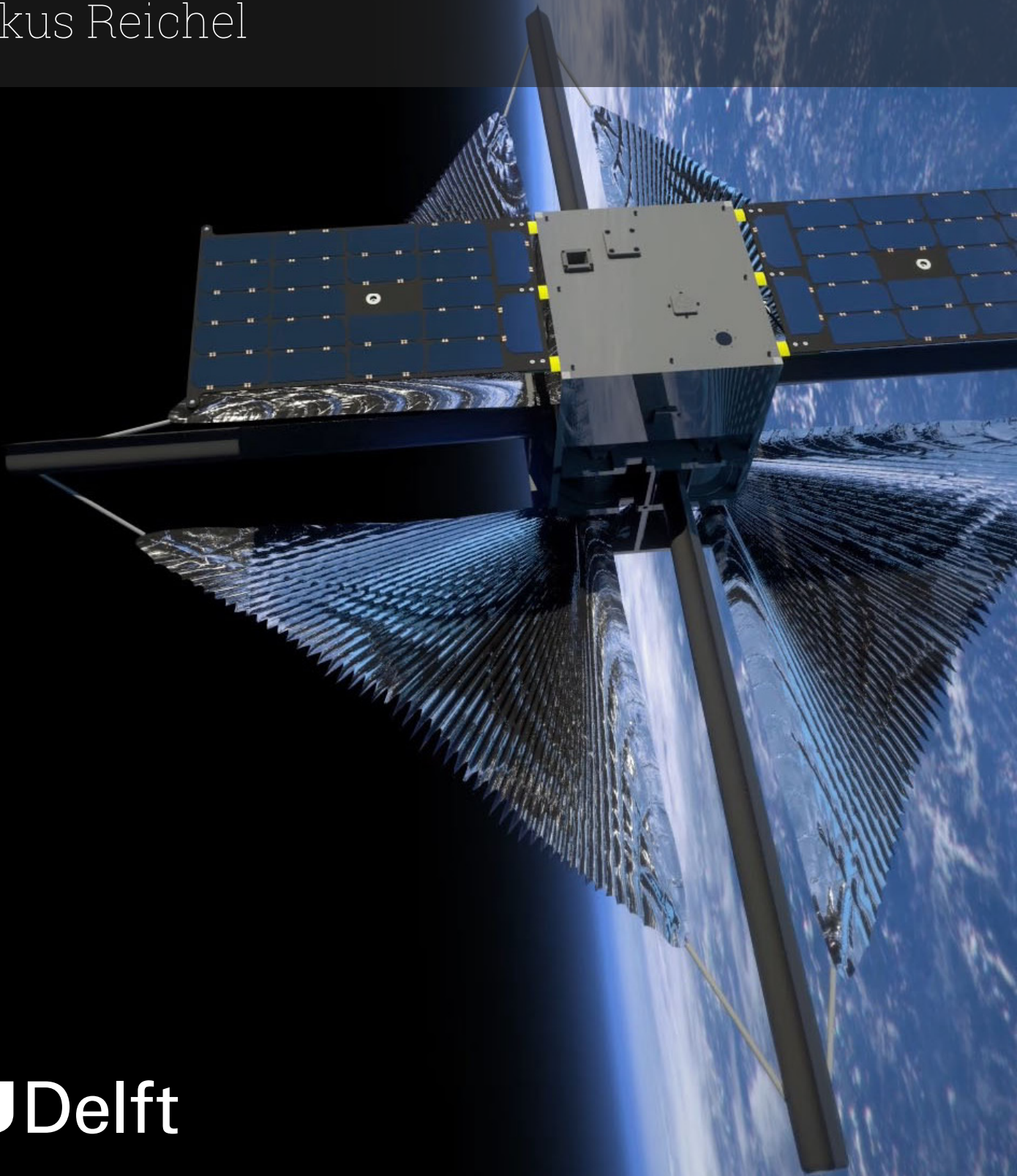


# Solar Sail Far-Range Rendezvous Operations For Active Debris Removal

Markus Reichel





# Solar Sail Far-Range Rendezvous Operations For Active Debris Removal

by

Markus Reichel

to obtain the degree of Master of Science

at the Delft University of Technology,

to be defended publicly on Friday November 29, 2024 at 13:00.

Student number: 5841348  
Project duration: February 14, 2024 – November 29, 2024  
Thesis committee: Dr. J. Guo, TU Delft, Committee chair  
Dr. ir. M.J. (Jeannette) Heiligers, TU Delft, Supervisor  
Dr. S. Gehly, TU Delft, External examiner

Cover: Advanced Composite Solar Sail System (ACS3) by NASA under  
CC BY-NC 2.0 (Modified)

An electronic version of this thesis is available at <http://repository.tudelft.nl/>.



“Don’t Panic”

*Douglas Adams*



# Preface

In this thesis, the results of nine months of dedicated research on

## **Solar Sail Far-Range Rendezvous Operations for Active Debris Removal**

are presented.

My first words are addressed to those who have always believed in me, loved me, and supported me throughout my life: my parents, Christel and Walter, and my brother André. Without you, I could not have embarked on this journey and closed this significant chapter in my life. Thank you for providing me everything I needed to be where I am today.

Next, I want to express my gratitude to the friends I made along the way, many of whom I believe will be lifelong friends. A special thanks goes to Jannis, Julius, and David, whom I am lucky to call my closest friends. Thank you for believing in me and answering my questions, which might also have been solved with a quick Google search.

Furthermore, I am grateful to Robbin, who started the Master's degree in Delft with me and whom I now can also call a true friend. I already miss our long walks around the faculty and the extensive tea breaks we shared.

Last but not least, I want to thank Bernd Dachwald, who inspired me and awakened my interest in orbital mechanics, and my supervisor, Jeannette Heiligers, for her guidance, feedback, and for sharing her knowledge throughout my thesis project. Your enthusiasm for the wonderful world of solar sails is truly contagious.

*Markus Reichel*  
*Herzogenrath, November 15, 2024*



# Summary

Space debris has become an increasingly pressing issue, exaggerated by the rapid increase in satellites sent into orbit. With it, the growing risk of collisions leads to the potential for uncontrolled proliferation of debris, which could render entire orbital regions unusable in the future. Active debris removal is the only long-term solution to stop the growth of the debris population. Solar sails may represent a sustainable method for cleaning up debris pieces due to their nearly unlimited  $\Delta V$  budget, but this would require the sail to operate in proximity to the target. However, solar-sail proximity operations have not yet been investigated in the literature. This thesis aims to address this research gap by defining the following objective:

**Contribute to a sustainable space environment by exploring the feasibility of solar-sail active debris removal missions, focusing on far-range rendezvous operations.**

A sail's inability to stay stationary with respect to a target poses an issue during proximity operations. This thesis, therefore, suggests and investigates a hold trajectory as an alternative to a classic hold point. Given the sail's inherently limited thrusting capabilities and operational constraints, it must constantly steer to remain within a dedicated hold volume, transforming the issue into an optimal control problem. To examine affect of the sail's operational limitations and safety considerations on hold trajectories, InTrance, an intelligent spacecraft trajectory optimisation tool that utilises neurocontrol evolution, was used. Furthermore, the feasibility of using InTrance to design preliminary homing trajectories for solar sails, enabling a transfer from an injection point to merge onto a hold trajectory, was assessed. The investigation resulted in the following outcomes:

1. **Feasibility of Hold Trajectories:** Hold trajectories represent a feasible alternative to classical hold points for solar sails, enabling the sail to steer continuously within a dedicated hold volume for prolonged periods. This allows for continuous observation of the target object, performance of system checks, and time to plan subsequent stages of proximity operations.
2. **Impact of Operational Constraints:** The size of the hold trajectory depends on the sail's operational constraints. Limiting the sail's cone angle requires larger hold trajectories to allow prolonged stays within hold volumes. A similar effect is observed when limiting the sail's turning rate.
3. **Optimal Hold Trajectory Location:** The safest locations for a hold trajectory are either ahead of or behind the target. This positioning allows for safe arrival from the homing trajectory and safe departure without passing by the target and risking a collision. Furthermore, this positioning of the hold trajectory can ensure that, during an emergency, the sail can simply maintain its current attitude to safely distance itself from the target at any point along the hold trajectory without drifting towards it, greatly improving safety.
4. **Limitations of InTrance for Homing Trajectories:** In its current adaptation, InTrance seems to converge to control profiles, which repeat each revolution. It is observed that with such a control profile, a seamless transition onto a hold trajectory is not possible. Thus, InTrance cannot generate feasible homing trajectories for solar sails in its current form.

While this work demonstrated that observing a piece of space debris for an extended period with a solar sail is possible, much research remains to fill the gap in solar-sail proximity operations. A key recommendation is to improve the safety associated with hold trajectories by investigating inclined trajectories, which could also allow for better target observation. Additionally, a deeper investigation into homing trajectories is necessary to bridge the phasing phase of proximity operations with hold trajectories. Advancing solar-sail proximity operations could lead to a sustainable way to keep Earth's orbits free from debris in the future.

# Zusammenfassung

Weltraumschrott ist in der Raumfahrt wegen der stetig steigenden Anzahl der in die Umlaufbahn gebrachten Satelliten in immer dringlicheres Problem geworden. Mit ihrer Anzahl steigt auch die Gefahr von Kollisionen. Aktive Entfernung von Weltraumschrott (Active Debris Removal) ist die einzige langfristige Lösung, um das Wachstum der Trümmerpopulation zu stoppen. Sonnensegel könnten aufgrund ihres nahezu unbegrenzten  $\Delta V$ -Budgets eine nachhaltige Methode zur Beseitigung von Weltraumschrott darstellen, aber dies würde erfordern, dass das Segel in der unmittelbaren Nähe des Ziels operiert. Allerdings wurden Sonnensegel-Näherungsoperationen in der Literatur noch nicht thematisiert. Diese Arbeit zielt darauf ab, diese Forschungslücke zu schließen, indem sie das folgende Ziel definiert:

**Durch die Erforschung der Machbarkeit von aktiven Weltraumschrottbeseitigungsmissionen mit Sonnensegeln, mit Fokus auf Fern-Rendezvous-Operationen, zu einer nachhaltigen Weltraumumgebung beitragen.**

Das Handicap eines Segels, relativ zu einem Ziel stationär zu bleiben, stellt bei Näherungsoperationen ein Problem dar. Diese Arbeit schlägt daher eine Haltebahn als Alternative zu einem klassischen Haltepunkt vor und untersucht sie. Angesichts der von Natur aus begrenzten Schubfähigkeiten und operativen Einschränkungen des Segels muss es ständig steuern, um innerhalb eines dedizierten Haltebereichs zu bleiben, wodurch das Problem in ein Optimierungsproblem der optimalen Steuerung umgewandelt wird. InTrance, ein intelligentes Werkzeug zur Optimierung von Raumfahrzeugtrajektorien, das Neurokontroll-Evolution verwendet, wurde angepasst, um den Einfluss der operativen Einschränkungen des Segels und Sicherheitsüberlegungen auf Haltebahnen zu untersuchen. Darüber hinaus wurde die Machbarkeit der Verwendung von InTrance zur Gestaltung vorläufiger Homing-Trajektorien für Sonnensegel bewertet, die einen Transfer von einem Einspeisepunkt ermöglichen, um auf eine Haltebahn zu gelangen. Die Untersuchung ergab folgende Ergebnisse:

1. **Machbarkeit von Haltebahnen:** Haltebahnen stellen eine machbare Alternative zu klassischen Haltepunkten für Sonnensegel dar, die es dem Segel ermöglichen, über längere Zeiträume kontinuierlich innerhalb eines dedizierten Haltebereichs zu steuern. Dies ermöglicht eine kontinuierliche Beobachtung des Zielobjekts, die Durchführung von Systemüberprüfungen und Zeit, um die nächsten Phasen der Näherungsoperationen zu planen.
2. **Auswirkung operativer Einschränkungen:** Die Größe der Haltebahn hängt von den operativen Einschränkungen des Segels ab. Die Begrenzung des Kegelwinkels des Segels erfordert größere Haltebereiche, um längere Aufenthalte innerhalb des Bereichs zu ermöglichen. Ein ähnlicher Effekt wird beobachtet, wenn die Drehgeschwindigkeit des Segels begrenzt wird.
3. **Optimale Position der Haltebahn:** Die sichersten Positionen für eine Haltebahn liegen entweder vor oder hinter dem Ziel. Diese Platzierung ermöglicht eine sichere Ankunft von der Homing-Trajektorie und einen sicheren Abflug, ohne am Ziel vorbeizufiegen und eine Kollision zu riskieren. Darüber hinaus kann diese Platzierung der Haltebahn sicherstellen, dass das Segel im Notfall

einfach seine aktuelle Ausrichtung beibehalten kann, um sich sicher vom Ziel zu entfernen, ohne sich ihm anzunähern, was die Sicherheit erheblich verbessert.

4. **Einschränkungen von InTrance für Homing-Trajektorien:** In seiner aktuellen Version scheint InTrance zu Steuerprofilen zu konvergieren, die sich in jeder Umdrehung wiederholen. Es wird beobachtet, dass mit einem solchen Steuerprofil ein nahtloser Übergang auf eine Haltebahn nicht möglich ist. Daher kann InTrance in seiner jetzigen Form keine machbaren Homing-Trajektorien für Sonnensegel generieren.

Obwohl diese Arbeit gezeigt hat, dass es möglich ist, ein Stück Weltraumschrott über einen längeren Zeitraum mit einem Sonnensegel zu beobachten, bleibt noch viel Forschung, um die Lücke in den Sonnensegel-Näherungsoperationen zu schließen. Eine wichtige Empfehlung ist, die mit Haltebahnen verbundene Sicherheit zu verbessern, indem geneigte Bahnen untersucht werden, die auch eine bessere Zielbeobachtung ermöglichen könnten. Außerdem ist eine tiefere Untersuchung von Homing-Trajektorien notwendig, um die "phasing" Phase der Näherungsoperationen mit Haltebahnen zu überbrücken. Die Weiterentwicklung von Sonnensegel-Näherungsoperationen könnte in Zukunft zu einer nachhaltigen Methode führen, um den erdnahen Weltraum um die Erde frei von Trümmern zu halten.

# Contents

<b>Preface</b>	<b>iii</b>
<b>Summary</b>	<b>v</b>
<b>List of Figures</b>	<b>xi</b>
<b>List of Tables</b>	<b>xv</b>
<b>Nomenclature</b>	<b>xvi</b>
<b>1 Introduction</b>	<b>1</b>
1.1 Research Objective and Questions . . . . .	2
1.2 Thesis Outline . . . . .	3
<b>2 Methodology</b>	<b>4</b>
2.1 Solar-Sail Model . . . . .	4
2.1.1 Ideal Solar-Sail Model . . . . .	4
2.1.2 Locally Optimal Steering . . . . .	6
2.1.3 Constrained Optimal Steering . . . . .	7
2.2 Proximity Operations . . . . .	9
2.2.1 Reference Frames . . . . .	9
2.2.2 Phases of a Rendezvous Mission . . . . .	10
2.2.3 Solar-Sail Far-Range Rendezvous Operations . . . . .	12
2.2.4 Equation of Motion . . . . .	14
2.2.5 Environmental Model . . . . .	15
2.3 Trajectory Optimisation Using InTrance . . . . .	16
2.3.1 Artificial Neural Networks . . . . .	16
2.3.2 Spacecraft Steering Using a Neurocontroller . . . . .	18
2.3.3 Neurocontroller Fitness Assignment . . . . .	19
2.3.4 Evolutionary Algorithms . . . . .	22
2.3.5 Evolutionary Neurocontrol . . . . .	23
2.4 Simulation and Optimisation Setup . . . . .	26
<b>3 Characteristics of Solar Sail Relative Motion</b>	<b>27</b>
3.1 Test Case . . . . .	28
3.2 Initial True Anomaly Analysis . . . . .	31
3.3 Cone Angle Analysis . . . . .	35
3.3.1 Positive Clock Angle . . . . .	36
3.3.2 Negative Clock Angle . . . . .	37
3.4 Discussion . . . . .	38

<b>4</b>	<b>Hold Trajectory Analysis</b>	<b>42</b>
4.1	Experiment Setup . . . . .	42
4.2	Encircling Hold Trajectories . . . . .	44
4.2.1	Test Case . . . . .	44
4.2.2	Cone Angle Constraints . . . . .	47
4.2.3	Turning Rate Constraints . . . . .	49
4.3	Leading/Trailing Hold Trajectories . . . . .	50
4.3.1	Test Case . . . . .	51
4.3.2	Cone Angle Constraints . . . . .	52
4.3.3	Turning Rate Constraints . . . . .	54
4.3.4	Clock Angle Constraints . . . . .	55
4.3.5	Combined Constraints . . . . .	59
4.4	Safety Assessment . . . . .	61
4.5	Discussion . . . . .	62
<b>5</b>	<b>Homing Trajectory Analysis</b>	<b>67</b>
5.1	Homing Trajectory Optimisation . . . . .	67
5.2	Hold Trajectory Optimisation . . . . .	71
5.3	Discussion . . . . .	72
<b>6</b>	<b>Conclusion and Recommendations</b>	<b>75</b>
6.1	Conclusion . . . . .	75
6.2	Recommendations . . . . .	77
	<b>Bibliography</b>	<b>81</b>
<b>A</b>	<b>Verification and Validation</b>	<b>85</b>
A.1	Coordinate Transformations . . . . .	85
A.2	Force Model . . . . .	86
A.3	Cylindrical Shadow Model . . . . .	87
A.4	Locally Optimal Steering . . . . .	88
A.5	Trajectory Optimisation . . . . .	88
A.6	Accuracy Assessment and Step Size Selection for CW Equations . . . . .	93
A.7	Runtime Efficiency Comparison of Propagation Methods . . . . .	94
<b>B</b>	<b>InTrance</b>	<b>95</b>
B.1	InTrance Configuration . . . . .	95
B.2	Evolutionary Algorithm Configuration . . . . .	95
B.3	Neurocontroller Configuration . . . . .	96
B.4	Simulation Configuration . . . . .	96
B.5	Spacecraft Configuration . . . . .	97
<b>C</b>	<b>Additional Figures and Tables</b>	<b>98</b>
C.1	Characteristics of Solar Sail Relative Motion . . . . .	98
C.2	Hold Trajectory Analysis . . . . .	98
C.3	Homing Trajectory Analysis . . . . .	98

# List of Figures

1	Sail control angles in Sun-sail line reference frame (Macdonald & McInnes, 2005). . . . .	5
2	SRP force on a perfectly reflecting solar sail. Adapted from Dachwald (2005) by changing parameter designations. . . . .	5
3	Solar-Sail Force Bubble and Locally Optimal Steering. . . . .	6
4	Frame $M$ attached to target $T$ , from which the chaser $C$ is observed, relative to the frame $I$ . Adapted from Curtis (2013) by changing axis labelling. . . . .	10
5	Main phases of a rendezvous mission (Fehse, 2003) . . . . .	10
6	Transfer from phasing orbit to rendezvous drift orbit. Adapted from Fehse (2003) by changing axis labelling. . . . .	11
7	Encircling and leading/trailing hold volumes . . . . .	13
8	Target volume for hold-trajectory optimisation . . . . .	14
9	Layered feed-forward artificial neural network . . . . .	17
10	NC for direct steering of a solar-sailcraft . . . . .	19
11	Evolutionary Operators Implemented in InTrance (Dachwald, 2005) . . . . .	23
12	Trajectory Optimisation Using Evolutionary Neurocontrol . . . . .	24
13	Mapping of an ANN on a (real-value) string (Dachwald, 2005) . . . . .	24
14	One-at-a-time reproduction with tournament selection (Dachwald, 2005) . . . . .	25
15	Real Delta Coding (Dachwald, 2005) . . . . .	25
16	Trajectory of the chaser for the test case in the GEI frame, highlighting different trajectory sections for discussion. . . . .	28
17	Trajectory of the chaser for the test case in the co-moving frame, highlighting different trajectory sections for discussion: a) beginning of the movement; b) 1.5 Revolutions; c) 10 revolutions. . . . .	29
18	a) altitude and b) orbital velocity for the test case, highlighting different sections for discussion. . . . .	30
19	Eccentricity of the trajectory of the test case, highlighting different sections for discussion. . . . .	30
20	Orbital energy of the chaser of the test case, highlighting different sections for discussion. . . . .	31
21	Initial positions of the chaser for investigating the impact of different true anomalies on the relative motion of a solar sail. . . . .	32
22	Relative motion of a solar sail for different initial true anomaly values. . . . .	32
23	Trajectory of the chaser for $\theta_0 = 120^\circ$ case in the GEI frame, highlighting different trajectory sections for discussion. . . . .	33
24	Trajectory of the chaser for case $\theta_0 = 120^\circ$ in the co-moving frame, highlighting different trajectory sections for discussion: a) beginning of the movement; b) 1.5 Revolutions; c) 10 revolutions. . . . .	34
25	Orbital energy of the chaser of the test case, highlighting different sections for discussion. . . . .	34
26	Relative motion of a solar sail for various cone angles for a constant clock angle of $\delta = 90^\circ$ . . . . .	36

27	Trajectory for a constant sail attitude with $\delta = 90^\circ$ , highlighting the part where the acceleration vector has a component opposing the velocity vector and where it aligns with the velocity vector for a) $\alpha = 0^\circ$ ; b) $\alpha = 30^\circ$ . . . . .	37
28	Orbital Energy of a solar sail with a constant sail attitude of $\alpha = 30^\circ$ and $\delta = 90^\circ$ and a starting location of $\theta_0 = 0^\circ$ . . . . .	37
29	Relative motion of a solar sail with a constant cone and clock angle of $\alpha = 10^\circ$ and $\delta = 90^\circ$ , respectively, for increasing $\theta_0$ . . . . .	38
30	Relative motion of a solar sail for various cone angles for a constant clock angle of $\delta = -90^\circ$ .	39
31	Relative motion of a solar sail with a constant cone and clock angle of $\alpha = 10^\circ$ and $\delta = -90^\circ$ , respectively, for increasing $\theta_0$ . . . . .	40
32	Optimised trajectory of test case for encircling hold trajectory in the co-moving frame. .	45
33	Optimised control profile of test case for encircling hold trajectory over one orbital revolution. . . . .	46
34	Optimised trajectory of test case for encircling hold trajectory in the GEI frame with parts of the trajectory highlighted for discussion. . . . .	46
35	Change of semi-major of the optimised trajectory of test case for encircling hold trajectory.	47
36	a) Optimised control profile and b) differences in semi-major axis relative to initial values for maximum cone angles of $\alpha_{\max} = 60^\circ$ , $70^\circ$ and $85^\circ$ for Case 7, as shown in Table 4 .	48
37	Optimised trajectory in a) inertial and b) co-moving frame for maximum cone angles of $\alpha_{\max} = 60^\circ$ for Case 7, as shown in Table 4 . . . . .	49
38	Optimised trajectory of test case for leading/trailing hold trajectories in the co-moving frame. . . . .	51
39	Optimised control profile of test case for leading/trailing hold trajectories over one orbital revolution. . . . .	52
40	Optimised hold trajectories for maximum cone angles of $\alpha_{\max} = 60^\circ$ , $70^\circ$ and $85^\circ$ for Case 6, as shown in Table 4 . . . . .	53
41	Sail control angles for optimised hold trajectories for maximum cone angles of $\alpha_{\max} = 60^\circ$ , $70^\circ$ and $85^\circ$ for Case 6, as shown in Table 4 . . . . .	53
42	Eccentricity for optimised hold trajectories for maximum cone angles of $\alpha_{\max} = 60^\circ$ and $70^\circ$ for Case 6, as shown in Table 4 . . . . .	54
43	Difference in semi-major axis compared to target orbit for optimised hold trajectories for maximum cone angles of $\alpha_{\max} = 60^\circ$ and $70^\circ$ for Case 6, as shown in Table 4 . . . . .	54
44	(a): Optimised hold trajectory and (b): corresponding sail control angles for turning rate restrictions of $\Omega_{\max} = 0.1^\circ/\text{s}$ and $0.5^\circ/\text{s}$ and the unrestricted turning rate for case 7, as shown in Table 4 . . . . .	56
45	(a): Optimised hold trajectory and (b): corresponding sail control angles for positive clock angle restriction for maximum cone angles of $\alpha_{\max} = 60^\circ$ , $70^\circ$ and $85^\circ$ for case 1, as shown in Table 4 . . . . .	57
46	Difference in the semi-major axis compared to target orbit for maximum cone angles of $\alpha_{\max} = 60^\circ$ , $70^\circ$ and $85^\circ$ for Case 1, as shown in Table 4 . . . . .	58
47	(a): Optimised hold trajectory and (b): corresponding sail control angles for negative clock angle restriction for maximum cone angles of $\alpha_{\max} = 65^\circ$ , $75^\circ$ and $85^\circ$ for case 1, as shown in Table 4. . . . .	59

48	(a): Optimised hold trajectory and (b): corresponding sail control angles for combined constraints for maximum turning rates of $\Omega_{\max} = 2.0^\circ/\text{s}$ , $0.5^\circ/\text{s}$ and $0.1^\circ/\text{s}$ for Case 2, as shown in Table 9. . . . .	60
49	Difference in the semi-major axis compared to target orbit for $\Omega_{\max} = 2.0^\circ/\text{s}$ , $0.5^\circ/\text{s}$ and $0.1^\circ/\text{s}$ for Case 2, as shown in Table 9. . . . .	60
50	Eccentricity for optimised hold trajectories for $\Omega_{\max} = 2.0^\circ/\text{s}$ , $0.5^\circ/\text{s}$ and $0.1^\circ/\text{s}$ for Case 2, as shown in Table 9. . . . .	61
51	Trajectories to optimally a) raise and b) lower the semi-major axis for encircling hold trajectories. . . . .	62
52	Safety analysis of sail trajectories with a constant sail attitude over 40 revolutions starting from the hold trajectory of case 1 with $\alpha_{\max} = 70^\circ$ and a positive clock angle. Initial states are shown in Table C2 . . . . .	63
53	Safety analysis of sail trajectories with a constant sail attitude over 40 revolutions starting from the hold trajectory of case 1 with $\alpha_{\max} = 70^\circ$ and a negative clock angle. Initial states are shown in Table C3 . . . . .	63
54	Line of sight on the target for trailing hold volumes. . . . .	64
55	Homing trajectory in the co-moving frame. . . . .	69
56	Repeating control profile for homing trajectory. . . . .	70
57	Homing trajectory, with sections of it highlighted for discussion, in the GEI frame, including the SRP acceleration acting on the sail. . . . .	70
58	Change in the semi-major axis of optimised homing trajectory, obtained with Seed 2 for the first three revolutions. . . . .	71
59	Optimised hold trajectory in the co-moving frame, starting from the final state of the homing trajectory obtained with Seed 2. . . . .	71
60	Sail control angles over time for the optimised hold trajectory starting from the final state of the homing trajectory obtained with seed 2. . . . .	72
61	Change in the semi-major axis of optimised hold trajectory, starting from the final state of the homing trajectory obtained with Seed 2 (see Table 12). . . . .	72
62	Encircling and leading/trailing hold volumes . . . . .	76
A1	Comparing the propagation of an initial condition for results originating from a) thesis work b) (Curtis, 2013) . . . . .	86
A2	Verification of co-moving position of the new force model. . . . .	86
A3	Verification of co-moving velocity of the new force model. . . . .	87
A4	Keplerian orbit around Earth for Verification of Shadow Model . . . . .	87
A5	Acceleration components in the direction of a) $\hat{\lambda} = [1, -5]$ and b) $\hat{\lambda} = [-5, 3]$ and their respective optimal cone angles . . . . .	88
A6	Comparing the a) optimal control profile for an optimal semi-major axis raising trajectory to b) the control optimised by InTrance . . . . .	89
A7	Resulting sail attitude of hold trajectory for verification . . . . .	89
A8	Position difference $\ \Delta\mathbf{r}\ $ between the 2-body and Clohessy-Wiltshire propagations over 4 orbital revolutions for different step sizes. . . . .	93
A9	Average runtime comparison between the RK45 integrator for two-body dynamics and the Clohessy-Wiltshire (CW) equations across various step sizes. . . . .	94

---

C1	Trajectory for a constant sail attitude with $\delta = -90^\circ$ , highlighting the part where the acceleration vector has a component opposing the velocity vector and where it aligns with the velocity vector for a) $\alpha = 30^\circ$ ; b) $\alpha = 60^\circ$ . . . . .	98
C2	Change of semi-major of the optimised trajectory of test case for leading/trailing hold trajectory. . . . .	99
C3	Optimised control profile of test case for encircling hold trajectory. . . . .	99
C4	Change of semi-major of the optimised trajectory or negative clock angle restriction for maximum cone angles of $\alpha_{\max} = 65^\circ$ , $75^\circ$ and $85^\circ$ for case 1, as shown in Table 4. . . . .	99
C5	Trajectories for a constant sail attitude with the initial state laying on the hold trajectory, as shown in Table C1 . . . . .	100

# List of Tables

1	Constraint conditions for hold trajectory optimisation. . . . .	43
2	Cases for the Analysis of Encircling Hold Trajectory . . . . .	45
3	Number of revolutions sail spends inside hold volume with cone angle constraint. . . . .	48
4	Test cases for encircling hold trajectory analysis . . . . .	50
5	Number of revolutions sail spends inside hold volume with cone angle constraint. . . . .	52
6	Number of revolutions sail spends inside hold volume with turning rate constraint for a maximum allowable cone angle of $\alpha_{\max} = 70^\circ$ . . . . .	55
7	Number of revolutions sail stays inside target area with cone angle constraint for a clock angle $\delta \in (1; 179)$ . . . . .	56
8	Number of Revolutions sail Spends Inside Target Area With Cone Angle Constraint for a clock angle $\delta \in (-179; -1)$ . . . . .	58
9	Number of revolutions sail spends inside target area with a cone angle constraint of $\alpha_{\max} = 70^\circ$ , a clock angle constraint of $\delta \in (-179; -1)$ and sail turning rates of $\Omega_{\max} = 0.1^\circ/\text{s}$ , $0.25^\circ/\text{s}$ , $0.5^\circ/\text{s}$ , $1^\circ/\text{s}$ and $2^\circ/\text{s}$ . . . . .	59
10	Targeted states used for homing trajectory optimisation . . . . .	68
11	Results of the homing trajectory optimisation for an unrestricted solar sail. . . . .	68
12	Final state of the homing trajectory obtained with Seed 2, used as the initial state for the hold trajectory optimisation. . . . .	71
A1	Inertial state of target and chaser for Verification of coordinate transformation from inertial to co-moving frame . . . . .	85
A2	Transformed co-moving state of chaser and error for the verification of coordinate transformation from inertial to co-moving frame . . . . .	85
A3	Error of coordinate transformation from co-moving to inertial frame . . . . .	86
A4	Analysis of input sets for homing trajectory optimisation across five runs . . . . .	91
A5	Analysis of input sets for hold trajectory optimisation across five runs . . . . .	93
C1	Initial states and corresponding sail attitude laying on the hold trajectory of Case 1 as seen in Table 2 with a maximum cone angle of $70^\circ$ . . . . .	98
C2	Initial conditions and corresponding sail attitudes for safety analysis of trajectories under a positive clock angle profile, showing the effect of different sail attitudes on drift in the V-bar direction. . . . .	99
C3	Initial conditions and corresponding sail attitudes for safety analysis of trajectories under a negative clock angle profile, showing the effect of different sail attitudes on drift in the V-bar direction. . . . .	100
C4	Results of the homing trajectory optimisation for an unrestricted solar sail for different maximum simulation times. . . . .	100

# Nomenclature

## Abbreviations

Abbreviation	Definition
ADR	Active Debris Removal
ANN	Artificial Neural Network
CW	Clohessy - Wiltshire
EA	Evolutionary Algorithm
ENC	Evolutionary Neurocontroller
FNN	Feed-Forward Neural Network
GEI	Geocentric Equatorial Inertial Reference Frame
GEO	Geostationary Orbit
LEO	Low Earth Orbit
NC	Neurocontroller
NE	Neuroevolution
RDC	Real Delta Coding
SRP	Solar Radiation Pressure
ToF	Time of Flight

## Latin Symbols

Symbol	Definition
$A$	area
$\mathbf{a}$	acceleration vector
$\tilde{a}$	semi-major axis
$e$	epoch
$\tilde{e}$	eccentricity
$F$	force
$\mathbf{f}$	thrust vector
$H$	search subspace
$h$	step size
$\tilde{h}$	altitude
$I$	geocentric equatorial inertial reference frame $(X, Y, Z)$
$J$	cost function
$\mathbf{k}$	rotation axis
$M$	co-moving reference frame $(x, y, z)$
$m$	mass
$N$	total number of time steps

---

Symbol	Definition
$n$	mean motion
$\mathbf{n}$	solar sail normal vector
$P$	solar radiation pressure
$r$	distance
$\mathbf{r}$	position vector
$S$	Sun-sail line reference frame
$s_\gamma$	sigmoid activation function( $\tilde{X}, \tilde{Y}, \tilde{Z}$ )
$T$	transfer time
$t$	time
$\mathbf{u}$	Sun-sail vector
$\Delta V$	velocity increment
$v$	velocity
$w_{ij}$	connection weight between neurons $j$ and $i$
$\Delta X$	trajectory accuracy

---

## Greek Symbols

---

Symbol	Definition
$\alpha$	cone angle
$\beta$	solar sail lightness number
$\delta$	clock angle
$\varepsilon$	orbital energy
$\gamma$	vernal equinox
$\tilde{\gamma}$	temperature parameter
$\eta$	sail efficiency
$\mu$	gravitational parameter
$\psi$	centre line angle
$\sigma$	sail loading
$\theta$	true anomaly
$\tilde{\theta}$	bias
$\lambda$	locally ideal control vector
$\omega$	turning angle
$\Omega$	turning rate

---

## Indices

---

Symbol	Definition
0	initial
$c$	characteristic
C	chaser
<i>current</i>	current state

---

Symbol	Definition
$f$	final
$i$	incident
max	maximum allowable value
min	minimum allowable value
<i>previous</i>	previous state
$r$	reflected
$SC$	spacecraft
SRP	solar radiation pressure
T	target
$\oplus$	Earth
$\odot$	Sun

---

## Other Symbols and Notations

---

Symbol	Definition
$\square$	arbitrary variable
$\hat{\square}$	unit vector

---



# 1

## Introduction

Over the next decade, the number of active satellites in Earth's orbit is expected to increase dramatically, from approximately 9,000 currently (European Space Agency, 2023b) to over 100,000 (Hainaut & Williams, 2020), driven by new space initiatives and the deployment of mega-constellations. Many of these satellites will be placed into already crowded orbits, particularly Low Earth Orbit (LEO) and Geostationary Orbit (GEO), due to their high economic value (Schaub et al., 2015). However, these orbits already have the highest densities of space debris (European Space Agency, 2023b; Union of Concerned Scientists, 2023), with currently approximately 36 860 objects regularly tracked (European Space Agency, 2024). As a result, the risk of collisions between active satellites, between satellites and debris, and among debris pieces is increasing (Buchs & Florin, 2021). Collisions, such as the Iridium-33 and Cosmos-2251 collision, have already occurred in 2009 (Kelso et al., 2009), significantly contributing to the debris population. If current practices continue, the debris population will grow exponentially, potentially leading to an uncontrolled proliferation (Kessler et al., 2010), which could render entire orbital regions unusable. Space debris has thus become an increasingly urgent issue for the safe operation of spacecraft in Earth's orbit. While enforcing strict guidelines for debris mitigation through regulatory approaches, such as post-mission disposal (European Space Agency, 2023a), may slow the growth of the debris population, it cannot halt it entirely (Lemmens & Letizia, 2020).

To stabilise the debris population, it is necessary to actively remove large debris pieces, the primary contributors to debris proliferation, through active debris removal (ADR) missions (Bastida Virgili & Krag, 2009). Previous simulations indicate that removing five large debris objects per year could stabilise the debris population (Lemmens & Letizia, 2020). However, the rapid increase in satellite launches may require an even higher removal rate. Although no ADR mission has been conducted yet, current approaches and tests rely on conventional impulsive propulsion systems (Astroscale, 2024; Choi, Park, & Lee, 2024). The limited onboard fuel capacity of these systems could restrict mission duration and operational altitude and may limit them to remove only a single debris piece per mission. As many debris pieces need to be removed in the future, a large fleet would be necessary, significantly increasing overall costs. By employing low-thrust, propellant-less propulsion systems such as solar sails, it may be possible to extend the scope and duration of ADR missions due to their nearly unlimited  $\Delta V$

budget. Solar sails may be utilised in preparation for ADR missions by travelling to potential target objects to observe and characterise them since the exact shape and rotation rates of debris pieces are often unknown (Sato, 1999). Furthermore, this technology may be used directly for debris removal by allowing the sequential transfer of multiple debris objects to lower-altitude orbits, where they can naturally de-orbit due to atmospheric drag. This approach potentially allows for the removal of multiple debris objects within a single mission.

Various methods have been proposed for capturing debris objects, including mechanical arms, harpoons, nets, and robotic servicing techniques (Mark & Kamath, 2019; Shan, Guo, & Gill, 2016). A common requirement across all these approaches is that the chaser spacecraft must perform proximity operations, even when the mission objective is solely to observe and characterise debris objects. Proximity operations have been studied for spacecraft employing conventional propulsion systems (Fehse, 2003; Goodman, 2006; Gurfil, 2023). However, these results cannot be directly applied to solar sail proximity operations due to their inherently limited thrusting capabilities. While the use of solar sails during the initial phasing phase of rendezvous missions has been explored (Bianchi et al., 2024), there is a significant gap in the literature regarding the subsequent phases of proximity operations using solar sails. Specifically, no research has yet been conducted on far-range and close-range operations, mating and docking procedures, or departure manoeuvres utilising solar sails. This lack of research highlights the need to develop new strategies to utilise solar sails as a sustainable alternative for ADR missions.

## 1.1. Research Objective and Questions

While research has been conducted on the phasing phase of ADR missions using solar sails (Bianchi et al., 2024), specifically demonstrating successful transfers from lower parking orbits to target debris in low Earth orbit, there is a lack of research addressing the subsequent phases of proximity operations. Therefore, this research aims to begin bridging this gap by investigating far-range rendezvous operations, also known as homing, to connect previous studies on phasing with the subsequent phase of close-range rendezvous operations. Therefore, this research sets out to achieve the following objective:

**Contribute to a sustainable space environment by exploring the feasibility of solar-sail active debris removal missions, focusing on far-range rendezvous operations.**

Far-range rendezvous operations aim to transfer from the phasing orbit to a first aim point, usually a hold point, close to the target. This hold point is typically situated on the target's orbit and serves as a safe location where the chaser can remain for an extended period at zero  $\Delta V$  cost. However, maintaining a hold point is not feasible for a solar sail due to its unique dynamics and operational constraints, which inevitably cause it to drift away from the hold point. Instead, a hold trajectory is proposed to serve the same purpose. Thus, this research investigates whether hold trajectories are a viable alternative to classical hold points for solar sails. Additionally, it explores the feasibility of designing preliminary homing trajectories for solar sails that target hold trajectories. To conduct both investigations, InTrance, a trajectory optimisation tool that employs artificial intelligence and evolutionary algorithms is utilised. This leads to the formulation of the following research questions:

1. *Can hold trajectories replace classical hold points for solar-sail far-range rendezvous operations?*
2. *How do safety considerations and the sail's operational constraints affect the size and position of hold trajectories?*
3. *Can a preliminary homing trajectory for solar sails be designed with InTrance?*

By investigating these areas, this work seeks to contribute to the understanding of solar-sail proximity operations and lay the groundwork for future research in the field.

## 1.2. Thesis Outline

To address the research questions outlined in the previous section, the methodology presented in Chapter 2 will be employed. It begins with an introduction to the concept of solar sails, followed by an overview of proximity operations and a description of the trajectory optimization tool InTrance. The results are presented in three dedicated chapters: Chapter 3 investigates the characteristics of the relative motion of solar sails to build an understanding of how their unique dynamics impact the movement relative to a target object. Building on these results, Chapter 4 explores solar sail hold trajectories as an alternative to classical hold points. The safety of different hold trajectory locations is examined, and the impact of the sail's operational constraints on these trajectories is assessed. The most favourable location can be targeted during homing as outlined in Chapter 5. The focus is on optimising homing trajectories for solar sails connecting the phasing phase to hold trajectories. This chapter evaluates the feasibility of designing such trajectories using the InTrance optimisation tool. The conclusion is presented in Chapter 6 by answering the research questions. Furthermore, the chapter provides recommendations for future work to continue research on solar sail proximity operations. Finally, this thesis ends with three appendices. The appendices will include a section on verification and validation, another providing input configurations for InTrance, and a final appendix featuring additional figures and tables.

# 2

## Methodology

The methodology presented in this chapter outlines a framework for simulating and optimising solar-sail proximity operations. It begins with an introduction to the solar-sail model, detailing the ideal sail model used in this work and a locally optimal steering law. Since the sail’s operational constraints must be considered, the optimal steering law is then adapted accordingly. Next, the chapter introduces proximity operations, including a reference frame typically used in rendezvous missions and an overview of the different phases of a rendezvous mission. The unique challenges solar sails face during proximity operations are also discussed, along with a potential alternative to classical hold points. Subsequently, this chapter describes the equations of motion and the environmental model used in the simulations. Furthermore, a trajectory optimisation approach using neuroevolution, a combination of artificial neural networks and evolutionary algorithms, is presented. The design of the neurocontroller and the fitness assignment strategies, which enable the autonomous generation of optimal steering commands for the solar sail, are explored. Lastly, the simulation and optimisation setup used in this work is presented.

### 2.1. Solar-Sail Model

This section outlines the framework of the solar-sail model used in this work. First, the ideal solar-sail model is introduced, followed by a discussion of a locally optimal steering strategy for planet-centred solar-sail missions. Lastly, to incorporate the operational limitations of solar sails, the locally optimal steering is adapted to account for the sail’s operational constraints, such as limits on the Sun incidence angle, the clock angle, and constraints on the angular turning rate of the sail.

#### 2.1.1. Ideal Solar-Sail Model

Within this work, the ideal solar-sail model is used, which assumes a perfect specular reflection. Before defining the solar radiation pressure (SRP) force  $\mathbf{F}_{\text{SRP}}$ , which acts on a perfectly reflective solar sail, it is convenient to introduce the sail control angles. The sail control angles are defined with respect to the Sun-sail line reference frame and are shown in Figure 1. In the Sun-sail line reference frame  $S(\tilde{X}, \tilde{Y}, \tilde{Z})$ , the coordinate axes are defined as follows:

- The Sun is fixed along the  $\tilde{X}$ -axis.

- The  $\tilde{Y}$ -axis aligns with the heliocentric velocity vector of the planet around which the solar sail is orbiting.
- The  $\tilde{Z}$ -axis is established to complete a right-handed Cartesian coordinate system.

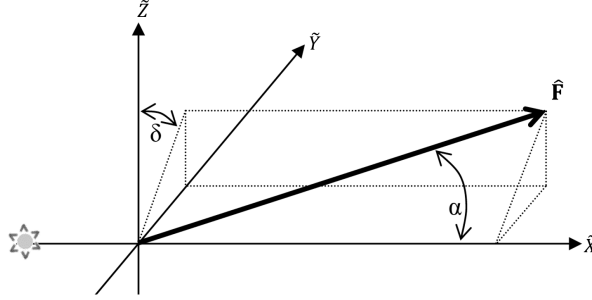


**Figure 1:** Sail control angles in Sun-sail line reference frame (Macdonald & McInnes, 2005).

The solar-sail cone angle  $\alpha$  is defined as the angle between the sail normal and the direction of the incident photons (McInnes, 2004). As the sail acceleration cannot be directed towards the Sun, the sail cone angle is defined as  $\alpha \in [0, \pi]$ . The sail clock angle  $\delta$  represents the angle of rotation of the sail normal around the Sun-line, measured from a reference direction in the plane perpendicular to the Sun-line and is defined as  $\delta \in (-\pi, \pi]$ .

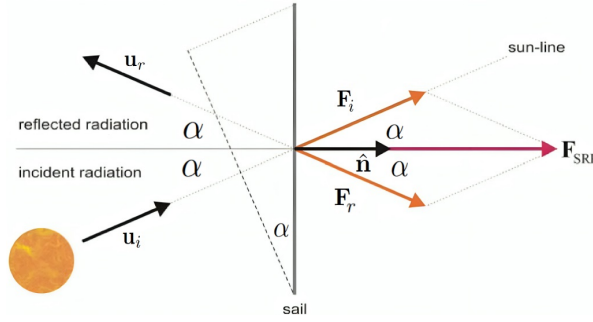


**Figure 2:** SRP force on a perfectly reflecting solar sail. Adapted from Dachwald (2005) by changing parameter designations.

The SRP force can now be derived from Figure 2. The force due to incident photons from the  $\mathbf{u}_i$  direction and the force due to reflected photons in  $\mathbf{u}_r$  direction can be written as

$$\mathbf{F}_i = PA(\mathbf{u}_i \cdot \hat{\mathbf{n}}) \mathbf{u}_i \quad (2.1.1)$$

$$\mathbf{F}_r = PA(\mathbf{u}_i \cdot \hat{\mathbf{n}}) \mathbf{u}_r \quad (2.1.2)$$

where  $P$  is the solar radiation pressure at distance  $r$  from the Sun,  $A$  is the total sail frontal area,  $A(\mathbf{u}_i \cdot \hat{\mathbf{n}})$  is the projected sail area along the  $\mathbf{u}_i$  direction and  $\hat{\mathbf{n}}$  is the unit vector normal to the sail surface (Dachwald, 2005). The total SRP force exerted on the solar sail can now be calculated using  $\mathbf{u}_i - \mathbf{u}_r = 2(\mathbf{u}_i \cdot \hat{\mathbf{n}})^2 \hat{\mathbf{n}}$

$$\mathbf{F}_{\text{SRP}} = \mathbf{F}_i + \mathbf{F}_r = 2PA(\mathbf{u}_i \cdot \hat{\mathbf{n}})^2 \hat{\mathbf{n}} \quad (2.1.3)$$

Using the relation  $\mathbf{u}_i \cdot \hat{\mathbf{n}} = \cos \alpha$ , the SRP force simplifies to:

$$\mathbf{F}_{\text{SRP}} = 2PA \cos^2 \alpha \hat{\mathbf{n}} \quad (2.1.4)$$

To account for non-perfect reflectivity and potential sail deformation under load, a sail efficiency coefficient  $\eta$  is introduced (McInnes, 2004). Additionally, the sail loading  $\sigma = \frac{m}{A}$ , defined as the ratio of spacecraft mass  $m$  to sail frontal area, allows the SRP acceleration  $\mathbf{a}_{\text{SRP}}$  to be expressed as:

$$\mathbf{a}_{\text{SRP}} = 2\eta \frac{P}{\sigma} \cos^2 \alpha \hat{\mathbf{n}} \quad (2.1.5)$$

To derive a modified version of Eq. 2.1.5, the sail lightness number is introduced, denoted as  $\beta$ :

$$\beta = \frac{a_c}{a_0} \quad (2.1.6)$$

Here,  $a_c$  represents the characteristic acceleration due to SRP at a distance of one astronomical unit (AU) from the Sun. The reference acceleration  $a_0$  is defined as  $a_0 = \mu_{\odot}/r_0^2$ , where  $\mu_{\odot}$  is the Sun's gravitational parameter and  $r_0$  represents the distance of one AU (Dachwald, 2005). Using this definition, the SRP acceleration can be reformulated as:

$$\mathbf{a}_{\text{SRP}} = 2\beta \frac{\mu_{\odot}}{r^2} \cos^2 \alpha \hat{\mathbf{n}} \quad (2.1.7)$$

### 2.1.2. Locally Optimal Steering

Unlike other low-thrust spacecraft that can orient their thrust vector in any desired direction, the thrust vector of a solar sail is constrained to lie on the surface of a force "bubble" that always points away from the Sun (Dachwald, 2005), as illustrated in Figure 3. This constraint significantly influences the steering strategy for solar sails. For example, in Earth-centred missions, the potential for energy gain from solar sails is limited when the sailcraft is directed toward the Sun (McInnes, 2004).

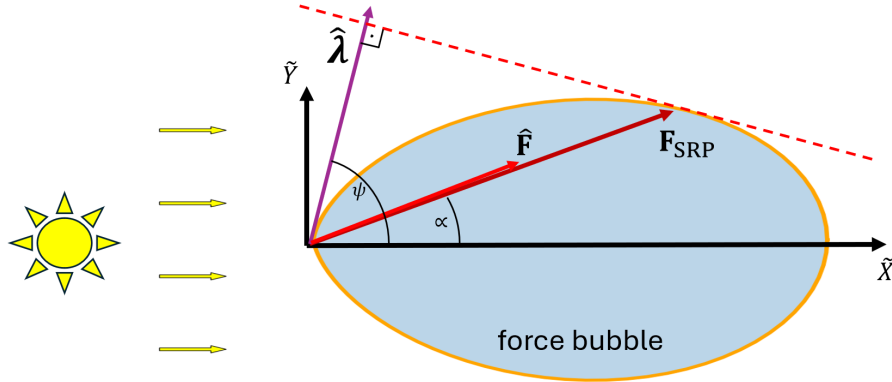


Figure 3: Solar-Sail Force Bubble and Locally Optimal Steering.

If  $\hat{\lambda}$  denotes the locally ideal control unit vector in the desired thrust direction, the thrust unit vector  $\hat{\mathbf{F}}_{\text{SRP}}$  must align with the direction of the optimal control vector that maximises the SRP force along  $\hat{\lambda}$  (Dachwald, 2005). For a perfectly reflective sail, the SRP force is always directed normal to the sail surface, and thus  $\hat{\mathbf{F}}_{\text{SRP}} = \hat{\mathbf{n}}$ . The optimal sail control angles are as follows (McInnes, 2004). As the

magnitude of the sail acceleration does not depend on the sail clock angle, the locally optimal sail clock angle can be directly calculated from  $\hat{\lambda}$ . Thus,

$$\delta = \arctan2(\lambda_{\hat{y}}, \lambda_{\hat{z}}) \quad (2.1.8)$$

With the cone angle of the locally ideal control unit vector defined as

$$\psi = \arccos(\lambda_{\hat{x}}) \quad , \quad (2.1.9)$$

the locally optimal sail cone angle can be defined as

$$\alpha = \frac{1}{2} \left[ \psi - \arcsin \left( \frac{\sin \psi}{3} \right) \right] \quad , \alpha \in [0, \pi] \quad (2.1.10)$$

The sail normal vector in the frame  $S$  can then be obtained by

$$\hat{\mathbf{n}} = \begin{pmatrix} \cos \alpha \\ \sin \alpha \sin \delta \\ \sin \alpha \cos \delta \end{pmatrix} \quad (2.1.11)$$

### 2.1.3. Constrained Optimal Steering

Operational constraints of a solar sail can impact the design of a mission by influencing performance and control capabilities. One of the constraints involves limitations on the Sun incidence angle, which directly affects the allowable cone angle (Heaton, Ahmad, and Miller, 2017), thereby necessitating the definition of a maximum allowable cone angle  $\alpha_{\max}$ . The Sun incidence angle significantly impacts several aspects of the spacecraft's operation:

- **Electrical Power Generation:** The sail's orientation affects the performance of solar arrays mounted on the spacecraft. Optimal power generation requires specific angles to maximise solar exposure; deviations can result in insufficient power for onboard systems.
- **Thermal Control:** The spacecraft's thermal environment is influenced by its attitude relative to the Sun. Improper angles can lead to overheating of components, potentially compromising system functionality and longevity (Tsuda et al., 2011, Johnson et al., 2011).
- **Thrust Generation:** Imposing a maximum allowable cone angle constrains the sail's ability to adjust its thrust, particularly its ability to reduce thrust. Since the sail is no longer permitted to adopt an edge-on orientation toward the Sun, it cannot nullify the SRP acting upon it. As a result, when exposed to sunlight, the sail is constantly under acceleration.

Another constraint is the maximum angular turning rate  $\Omega_{\max}$  of the sail, determined by the torque output of the attitude control system (Losada, 2024) and the sail's moment of inertia. Rapid attitude adjustments can generate high inertial forces, posing a risk of damaging the slender booms and fragile harness of the sail (Wie, 2004). These factors restrict the sail's agility and necessitate limitations on the sail turning rate. Additionally, limits on the clock angle may be imposed, requiring the definition of a minimum and maximum allowable clock angle, denoted as  $\delta_{\min}$  and  $\delta_{\max}$ , respectively.

These constraints impose the need to adapt the calculation of the optimal control angles. The constraints are implemented as described below:

### Sun Incidence Angle Constraint

The constrained sail cone angle is:

$$\alpha = \begin{cases} \frac{1}{2} \left[ \pi - \arcsin \left( \frac{\sin \psi}{3} \right) \right] & \text{if } \frac{1}{2} \left[ \pi - \arcsin \left( \frac{\sin \psi}{3} \right) \right] \leq \alpha_{\max} \\ \alpha_{\max} & \text{otherwise} \end{cases} \quad (2.1.12)$$

ensuring  $\alpha \in [0, \alpha_{\max}]$ .

### Clock Angle Constraint

The constrained sail clock angle is defined as:

$$\delta = \begin{cases} \arctan2(\lambda_{\bar{Y}}, \lambda_{\bar{Z}}) & \text{if } \delta_{\min} \leq \arctan2(\lambda_{\bar{Y}}, \lambda_{\bar{Z}}) \leq \delta_{\max} \\ \delta_{\min} & \text{if } \arctan2(\lambda_{\bar{Y}}, \lambda_{\bar{Z}}) < \delta_{\min} \\ \delta_{\max} & \text{if } \arctan2(\lambda_{\bar{Y}}, \lambda_{\bar{Z}}) > \delta_{\max} \end{cases} \quad (2.1.13)$$

ensuring  $\delta \in [\delta_{\min}, \delta_{\max}]$ .

### Angular Turning Rate Constraint

To ensure that the transition between successive attitude orientations adheres to a predefined maximum turning rate, the sail control angles must be adjusted accordingly. The sail control angles are expressed as:

$$\delta = \begin{cases} \arctan2(\lambda_{\bar{Y}}, \lambda_{\bar{Z}}) & \text{if } \omega \leq \omega_{\max} \\ \delta_{\text{adjusted}} & \text{otherwise} \end{cases} \quad (2.1.14)$$

$$\alpha = \begin{cases} \frac{1}{2} \left[ \pi - \arcsin \left( \frac{\sin \psi}{3} \right) \right] & \text{if } \omega \leq \omega_{\max} \\ \alpha_{\text{adjusted}} & \text{otherwise} \end{cases} \quad (2.1.15)$$

where  $\omega$  is the turning angle between the previous sail normal vector  $\hat{\mathbf{n}}_{\text{previous}}$  and the current optimal sail normal vector  $\hat{\mathbf{n}}_{\text{current}}$ ,  $\omega_{\max}$  the maximum allowable turning rate and  $\delta_{\text{adjusted}}$  and  $\alpha_{\text{adjusted}}$  the adjusted sail control angles, if  $\omega$  exceeds  $\omega_{\max}$ . The maximum allowable turning angle  $\omega_{\max}$  is defined as:

$$\omega_{\max} = \Omega_{\max} \cdot h \quad (2.1.16)$$

where  $h$  is the time interval between the two successive states. The turning angle  $\omega$  can be expressed as:

$$\omega = \arccos(\hat{\mathbf{n}}_{\text{previous}} \cdot \hat{\mathbf{n}}_{\text{current}}) \quad (2.1.17)$$

If  $\omega$  exceeds  $\omega_{\max}$ , the current orientation must be adjusted, by rotating  $\hat{\mathbf{n}}_{\text{previous}}$  towards  $\hat{\mathbf{n}}_{\text{current}}$  by

$\omega_{\max}$ . The rotation occurs about an axis  $\mathbf{k}$  defined by:

$$\mathbf{k} = \frac{\hat{\mathbf{n}}_{\text{previous}} \times \hat{\mathbf{n}}_{\text{current}}}{\|\hat{\mathbf{n}}_{\text{previous}} \times \hat{\mathbf{n}}_{\text{current}}\|} \quad (2.1.18)$$

The adjusted sail normal vector  $\hat{\mathbf{n}}_{\text{adjusted}}$  is computed using Rodrigues' rotation formula (Rodrigues, 1840):

$$\hat{\mathbf{n}}_{\text{adjusted}} = \hat{\mathbf{n}}_{\text{previous}} \cos \omega_{\max} + (\mathbf{k} \times \hat{\mathbf{n}}_{\text{previous}}) \sin \omega_{\max} + \mathbf{k} (\mathbf{k} \cdot \hat{\mathbf{n}}_{\text{previous}}) (1 - \cos \omega_{\max}) \quad (2.1.19)$$

The corresponding adjusted control angles are:

$$\delta_{\text{adjusted}} = \arctan2 \left( n_{\text{adjusted}, \tilde{Y}}, n_{\text{adjusted}, \tilde{X}} \right) \quad (2.1.20)$$

$$\alpha_{\text{adjusted}} = \arccos \left( n_{\text{adjusted}, \tilde{Z}} \right) \quad (2.1.21)$$

## 2.2. Proximity Operations

Proximity operations and rendezvous are critical components of numerous space missions, including on-orbit servicing (Hudson & Kolosa, 2020), refuelling (Chen & Yu, 2017), docking with space stations for human spaceflight (Goodman, 2006) and ADR missions. However, challenges arise during rendezvous operations when the chaser is a solar sail.

This section begins by defining the reference frames commonly used in proximity operations. It then introduces the phases of a rendezvous mission for conventional (non-solar sail) spacecraft. Following this, the unique challenges of solar-sail proximity operations are discussed. Subsequently, the equations of motion used in this work to simulate proximity operations are presented. Finally, the environmental model utilised in simulating solar-sail dynamics in this work is examined.

### 2.2.1. Reference Frames

Before defining the reference frame typically used in rendezvous missions, the Geocentric Equatorial Inertial (GEI) reference frame, denoted as the frame  $I(X, Y, Z)$ , is defined (Russell, 1971), as can be seen in Figure 4. The  $X$ -axis points from Earth's centre towards the vernal equinox  $\gamma$ . The  $Z$ -axis aligns with Earth's rotational axis, pointing towards the celestial north pole, while the  $Y$ -axis completes the right-handed orthogonal set.

The relative motion of the chaser spacecraft  $C$  with respect to a target  $T$  can be described in a co-moving, rotating reference frame  $M(x, y, z)$ , whose origin is at the target's centre of mass. This frame moves along with the target and rotates to maintain alignment with the target's orbital motion. The axes are defined with respect to the frame  $I$ , as can be seen in Figure 4.

- The  $x$ -axis (R-bar) points radially away from the Earth, along the position vector  $\mathbf{R}$  of the target.
- The  $z$ -axis (H-bar) is aligned with the orbital angular momentum vector of the target perpendicular to the orbital plane.
- The  $y$ -axis (V-bar) completes the right-handed orthogonal set and is thus directed towards the target's orbital velocity vector but is not necessarily aligned with it.

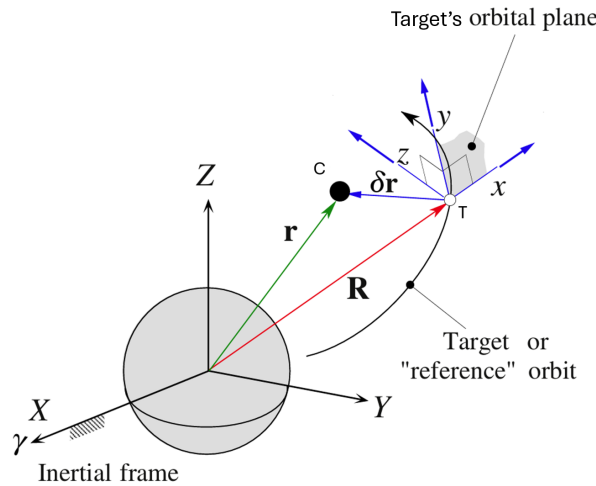


Figure 4: Frame  $M$  attached to target  $T$ , from which the chaser  $C$  is observed, relative to the frame  $I$ . Adapted from Curtis (2013) by changing axis labelling.

### 2.2.2. Phases of a Rendezvous Mission

Rendezvous missions can be divided into five phases: launch, phasing, far-range rendezvous, close-range rendezvous and mating (Fehse, 2003). A brief description of the phases can be seen in Figure 5. An overview of each phase will be given, and their objectives and end conditions will be discussed. It is noted that the following descriptions for the phases are for non-solar sail spacecraft.

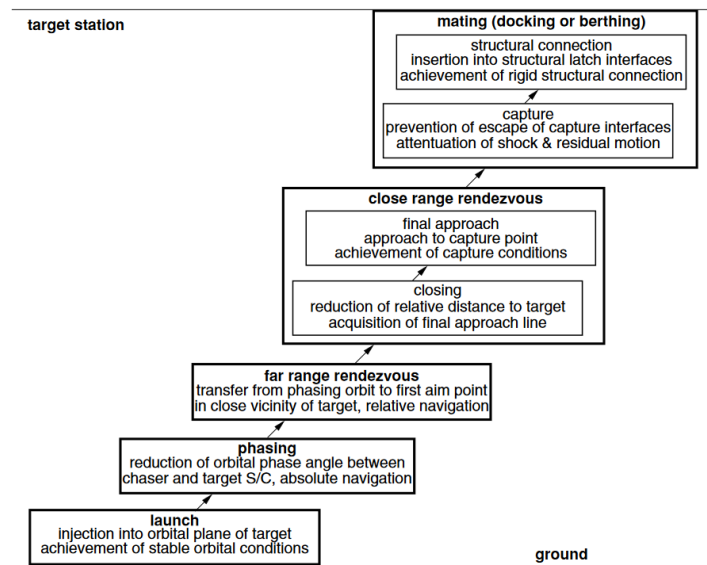
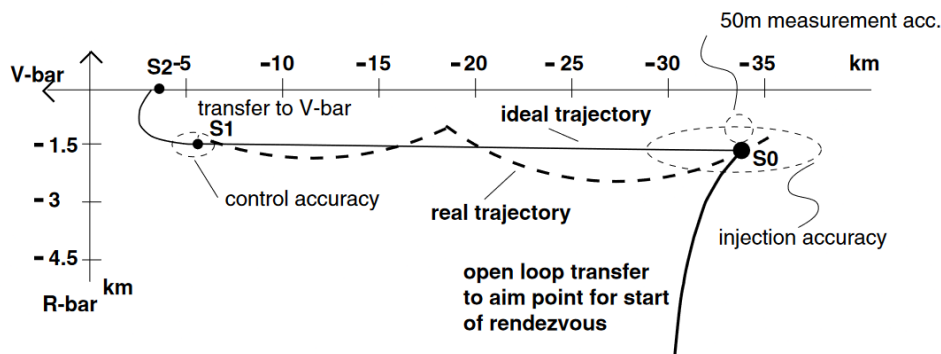


Figure 5: Main phases of a rendezvous mission (Fehse, 2003)

The aim of the launch is to deliver the chaser vehicle into a stable orbit, which lies in the orbital plane of the target. The chaser is usually released into a lower orbit with an arbitrary phase angle behind the target (Fehse, 2003). After separation from the launcher, the spacecraft deploys its solar arrays and antennas and initialises its subsystems. Once the chaser becomes operational, phasing can begin. Phasing aims to reduce the phasing angle and the orbit parameters between the chaser and the target. The phasing angle can be reduced by using the fact that a lower orbit has a shorter orbital period. Phasing ends when the chaser reaches an 'initial aim point' or achieves set margins for position and

velocity at a specific range called the entry gate, labelled S0 in Figure 6. The designated initial aim point or gate is positioned on the target orbit or in close proximity to it.

Far-range rendezvous operations, called 'homing', begin when the chaser reaches the initial aim point (Fehse, 2003). The primary objective is to minimise trajectory dispersion, ensuring the chaser attains the necessary position, velocity, and angular rate conditions for initiating close-range operations. Essential tasks include acquiring the target's orbit and reducing approach velocity. This phase typically ends at a point (labelled point S2 in Figure 6), marking the transition to standard rendezvous along fixed trajectories and timelines, which is advantageous for automated procedures. Operational requirements may limit the homing phase's endpoint; for example, the International Space Station defines an "approach ellipsoid" (2 km by 1 km) outside of which final rendezvous manoeuvres should commence. Consequently, far-range rendezvous operations often start at tens of kilometres and conclude a few kilometres from the target. Alternatively, the phase can end at a hold point on the target orbit, where the chaser can remain indefinitely without using propellant. Hold points serve multiple purposes, such as observing a target with an unknown shape or rotation rate (e.g., space debris) or synchronising the mission timeline with external events like Sun illumination or communication windows. To reach the hold point, trajectory elements during homing may include free drift trajectories on circular or elliptical orbits, where the chaser first transfers into a drift orbit located below the V-bar, starting from the initial aim point. Due to the lower orbit, the chaser drifts towards the target. Once the desired distance to the target is reached, a Hohmann transfer can be used to reach the targeted hold point.



**Figure 6:** Transfer from phasing orbit to rendezvous drift orbit. Adapted from Fehse (2003) by changing axis labelling.

The close-range rendezvous phase can be divided into a preparatory phase leading to a final approach corridor, called 'closing' and a final approach phase, leading to the mating phase (Fehse, 2003). However, in the case of an approach from the V-bar, these two sub-phases may not be able to be distinguished, as the direction of motion remains the same. At the beginning of this phase, all out-of-plane errors, such as inclination and right ascension of the ascending node, should have been corrected, and the mission timeline should be up to date. Furthermore, all parties involved, i.e., vehicles, space and ground segments, and when docking with a station, the crew should be ready for the final operation. Closing aims to reduce the remaining distance to the target and to align the chaser for the final approach corridor. This might include a fly-around manoeuvre to acquire the approach axis. Due to the proximity to the target, all operations in this phase are safety-critical and require special safety precautions for the trajectory and the design of the onboard systems. The final approach phase aims to achieve specific mating conditions regarding positions, velocities, relative attitude, and angular rates. A cone-shaped approach corridor is commonly implemented to guarantee a secure mating operation. This corridor

starts from the point of contact with the target vehicle and has a half-cone angle of 10-15 degrees. If the limits of the corridor are breached, commands to halt, retreat, or avoid collision can be given.

Two different mating processes can be distinguished: docking and berthing (Fehse, 2003). Docking involves the control of an approaching vehicle to guide its capture interfaces into the corresponding interfaces on the target vehicle. In contrast, during berthing, the manipulator arm assumes an active role by guiding its grapple mechanism to capture the passive grapple fixture on the other vehicle. The manipulator arm can be located on either the target station or the approaching vehicle, and the same applies to the passive grapple fixture.

Safety considerations are crucial in rendezvous operations, especially when dealing with passive, unresponsive objects like space debris, as an evasive manoeuvre can only be conducted by the chaser satellite. Rendezvous operations must be designed to minimise the risk of collision with the target object and to ensure the spacecraft's integrity throughout the mission. To ensure these safety objectives are met, the trajectory design must address several factors, including collision avoidance, emergency manoeuvrability, and contingency plans for attitude anomalies, as outlined below (Fehse, 2003).

### Collision Avoidance

Maintaining a safe distance from the target is important for mission safety while conducting homing and far and close-range rendezvous operations.

- **Minimum Target Distance:** A predefined minimum distance from the target must be maintained to prevent accidental collisions. This safety zone should account for potential trajectory deviations caused by environmental factors or system errors, ensuring that even under unforeseen circumstances, the spacecraft remains at a safe distance. A safety zone can be enforced by defining an ellipsoid around the target.

### Emergency Manoeuvrability

The spacecraft must be capable of responding fast to emergencies to ensure safety.

- **Rapid Departure Capability:** In the event of an emergency, such as a system failure, unexpected behaviour from the target or collision threats, the spacecraft must be able to quickly and safely distance itself from the target.

### Attitude Anomalies

Potential attitude anomalies must be considered in safety planning to mitigate risks.

- **Stuck Attitude Scenarios:** If the chaser becomes stuck in a particular orientation due to a malfunction, the resulting forces, like SRP force or atmospheric drag, should not cause the spacecraft to drift toward the target. The trajectory design must ensure that, under such circumstances, the spacecraft will either maintain a safe distance or naturally move away from the target.
- **Uncontrolled Rotation:** In the event that the spacecraft enters an uncontrolled spin, procedures must be established to mitigate the spin and prevent collision risks.

## 2.2.3. Solar-Sail Far-Range Rendezvous Operations

As previously explained, the primary objective of far-range rendezvous operations is to close the distance to the target and to reach a designated hold point from which standard rendezvous procedures can

start. The hold point should be situated outside of the approach ellipsoid, which should not be entered during far-range rendezvous operations, effectively functioning as a "Safety Zone." This ensures that any unplanned deviations in the sail's trajectory do not pose any collision risk. Furthermore, hold points are usually situated on the target orbit, allowing the chaser to maintain a fixed position relative to the target for a longer period. However, when the chaser is a solar-sail spacecraft, unique challenges arise.

The SRP force acting upon the sail will cause it to drift away from the hold point. Even if the sail is oriented edge-wise to the Sun to minimise the SRP force, the large size of the sail results in significant atmospheric drag in LEO. This drag induces drift as well, making it difficult to maintain a fixed position relative to the target. These factors make maintaining a traditional hold point unfeasible for a solar sail, rendering it an unsuitable endpoint for far-range rendezvous operations. Therefore, instead of attempting to maintain a fixed hold point, a dynamic "hold trajectory" may be established. Such a trajectory would allow the sailcraft to manoeuvre continuously, actively compensating for SRP and other perturbations while still remaining in proximity to the target over an extended period of time.

Designing an effective hold trajectory for a solar sail involves meeting specific operational constraints and safety considerations, which have already been introduced in subsection 2.1.3 and subsection 2.2.2, respectively, while still allowing for target observation. To establish a hold trajectory, a hold volume is defined as the spatial region within which the chaser must remain during the hold phase. Two types of hold trajectories are considered: an encircling hold trajectory and a leading/trailing hold trajectory, as shown in Figure 7.

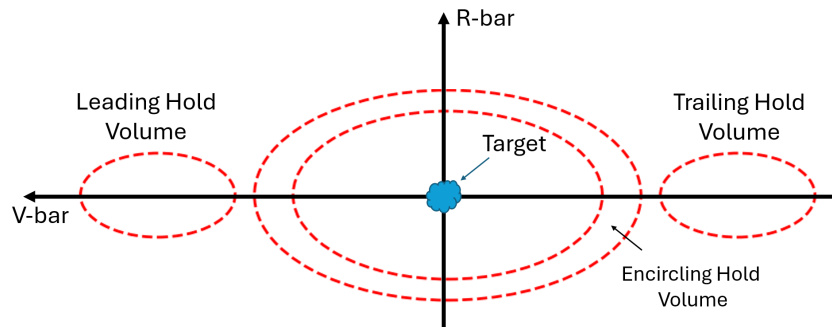
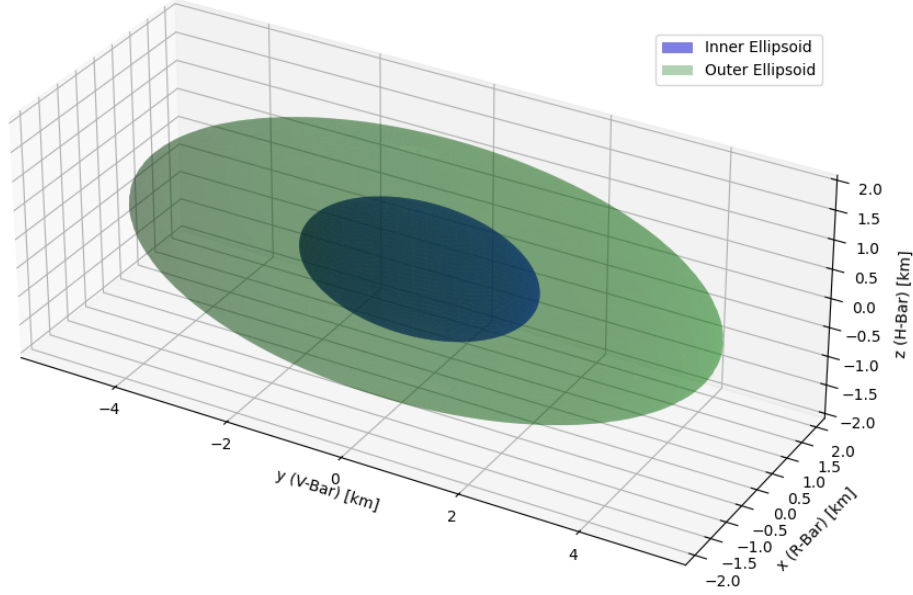


Figure 7: Encircling and leading/trailing hold volumes

In the encircling hold trajectory configuration, two concentric ellipsoids are established around the target object (see Figure 8). The hold volume is defined as the region between these two ellipsoids. In this setup, the inner ellipsoid functions as a safety zone surrounding the target, ensuring a minimum separation distance to prevent potential collisions. The chaser spacecraft operates within this hold volume, allowing it to encircle the target while maintaining a safe distance and observing it from nearly all angles. However, if the trajectory lies in the same orbital plane as the target, safe arrival and departure might become challenging. The chaser may inadvertently enter the safety zone, risking a close pass or even a collision with the target object. This configuration also poses issues during emergency situations when the sail needs to quickly distance itself from the target due to the same reason.

In the leading/trailing hold trajectory configuration, the hold volume is defined by a single ellipsoid positioned either ahead of or behind the target along its orbital path. The chaser spacecraft must remain within this ellipsoid. This setup has the advantage that, even if the hold trajectory lies in the



**Figure 8:** Target volume for hold-trajectory optimisation

same plane as the target's orbit, safe arrival and departure are possible from the positive or negative V-bar direction, respectively, without passing by the target. This greatly increases safety, especially in emergency situations when the chaser needs to quickly distance itself from the target. However, a disadvantage of this configuration is that if the target is non-rotating, the chaser can only observe it from one side, limiting overall observability.

The ellipsoids are parametrised by:

- Semi-Major Axis: V-Bar direction.
- Semi-Minor Axis: R-Bar direction.
- Semi-Minor Axis: H-Bar direction.

#### 2.2.4. Equation of Motion

When the chaser and the target are under the sole influence of the point mass gravitational acceleration of Earth, their equation of motion (EOM) in the frame  $I$  is

$$\ddot{\mathbf{r}} = -\mu_{\oplus} \frac{\mathbf{r}}{\|\mathbf{r}\|^3} \quad (2.2.1)$$

where  $\mathbf{r}$  is their position vector in the frame  $I$  and  $\mu_{\oplus}$  is Earth's gravitational parameter. Solving this equation requires an ordinary differential equation solver, which can be computationally demanding when high accuracy is needed.

Assuming the chaser and target are in close proximity, and the target is in a circular orbit, Eq. 2.2.1

can be linearised and expressed in the frame  $M$  (Wakker, 2015):

$$\ddot{x} - 3n^2x - 2n\dot{y} = a_x \quad (2.2.2a)$$

$$\ddot{y} + 2n\dot{x} = a_y \quad (2.2.2b)$$

$$\ddot{z} + n^2z = a_z \quad (2.2.2c)$$

where  $n$  is the mean motion of the target and  $a_x$ ,  $a_y$  and  $a_z$ , represent additional forces acting on the chaser in the R-bar, V-bar, and Z-bar directions, respectively. These differential equations are known as the *Clohessy - Wiltshire (CW) equations* and can be solved analytically to obtain the position and velocity components of the chaser relative to the target (see Wakker (2015) for the full derivation):

$$x = x_0(4 - 3\cos nt) + \frac{\dot{x}_0}{n}\sin nt + \frac{2\dot{y}_0}{n}(1 - \cos nt) + \frac{a_x}{n^2}(1 - \cos nt) + \frac{2a_y}{n^2}(nt - \sin nt) \quad (2.2.3a)$$

$$y = y_0 - \frac{\dot{y}_0}{n}(3nt - 4\sin nt) - 6x_0(nt - \sin nt) - 2\frac{\dot{x}_0}{n}(1 - \cos nt) - \frac{2a_x}{n^2}(nt - \sin nt) + \frac{2a_y}{n^2}\left(2 - \frac{3}{4}n^2t^2 - 2\cos nt\right) \quad (2.2.3b)$$

$$z = z_0\cos nt + \frac{\dot{z}_0}{n}\sin nt + \frac{a_z}{n^2}(1 - \cos nt) \quad (2.2.3c)$$

$$\dot{x} = 3x_0\sin nt + \dot{x}_0\cos nt + 2\dot{y}_0\sin nt + \frac{a_x}{n}\sin nt + 2\frac{a_y}{n}(1 - \cos nt) \quad (2.2.3d)$$

$$\dot{y} = -\dot{y}_0(3 - 4\cos nt) - 6x_0n(1 - \cos nt) - 2\dot{x}_0\sin nt - \frac{2a_x}{n}(1 - \cos nt) - 2\frac{a_y}{n}\left(\frac{3}{2}nt - 2\sin nt\right) \quad (2.2.3e)$$

$$\dot{z} = -z_0n\sin nt + \dot{z}_0\cos nt + \frac{a_z}{n}\sin nt \quad (2.2.3f)$$

where  $x_0$ ,  $y_0$ ,  $z_0$ ,  $\dot{x}_0$ ,  $\dot{y}_0$  and  $\dot{z}_0$  are the Cartesian components of the position and velocity at time  $t = 0$  of the chaser in the frame  $M$  and the quantity  $nt$  indicates the central angle that the target covers in the time interval  $0 - t$ , which is also used to calculate the new position of the target. Since the CW equations are a linearisation of the non-linear orbital dynamics, they introduce inaccuracies that become more pronounced over time or at larger separations (see Section A.6). However, the significant computational efficiency gained from their analytical solutions makes them advantageous for the initial analysis conducted in this thesis (see Section A.7). Therefore, the Clohessy-Wiltshire equations are used to describe the relative motion of the chaser with respect to the target in this work.

### 2.2.5. Environmental Model

In this work, a simple environmental model is used to focus on the primary dynamics of the sailcraft without the complexity introduced by other perturbations. The characteristics of this model are:

- **Perturbing Forces:** Only the SRP force acting on the solar sail is considered as an additional perturbing force. Therefore, in Eq. 2.2.2, the acceleration components  $a_x$ ,  $a_y$  and  $a_z$  in frame  $M$  represent solely the SRP-induced accelerations.
- **Solar Radiation Pressure:** The SRP acting on the spacecraft is assumed to be constant throughout the simulation, with a value of  $P = 4.56 \times 10^{-6} \text{ N/m}^2$

- **Sun Location:** The Sun is located at the autumnal equinox and is assumed to be stationary.
- **Sunlight:** The Sunlight reaching Earth is assumed to be parallel.
- **Shadow Model:** A simple cylindrical shadow model is used to determine eclipse periods.

## 2.3. Trajectory Optimisation Using InTrance

One of the primary objectives of this thesis is to identify potential locations for hold trajectories relative to the target where the sail can safely remain for an extended period of time and to investigate the impact of attitude constraints on them. However, due to constraints imposed on the sail, like a maximum allowable cone angle, the spacecraft cannot simply follow an elliptical orbit. Consequently, finding a trajectory that remains close to the target while adhering to safety considerations transforms this problem into an optimal control problem. Furthermore, during the homing phase, the endpoint of the homing trajectory should seamlessly transition into the hold trajectory, minimising state deviation at that point while also reducing transfer time. This further emphasises the need for trajectory optimisation. Numerous methods exist for designing spacecraft trajectories, including indirect methods, direct methods, and heuristics (Chai et al., 2019; Conway, 2010; Shirazi, Ceberio, & Lozano, 2018). These are classified as local trajectory optimisation methods and require an initial guess of the control profile.

Neuroevolution (NE) offers a promising alternative to conventional optimisation methods (Conway, 2010; Dachwald, 2005). NE combines evolutionary algorithms (EAs) with artificial neural networks (ANNs) and has shown success in optimising various trajectories (Galván & Stapleton, 2023), ranging from autonomous vehicles (Grigorescu et al., 2019) to autonomous robots (Jalali et al., 2020). NE has also been applied to optimise spacecraft trajectories (Dachwald, Ohndorf, & Wie, 2006; Galván & Stapleton, 2023; Wetherell, 2022). NEs have two main advantages over direct and indirect optimisation methods: they require no initial guess and are more likely to locate a global optimum rather than getting trapped in a local optimum, classifying them as a global optimisation method (Dachwald, 2005). One such method is InTrance (Intelligent Trajectory optimization using neurocontroller evolution), a smart global trajectory optimisation approach (Dachwald, 2005). InTrance trains a single ANN, functioning as a neurocontroller (NC), to produce a near-optimal steering strategy for a specific transfer problem. An EA is used to evolve the ANN, allowing InTrance to find near-optimal steering strategies without needing an initial trajectory guess. In this work, InTrance is utilised as an optimiser; however, since it was originally developed for interplanetary trajectory optimisation, it needs to be adapted for use in proximity operations.

In this section, the working principles of InTrance are explained, and the modifications made to the method are detailed. First, the fundamentals of ANNs are discussed, followed by an exploration of spacecraft steering using NE. Next, the fitness assignment for the hold and homing trajectory are presented, after which EAs are examined. Finally, it is explained how these components integrate to form an Evolutionary Neurocontroller (ENC).

### 2.3.1. Artificial Neural Networks

Artificial Neural Networks (ANNs) are interconnected groups of nodes modelled after the human brain, allowing them to be analogue, fault-tolerant, and adaptable (Caudill & Butler, 1990). ANNs are used in artificial intelligence to recognise patterns based on previous training. They can be applied in a multitude of fields including, but not limited to, word-, image-, and speech recognition, forecasting,

machine translation, and medical diagnosis (Swingler, 1996; Wu and Feng, 2018; Ketkar et al., 2021; Samek et al., 2021).

ANNs are composed of processing elements called neurons, which model the basic functions of biological neurons (Dachwald, 2005). There are two types of ANNs: feed-forward neural networks (FNNs), also known as multi-layer neural networks and recurrent neural networks. ANNs are usually structured and consist of multiple layers of neurons. In FNNs, layers are organised, so connections flow only from the previous layer to the next. In recurrent ANNs, this flow order does not exist, and nodes can form loops. The first layer, the input layer, consists of input neurons responsible for receiving the networks input data, as can be seen in Figure 9. Conversely, the last layer, called the output layer, consists of output neurons that produce the output of the network. The intermediate layers and their respective neurons located between the input and output layers are called hidden layers and hidden neurons.

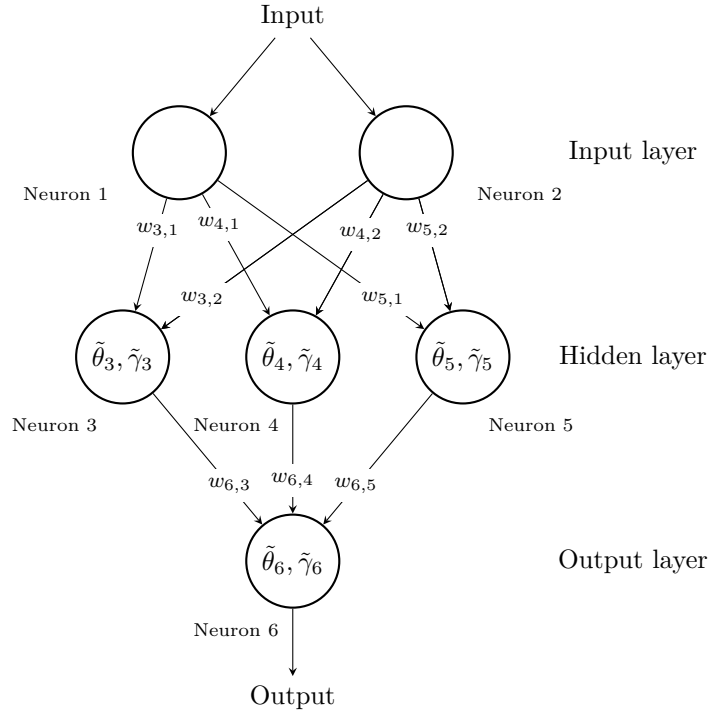


**Figure 9:** Layered feed-forward artificial neural network

Each neuron has an activation function that maps the neuron's weighted input values onto a single output value (Dachwald, 2005). Various activation functions, such as a binary step function, Tanh, ReLU, or Sigmoid function, can be used (Sharma, Sharma, & Athaiya, 2017). In this work the Sigmoid activation function  $s_{\tilde{\gamma}} : \mathbb{R} \mapsto (0,1)$  is used, which is defined as

$$s_{\tilde{\gamma}}(x) = \frac{1}{1 + e^{-x/\tilde{\gamma}}} , \quad (2.3.1)$$

where the temperature parameter  $\tilde{\gamma}$  describes the slope of the function. Thus, a layered FNN can be described as a directed graph in which each node (neuron)  $i$  in a layer performs the function

$$y_i = \frac{1}{1 + e^{\sum_j w_{ij} y_j - \tilde{\theta}_i / \tilde{\gamma}_i}}, \quad (2.3.2)$$

where  $y_i \in (0,1)$  is the output of neuron  $i$ , and  $y_j$  the output values of the neurons  $j$  in the previous layer (Dachwald, 2005).  $w_{ij}$  are the connection weights between the neurons  $j$  and neuron  $i$  and  $\tilde{\theta}$  is the bias or threshold of neuron  $i$ .

### 2.3.2. Spacecraft Steering Using a Neurocontroller

ANNs can serve as NCs providing near-optimal steering strategies for specific transfer problems by determining the optimal control vector  $\hat{\lambda}(t)$ , utilising environmental data in the process (Dachwald, 2005). Since InTrance was originally designed for interplanetary transfers, it is necessary to adapt the input of the NC for effective use in proximity operations.

#### Neurocontroller Input

The NC must have knowledge of both the chaser and target spacecraft states to generate appropriate control commands. Additionally, because solar sails rely on solar radiation pressure for propulsion, information about the relative position of the chaser to the Sun in the co-moving frame might also be necessary. This includes the Sun-sail unit vector and an eclipse factor to account for periods when the spacecraft is in Earth's shadow.

Therefore, the NC utilises the following environmental information:

1. State of the Chaser:
  - GEI Frame:  $\mathbf{X}_C(t)$
  - Co-Moving Frame:  $\mathbf{x}_C(t)$
2. Targeted State:
  - Co-Moving Frame:  $\mathbf{x}_T(t)$
3. Sun-Sail Unit Vector in the Co-Moving Frame:  $\hat{\mathbf{u}}(t)$
4. Eclipse Factor:  $E(t) \in 0, 1$

The **eclipse factor**  $E(t)$  indicates whether the chaser is illuminated by the Sun ( $E(t) = 1$ ) or is in Earth's shadow ( $E(t) = 0$ ). These inputs were specifically chosen to capture the environmental factors that influence the motion of the sail during proximity operation and to effectively guide it to the target. The inputs can be used in various combinations, with the restriction that if the Sun-sail unit vector  $\hat{\mathbf{u}}(t)$  or the eclipse factor  $E(t)$  is included, at least one state variable of the chaser must also be present to provide context for the NC. In total, there are 17 possible input sets derived from different combinations of these inputs. However, the optimal set of inputs for the NC is problem-dependent and may vary based on optimisation objectives, necessitating parameter tuning (see Figure A.5).

#### Neurocontroller Output

The NC outputs a three-dimensional vector  $\lambda_{\text{NC}} \in (0,1)^3$ , which is used to compute  $\hat{\lambda}$  (Dachwald, 2005):

$$\lambda_{\text{scaled}} = 2\lambda_{\text{NC}} - 1 \quad (2.3.3)$$

$$\hat{\lambda} = \frac{\lambda_{\text{scaled}}}{|\lambda_{\text{scaled}}|} \quad (2.3.4)$$

In this formulation, the NC generates a steering vector without implicit knowledge of locally optimal spacecraft steering, categorising it as a direct steering strategy. From  $\hat{\lambda}$ , the constrained sail control angles can be calculated as explained in subsection 2.1.3. Subsequently, the spacecraft's trajectory can be propagated from the current state using the calculated control angles. Figure 10 illustrates an example of a sailcraft steering strategy. The NC receives the chaser's state in the co-moving frame along with the eclipse factor as inputs and outputs the three-dimensional vector  $\lambda_{\text{NC}}$ .

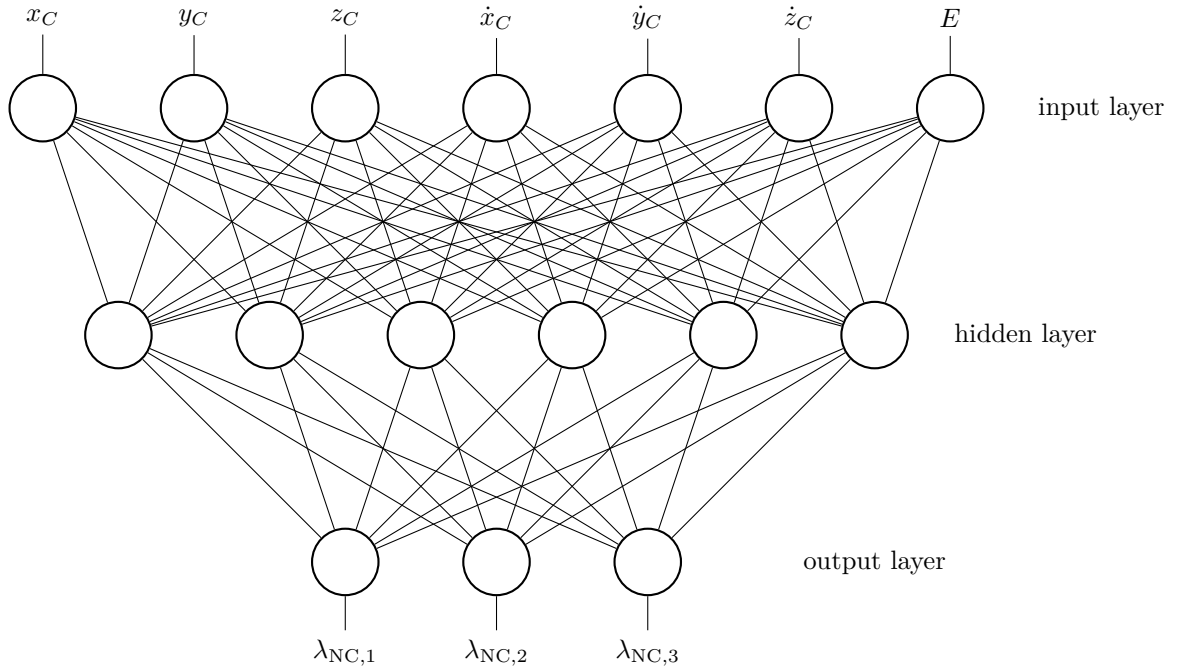


Figure 10: NC for direct steering of a solar-sailcraft

### 2.3.3. Neurocontroller Fitness Assignment

In this work, two types of proximity trajectories are investigated: hold trajectories and homing trajectories. Each trajectory type has different objectives, necessitating the development of specific fitness functions to evaluate optimality.

#### Hold Trajectory Optimisation

For the hold trajectory optimisation, the objective is to maximise the time the chaser spends inside the hold volume to allow for a prolonged stay relative to the target without immediately drifting away. Therefore, the fitness function  $J$  is formulated to quantify this performance based on the chaser's duration within the defined hold volume. The fitness function  $J$  can be expressed as:

$$J = \int_{t_0}^{t_f} \mathbb{1}_{\text{inside}}(t) dt \quad (2.3.5)$$

where  $\mathbb{1}_{\text{inside}}(t)$  is an indicator function.

For the encircling hold trajectory, the chaser must stay between the two defined ellipsoids. Thus, the indicator function is defined as:

$$\mathbb{1}_{\text{inside}}(t) = \begin{cases} 1, & \text{if } \frac{(x_C(t)-x_0)^2}{a_i^2} + \frac{(y_C(t)-y_0)^2}{b_i^2} + \frac{(z_C(t)-z_0)^2}{c_i^2} \geq 1 \\ & \text{and } \frac{(x_C(t)-x_0)^2}{a_o^2} + \frac{(y_C(t)-y_0)^2}{b_o^2} + \frac{(z_C(t)-z_0)^2}{c_o^2} \leq 1, \\ 0, & \text{otherwise.} \end{cases} \quad (2.3.6)$$

In this formulation:

- $(x_0, y_0, z_0)$  is the common centre of the ellipsoids.
- The ellipsoid parameters  $a_i, b_i, c_i$  and  $a_o, b_o, c_o$  define the size and shape of the inner and outer ellipsoids, respectively.

For the leading/trailing hold trajectory, the sail only needs to stay within the volume confined by a single ellipsoid. Thus, the indicator function simplifies to:

$$\mathbb{1}_{\text{inside}}(t) = \begin{cases} 1, & \text{and } \frac{(x_C(t)-x_0)^2}{a_o^2} + \frac{(y_C(t)-y_0)^2}{b_o^2} + \frac{(z_C(t)-z_0)^2}{c_o^2} \leq 1, \\ 0, & \text{otherwise.} \end{cases} \quad (2.3.7)$$

In practice, the evaluation of this fitness function is performed by discretising the mission time interval  $[t_0, t_f]$  into small time steps  $\Delta t$ . The integral is approximated by summing the indicator function values over these discrete time steps:

$$J \approx \sum_{k=0}^{N-1} \mathbb{1}_{\text{inside}}(t_k) \Delta t \quad (2.3.8)$$

where  $N$  is the total number of discrete time steps, and  $t_k$  is the time point at step  $k$ .

### Homing Trajectory Optimisation

The primary goal of the homing phase for proximity operations using a solar sail is to reach a designated hold trajectory. Homing typically begins at a range of tens of kilometres from the target and must seamlessly transition onto the hold trajectory.

To successfully merge onto a hold trajectory, several requirements must be met:

- **Minimising State Deviation:** The sail's position and velocity at the end of the homing trajectory should closely match those of the targeted state of the hold trajectory at the point of merging.
- **Aligning Sail Attitude:** The sail's orientation upon arrival should match the attitude of the targeted state of the hold trajectory to ensure a smooth transition.
- **Reducing Time of Flight:** The homing trajectory should be optimised for efficiency, minimising the time to reach the hold volume.

When targeting a predefined hold trajectory, minimising the state deviation between the final state of the homing trajectory and a state on the hold trajectory involves two components. On the one hand, the state deviation in the co-moving frame, representing the relative position and velocity with respect

to the target, needs to be minimised. On the other hand, each co-moving state on the hold trajectory corresponds to a specific state in the inertial frame. Therefore, targeting only the co-moving state may result in the sail reaching the correct relative position and attitude but at an incorrect location in inertial space, thereby failing to merge onto the intended hold trajectory. In such a case, the resulting trajectory would have the same semi-major axis and eccentricity as the targeted hold trajectory but might differ in the argument of periapsis. This dual requirement complicates the optimisation process because both the co-moving and inertial states must be aligned to merge onto the hold trajectory successfully. To reduce complexity and simplify the optimisation, the optimisation process used in this study targets only the co-moving states, including their respective sail attitudes, during the homing phase. By doing so, it can be assessed whether InTrance can effectively optimise homing trajectories to achieve the desired relative position and orientation required for the hold trajectory, even if the inertial alignment is not perfect.

The optimisation problem used in this study, thus, involves three key objectives:

1. Minimise Transfer Time: The transfer time  $T = t_f - t_0$  should be minimised to reduce mission duration (Dachwald, 2005).
2. Minimise Final Relative Position and Velocity: At the final time  $t_f$ , the relative position and velocity should be minimised, measured by  $\Delta r_f = |\mathbf{r}_T(t_f) - \mathbf{r}_C(t_f)|$  and  $\Delta v_f = |\mathbf{v}_T(t_f) - \mathbf{v}_C(t_f)|$  (Dachwald, 2005).
3. Minimise Discrepancy in Sail Attitude: At the final time  $t_f$ , the angle  $\Omega_f$  between the sail normal vector of the chaser  $\hat{\mathbf{n}}_{C,f}$  and the sail normal vector of the targeted state on the hold trajectory  $\hat{\mathbf{n}}_{T,f}$  should be minimised to allow for a seamless transfer between homing and hold trajectory.

Given practical limitations, the terminal constraints ( $\Delta r_f = 0 \text{ m}$ ,  $\Delta v_f = 0 \text{ m/s}$ ) may not be perfectly achieved, necessitating the definition of maximum allowable errors:  $\Delta r_{f,\max}$  and  $\Delta v_{f,\max}$  (Dachwald, 2005). The final relative position and velocity are normalised with respect to their maximum allowable values:

$$\Delta R_f = \frac{\Delta r_f}{\Delta r_{f,\max}} \quad \Delta V_f = \frac{\Delta v_f}{\Delta v_{f,\max}} \quad (2.3.9)$$

The fulfilment of the terminal constraints is assessed for each previously provided state on the hold trajectory. The feasibility of the trajectory is quantified by:

$$\Delta X = \sqrt{\frac{1}{2}(\Delta R^2 + \Delta V^2)}. \quad (2.3.10)$$

Importantly,  $\Delta r_f$  and  $\Delta v_f$  are not the relative distance and velocity at the end of the integration period. Instead, they are measured at the time  $t$  when  $\Delta X$  is minimal during the maximum allowable transfer time  $T_{\max}$ . This approach ensures that the optimal proximity to the hold trajectory is considered across all possible states.

The fitness function  $J(T, \Delta r_f, \Delta v_f, \Omega_f)$  is constructed from several sub-fitness components:

1. Primary Sub-Fitness Function:

$$J_T = 1000 \left( 1 - \frac{T}{T_{\max}} \right) \quad (2.3.11)$$

$J_T$  penalises longer transfer times.

2. Secondary Sub-Fitness Functions:

$$J_r = \log \left( \frac{1}{\Delta R_f} \right) \quad J_v = \log \left( \frac{1}{\Delta V_f} \right) \quad (2.3.12)$$

$J_r$  and  $J_v$  measure the accuracy of the final position and velocity. They yield positive values if accuracy requirements are met and negative values otherwise.

3. Tertiary Sub-Fitness Function:

$$J_\Omega = 100/\Omega_f \quad (2.3.13)$$

$J_\Omega$  rewards smaller dispersions between  $\hat{\mathbf{n}}_{C,f}$  and  $\hat{\mathbf{n}}_{T,f}$ .

4. Conditional Adjustment of  $J_T$

$$J'_T = \begin{cases} J_T, & \text{if } J_r \geq 0 \text{ and } J_v \geq 0 \\ 0, & \text{otherwise} \end{cases} \quad (2.3.14)$$

5. Conditional Adjustment of  $J_\Omega$

$$J'_\Omega = \begin{cases} J_\Omega, & \text{if } J_r \geq 0 \text{ and } J_v \geq 0 \\ 0, & \text{otherwise} \end{cases} \quad (2.3.15)$$

6. Overall Fitness Function: The complete fitness function is defined as:

$$J(T, \Delta r_f, \Delta v_f) = J'_T + \frac{1}{\sqrt{2 \max(\Delta R_f, \Delta V_f)^2}} + J'_\Omega \quad (2.3.16)$$

This means that  $J_T$  and  $J_\Omega$  are only awarded once the maximum allowable position and velocity errors are met. This way, the optimiser can first focus on minimising the distance and relative velocity to the targeted state.

### 2.3.4. Evolutionary Algorithms

EAs are a class of optimisation techniques inspired by the principles of natural evolution, including selection, mutation, recombination, and survival of the fittest (Bäck & Schwefel, 1993). These algorithms are particularly effective for solving complex optimisation problems where traditional methods may struggle, particularly in the presence of large, nonlinear, or multi-modal search spaces. EAs have been successfully applied across various fields such as engineering, economics, artificial intelligence, and biology, making them versatile tools for optimisation.

The core idea behind EAs is to mimic the evolutionary processes observed in nature to find optimal or near-optimal solutions to complex problems (Dachwald, 2005). The algorithm begins with an initial population of candidate solutions, often generated randomly. Each individual in the population represents a possible solution to the problem and is typically encoded as a string of variables, often referred to as chromosomes. The fitness of each individual is evaluated using a predefined fitness function, which quantifies how well the individual solves the problem at hand.

The evolutionary process is driven by a cycle of selection, reproduction, mutation, and replacement. During selection, individuals are chosen from the population based on their fitness, with fitter individuals having a larger probability of being selected. This selection process mimics the survival of the fittest principle, ensuring that better solutions are more likely to contribute to the next generation. Reproduction involves the creation of new individuals through the recombination (or crossover) of selected parent individuals (see Figure 11). This process combines the genetic information of two or more parents to produce offspring that inherit characteristics from both. Recombination is crucial for exploring new regions of the search space and combining advantageous traits from different individuals. Mutation introduces random changes to the individuals' genomes, which helps to maintain genetic diversity within the population and prevents premature convergence to sub-optimal solutions. Mutation ensures that the search process can explore a wide range of possible solutions and escape local optima. After reproduction and mutation, the new generation of individuals replaces the old population, and the cycle repeats. Over successive generations, the population is expected to evolve towards better solutions, with the fittest individuals gradually dominating the population.

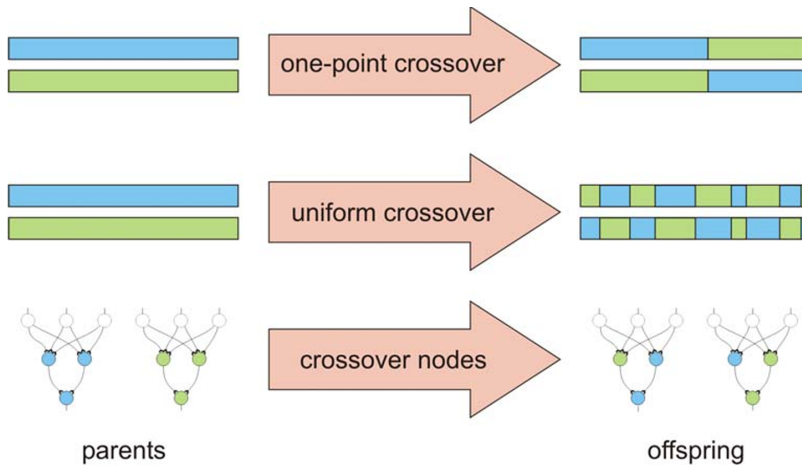


Figure 11: Evolutionary Operators Implemented in InTrance (Dachwald, 2005)

### 2.3.5. Evolutionary Neurocontrol

InTrance employs an ENC to determine an optimal steering strategy for a low-thrust spacecraft, combining ANNs with EAs (Dachwald, 2005).

#### Evolutionary Neurocontroller Design

The ENC integrates two key loops: an outer optimisation loop and an inner trajectory integration loop, as depicted in Figure 12. In the outer loop, the EA manages a population of randomly initialised NCs, denoted as  $\pi_1, \dots, \pi_q$ . Each NC generates a steering strategy  $\mathbf{u}(t)$  in the inner loop, which results in a spacecraft trajectory  $\mathbf{x}_{SC}(t)$ . The fitness of each trajectory is assessed using a fitness function, assigning

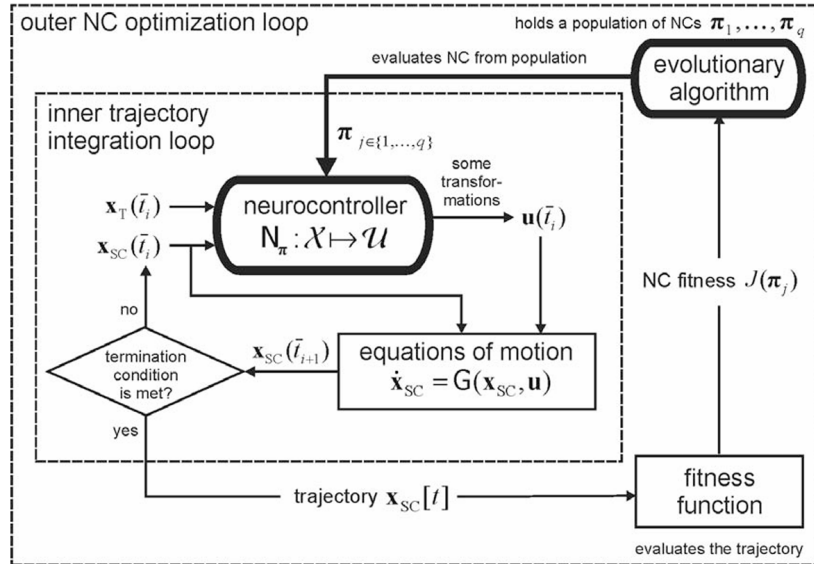


Figure 12: Trajectory Optimisation Using Evolutionary Neurocontrol

a fitness value  $J(\pi_j)$  to each NC, as explained in subsection 2.3.3.

The EA is used to find an NC representing an optimal steering strategy, resulting in an optimal trajectory. For this, a so-called one-at-a-time reproduction is used. The EA makes use of the fact that the parameters of an NC can be mapped onto a string, also called gene, which provides an equivalent description of the NCs network function, as can be seen in Figure 13.

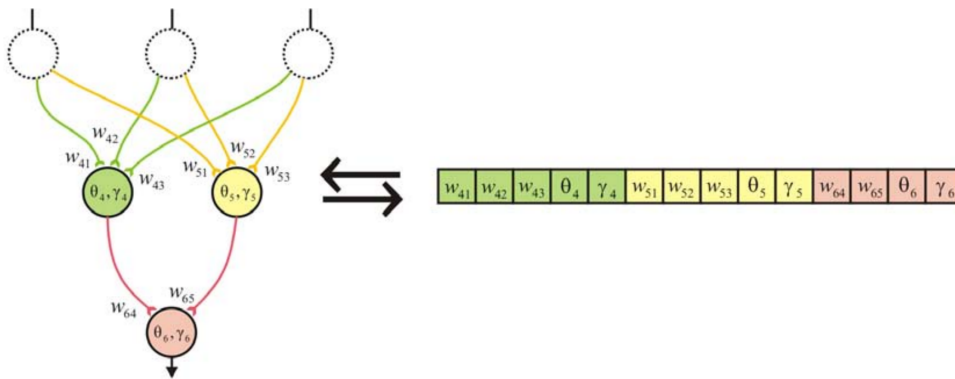


Figure 13: Mapping of an ANN on a (real-value) string (Dachwald, 2005)

For the one-at-a-time reproduction (Figure 14), two pairs of NCs are randomly selected from the population and their fitness values are compared. The two winners are used to generate offspring through crossover operators. The offspring's trajectories are evaluated, and new fitness values are assigned. The new offspring then replace the two losers. This process continues until the fitness value converges.

### Real Delta Coding

To optimise the NC, the search space, visualised as a hypercube where each dimension represents an NC weight, must be efficiently explored. To enhance precision and convergence in this high-dimensional space, the Real Delta Coding (RDC) algorithm is used in InTrance (Dachwald, 2005). RDC is an

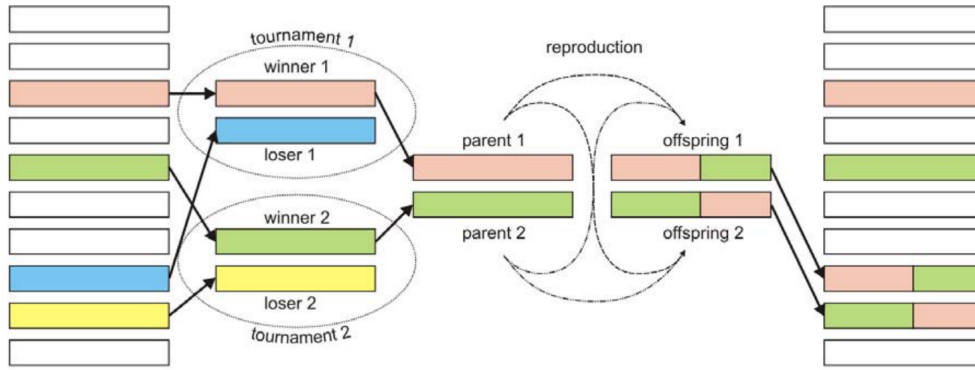


Figure 14: One-at-a-time reproduction with tournament selection (Dachwald, 2005)

iterative search algorithm tailored for real-valued optimisation problems like adjusting NC weights. It operates in cycles called epochs, during which a dynamically selected subspace of the total search space is explored, centred around the current best solution. This focused search strategy allows RDC to efficiently hone in on optimal or near-optimal solutions while avoiding premature convergence to local optima. RDC maintains a balance between exploring and exploiting the search space by periodically re-initialising the population and adapting the search space based on diversity metrics. This approach enhances the overall optimisation process, leading to improved NC performance. The working principle of RDC is illustrated in Figure 15.

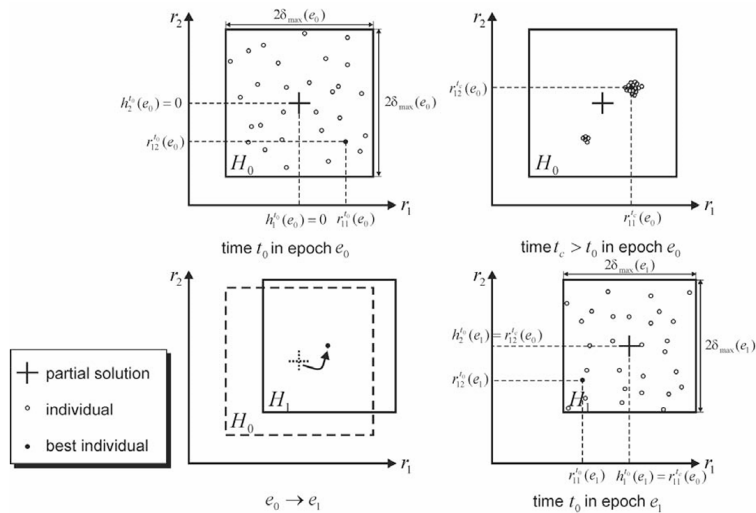


Figure 15: Real Delta Coding (Dachwald, 2005)

In the initial epoch ( $e_0$ ), the search subspace ( $H_0$ ) is centred at the origin, with the population initialised randomly. The EA then runs until an epochal convergence criterion is met based on the relative improvement of the most recent solutions. If the improvement is below a predefined threshold, the population is considered converged. After convergence in epoch  $e_0$ , the best-found solution becomes the centre for the next subspace ( $H_1$ ), Furthermore, the search area is reduced in size as well. This process of shifting and reducing the hypercube repeats in subsequent epochs, progressively narrowing the search space to hone in on the optimal solution. RDC does not include an expansion mechanism, ensuring a consistent focus on increasingly refined search areas. The process continues until the final RDC convergence criterion is met, effectively achieving a gradient search behaviour (Dachwald, 2005).

The RDC convergence criterion, similar to the epochal convergence criterion, is based on the relative improvement between subsequent epochs. To ensure robustness, the initial epoch is performed multiple times with different randomly generated populations, known as search space scan epochs. The best solution from these initial scans is then used as the starting point for subsequent epochs.

For the homing trajectory optimisation, RDC is used without modifications. However, for the hold trajectory optimisation, RDC is adapted to account for the specific conditions of the problem. In this scenario, a maximum time of flight (ToF) is predefined. If a steering strategy is found that keeps the spacecraft within the hold volume for the entire duration of this ToF, further optimisation becomes unnecessary as the fitness can no longer increase. Consequently, the optimisation process is stopped as soon as such a solution is found.

## 2.4. Simulation and Optimisation Setup

Throughout this work, the SRP force acting on the solar sail of the chaser spacecraft is simulated using the ideal sail model, as described in subsection 2.1.1. This model assumes a perfectly reflecting sail where the SRP force is always aligned with the sail's normal vector. To maximise the chaser's thrust in the desired, locally optimal thrust direction, a locally optimal steering law is employed, following the approach outlined in subsection 2.1.2. When attitude constraints are imposed, such as limitations on the maximum cone angle or angular rate, the calculation of the sail's optimal control angles is adapted accordingly, as detailed in subsection 2.1.3. To assess a lightness number achievable with current state-of-the-art technology, the lightness number of the ACS3 (Wilkie & Fernandez, 2023) mission is adopted. Throughout this work, a lightness number of  $\beta = 7.7 \times 10^{-3}$  is used for the solar sail. Just as ACS3, the altitude of the target orbit through this work chosen to be 1000 km.

The motion of the chaser is propagated using the CW equations, as described in subsection 2.2.4. The CW equations provide a linearized model of the relative motion of a spacecraft in close proximity to a reference orbit, assuming a circular orbit and small relative distances. The target spacecraft is assumed to be in a circular orbit, influenced only by Earth's point mass gravity. Therefore, the central angle it covers over a given time interval can be calculated using its mean motion, allowing the determination of its position at any given time. A simplified environmental model is employed, with no additional perturbations such as atmospheric drag, J2 effect, or third-body gravitational influences. A cylindrical shadow model is used to determine eclipse periods, as described in subsection 2.2.5. This simplified model allows focus on the primary effects of SRP on the solar sail without the added complexity of modelling additional perturbing forces.

The optimisation of the hold and homing trajectories is conducted using InTrance, an intelligent spacecraft trajectory optimisation tool that employs neurocontroller evolution to determine optimal control laws. The specific settings and parameters used in InTrance for optimising the hold trajectories are provided in Appendix B. The input to the NC is based on the parameter tuning results from Figure A.5. For the hold trajectory optimisation, the NC receives the sails inertial Cartesian state, co-moving state, and the Sun-sail vector in the frame  $M$  as input variables. For the homing trajectory optimisation, the NC receives the sail's inertial Cartesian state and its co-moving state as inputs.

# 3

## Characteristics of Solar Sail Relative Motion

As there is no prior research focusing on solar sail proximity operations and their relative motion, it is essential to first understand the characteristics of a solar sail's relative motion, governed by its unique dynamics, before exploring proximity operations using solar sails. This knowledge is important for designing effective and safe proximity trajectories, such as hold trajectories, in ADR missions. While a variety of analyses could be conducted to explore the impact of different factors on the relative motion, such as orbital altitude, eccentricity, inclination, and the sail's lightness number, due to the limited time frame of this work, the analysis focuses on the relative motion within the orbital plane of the target at a constant altitude and a circular orbit. This simplification allows the problem to be more manageable while still capturing the key dynamics involved.

The chapter begins by introducing a test case that analyses the relative motion of a solar sail in proximity to a target object. This test case serves as a baseline to understand the fundamental behaviours of a solar sail under specific conditions. Furthermore, the test case serves as a reference point from which variations can be systematically explored. Subsequently, two parametric analyses are conducted to provide deeper insights into solar sail relative motion:

- **Effect of Initial True Anomaly ( $\theta_0$ ):** Effect of Initial True Anomaly ( $\theta_0$ ): The first analysis examines how varying the sail's initial true anomaly affects its trajectory relative to the target while keeping the cone angle constant at  $\alpha = 0^\circ$ .
- **Impact of Varying Cone Angles:** The second analysis explores how different cone angles affect the sail's relative motion, considering two scenarios: one with a positive clock angle of  $\delta = 90^\circ$  and another with a negative clock angle of  $\delta = -90^\circ$ . The cone angle is an important parameter because a solar sail's thrust is inherently limited, and adjusting the sail's attitude (specifically the cone angle) is the primary means of controlling thrust magnitude and direction. Focusing on cone angle variations allows for an understanding of how attitude adjustments can be used to manage in-plane motion effectively.

Since this analysis focuses on in-plane motion, varying the clock angle is not examined. The decision to concentrate on the cone angle rather than the clock angle is supported by the characteristics of the CW equation (see Eq. 2.2.2), which demonstrates that motion in the z-direction is decoupled from motion in the x/y plane. Therefore, investigating in-plane effects can be effectively accomplished by varying the cone angle, thereby simplifying the analysis.

For all analyses conducted in this chapter, the target is assumed to be in a circular, equatorial orbit with an altitude of 1000 km. This orbit is chosen because most debris objects are located in LEO (Bonnal & McKnight, 2017), and the ACS3 mission operates at this altitude (Wilkie & Fernandez, 2023), providing a relevant reference. At the beginning of the simulation, the sail and the target have identical initial state vectors, positioning the sail on the same orbit as the target at the origin of the co-moving frame. A lightness number of  $\beta = 7.7 \times 10^{-3}$  is used for the sail, consistent with the ACS3 mission parameters, as stated in Section 2.4. The sail maintains a constant attitude throughout the simulation, which simplifies the analysis and isolates the effects of the parameters under investigation. The sail's motion is simulated over ten revolutions of the target, with a step size of one second.

### 3.1. Test Case

For the test case, both the chaser and the target have an initial true anomaly of  $\theta_0 = 0^\circ$ , locating them behind Earth as seen from the Sun, as shown in Figure 16. The sail maintains a constant attitude throughout the simulation with a cone angle of  $\alpha = 0^\circ$ ; thus, the SRP force vector is aligned with the incident sunlight and lays in the orbital plane of the target. As a result, the sail moves only within the target's orbital plane. Figure 17 illustrates the sail's trajectory in the co-moving frame.

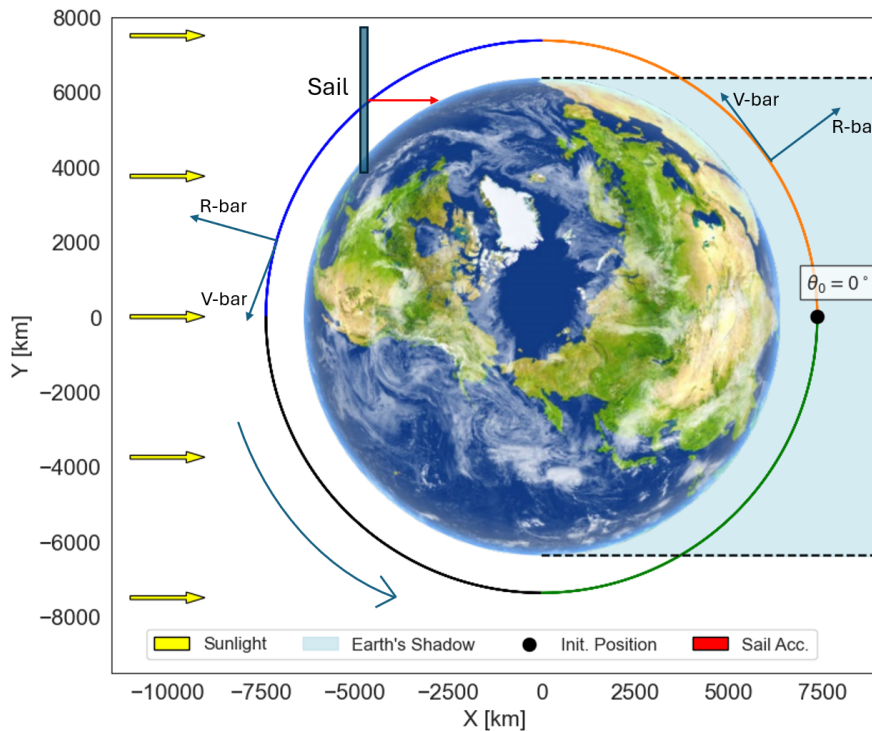


**Figure 16:** Trajectory of the chaser for the test case in the GEI frame, highlighting different trajectory sections for discussion.

At the start of the simulation, the chaser moves along the circular target orbit (highlighted in orange

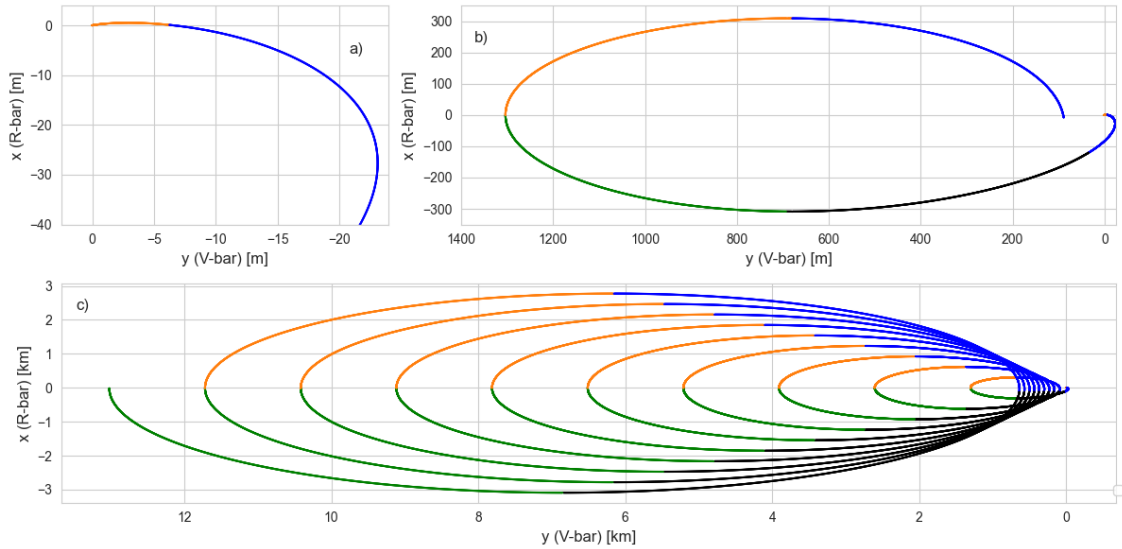


**Figure 17:** Trajectory of the chaser for the test case in the co-moving frame, highlighting different trajectory sections for discussion: a) beginning of the movement; b) 1.5 Revolutions; c) 10 revolutions.

in Figure 16), but since it is in Earth's shadow, no SRP force is acting on it. Consequently, the chaser remains stationary in the co-moving frame at its origin. Once the chaser emerges from Earth's shadow, the SRP force begins to act on it. As the sail is moving toward the Sun, the SRP acceleration has a component opposite to its velocity, causing a decrease in its orbital velocity, as depicted in Figure 18. As a result, the chaser falls behind the target in the co-moving frame (see Figure 17 a), orange arc). Simultaneously, the SRP acceleration has an outward radial component, leading to an initial movement of the chaser above the target. However, the chaser transitions onto a slightly elliptical orbit due to the reduced orbital velocity, as shown in Figure 19, with a lower periapsis than the initial circular orbit. Additionally, the acceleration component opposing the velocity reduces the chaser's orbital energy (see Figure 20). As the sail flies towards its periapsis (blue arc), its orbital altitude decreases, causing movement in the negative R-bar direction below the target. At the same time, the orbital velocity increases, leading to reduced motion in the negative V-bar direction and a subsequent motion in the opposite direction towards the target, eventually overtaking it. During this phase, the sail is still moving toward the Sun, and the SRP acceleration continues to have a component opposing the velocity, further reducing its orbital energy.

After half a revolution, the chaser spacecraft begins moving away from the Sun (highlighted in black), resulting in an acceleration component in the direction of its velocity. This causes an increase in orbital energy and raises the apoapsis above the altitude of the target orbit, further increasing the eccentricity. As the sail approaches periapsis, its altitude decreases while its velocity increases. The sail reaches periapsis after approximately three-quarters of a revolution (transition between black and green arcs), marking its lowest point relative to the target during the revolution. This appears as a minimum along the R-bar direction, as seen in the co-moving frame. At periapsis, the sail attains its highest orbital velocity and maximum velocity relative to the target during the first revolution. As the sail ascends toward apoapsis (see Figure 16 and Figure 17 b), green arc), its altitude increases while its orbital velocity decreases. This results in movement in the positive R-bar direction and a decelerating movement in the positive V-bar direction. Until the sail enters Earth's shadow, the SRP acceleration continues to have a component in the velocity direction, increasing the sail's orbital energy

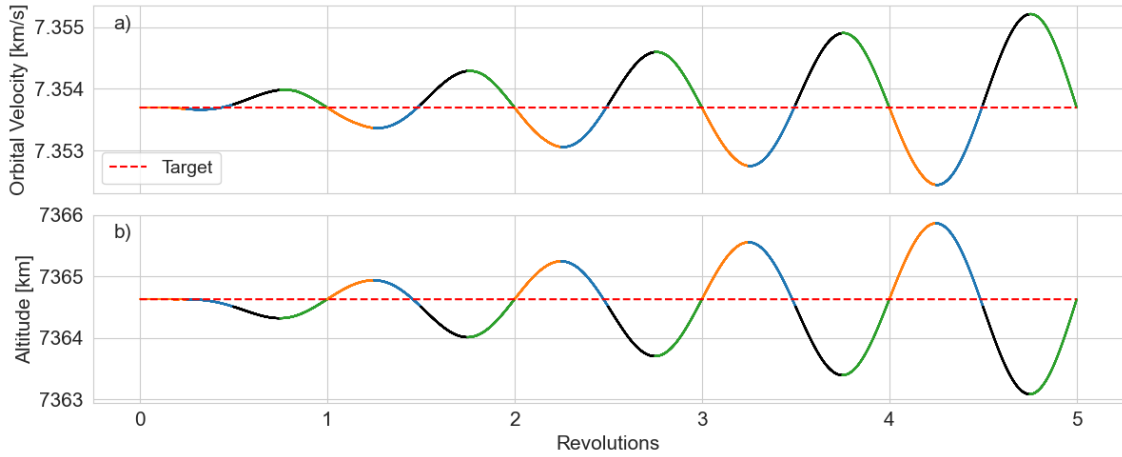


**Figure 18:** a) altitude and b) orbital velocity for the test case, highlighting different sections for discussion.

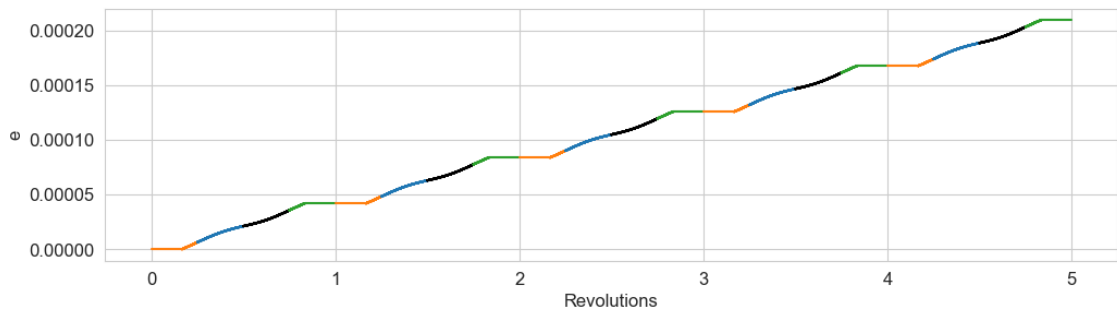


**Figure 19:** Eccentricity of the trajectory of the test case, highlighting different sections for discussion.

back toward its initial value. Once the sail enters Earth's shadow, it coasts without SRP acceleration toward apoapsis. After completing one full revolution (transition between green and orange arcs), the sail crosses the target orbit. At this point, the relative velocity component along the V-bar direction is zero, and the sail is positioned directly ahead of the target along the V-bar axis. The sail remains below the target throughout the first revolution, as seen in the co-moving frame.

At the beginning of the second revolution, after orbit crossing (see Figure 16 and Figure 17 b), orange arc), the sail continues to coast toward apoapsis. Now, at a higher altitude than the target, the sail has a lower orbital velocity relative to the target, causing it to move in the negative V-bar direction, moving back toward the target. As the sail's altitude increases, it moves further in the positive R-bar direction above the target. Once the sail exits Earth's shadow, as it flies towards the Sun, the SRP acceleration acts again in the opposing direction of the sail's velocity vector, decreasing its orbital energy and lowering its periapsis. The sail's velocity decreases further, reaching a minimum at apoapsis (transition between orange and blue arcs), where its relative velocity to the target also reaches a minimum. After passing apoapsis (blue arc), the sail's orbital velocity increases as it moves toward periapsis, reducing its motion in the negative V-bar direction and causing it to descend toward the target. Eventually, the sail's orbital velocity exceeds the target's, resulting in movement in the positive V-bar direction (transition between blue and black arcs after the first revolution). As the sail moves away from the Sun (black and green arcs), the SRP acceleration points in the direction of its velocity, increasing its orbital energy back to its initial value and raising the apoapsis. From Figure 17, it can be observed that starting from the second revolution, the sail traces a full ellipse in the co-moving frame during

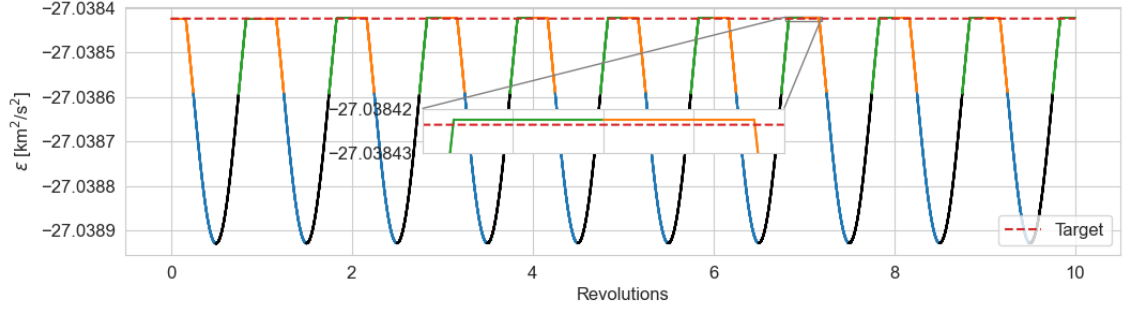


**Figure 20:** Orbital energy of the chaser of the test case, highlighting different sections for discussion.

each revolution, whereas during the first revolution, only half of the ellipse was covered. Consequently, after each revolution starting from the second, the chaser reaches a position furthest from the target ahead of it along the V-bar.

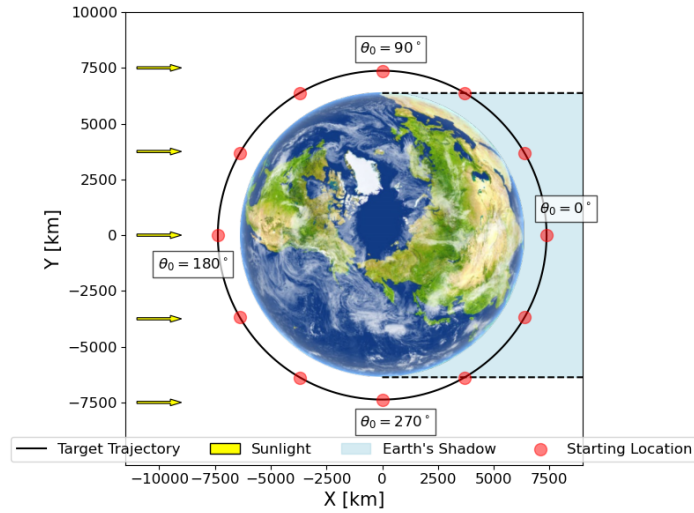
During this test case, as the sail flies toward the Sun, its periapsis decreases, and when it flies away from the Sun, its apoapsis increases. This leads to a gradual increase in eccentricity. In the co-moving frame, this is evident as the lowest (periapsis) and highest (apoapsis) points of the trajectory decrease and increase, respectively, with each revolution. These continuous changes result in higher and lower orbital velocities of the sail relative to the target at these points, causing faster movement in both positive and negative V-bar and R-bar directions, thus covering more distance (see Figure 17). Consequently, the point of orbit crossing, when the sail ascends toward apoapsis (moving upward relative to the target, now referred to as the left orbit crossing), shifts progressively ahead of the target. Furthermore, it can be observed that the orbit crossing at which the sail descends towards periapsis (moving downward relative to the target, now denoted as the right orbit crossing) shifts in the positive V-bar direction as well.

The general movement in the positive V-bar direction can also be explained by the change in orbital energy,  $\varepsilon = -\frac{\mu_{\oplus}}{2\tilde{a}}$ , where  $\tilde{a}$  is the semi-major axis. The relationship between orbital energy and orbital period  $T$  is given by  $T = 2\pi\sqrt{\frac{\tilde{a}^3}{\mu_{\oplus}}} = 2\pi\sqrt{\frac{\mu_{\oplus}^2}{8\varepsilon^3}}$ . Therefore, a lower orbital energy results in a shorter orbital period, and vice versa. From Figure 20, it can be seen that, over one revolution, the sail's orbital energy first decreases and then increases back to nearly its initial value. However, the cumulative orbital energy remains lower than the target's, leading to a shorter orbital period and a forward movement relative to the target.

## 3.2. Initial True Anomaly Analysis

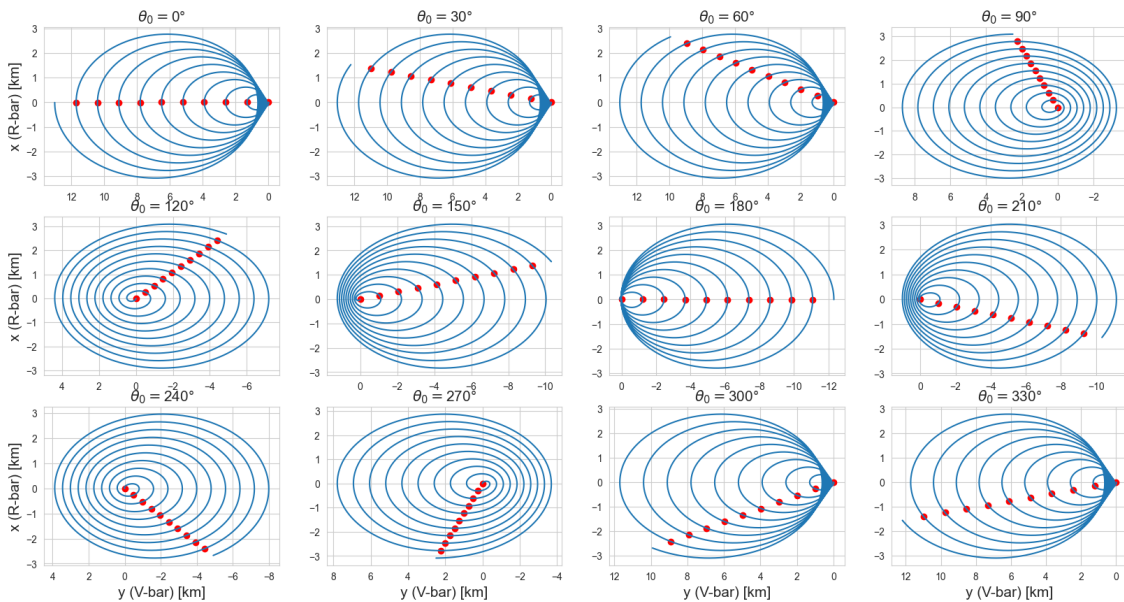
The following parametric analysis investigates how different initial true anomalies  $\theta_0$  affect the motion of a solar sail relative to a target while maintaining a constant cone angle of  $\alpha = 0^\circ$ . Twelve different starting positions are investigated, equally spaced at intervals of  $30^\circ$  starting from  $\theta_0 = 0^\circ$ , as shown in Figure 21.

Figure 22 shows the trajectories in the co-moving frame for all twelve investigated initial positions, with red dots indicating the position of the sail after the target completes one revolution. The first case,  $\theta_0 = 0^\circ$ , represents the test case as discussed in Section 3.1. For initial angles  $\theta_0 = 0^\circ, 30^\circ, 60^\circ, 300^\circ$  and  $330^\circ$ , it can be seen that the trajectories are largely identical. In these



**Figure 21:** Initial positions of the chaser for investigating the impact of different true anomalies on the relative motion of a solar sail.

cases, the sail's initial position is inside Earth's shadow. While in Earth's shadow, the sail experiences no SRP acceleration and thus remains stationary at the origin of the co-moving frame and coasts along its circular starting orbit. Only after emerging from the shadow does the SRP act on the sail, initiating the motion as seen in the co-moving frame. This leads to the same acceleration profile and, consequently, to the same trajectory. The only difference is the sail's position along the trajectory after each revolution of the target (indicated as red dots in Figure 22). Each case is propagated for ten revolutions, but the timing of the sail's emergence from Earth's shadow varies. For  $\theta_0 = 60^\circ$ , the sail exits the shadow shortly after the propagation begins, whereas, for  $\theta_0 = 300^\circ$ , the sail remains in Earth's shadow for nearly one-third of a revolution before emerging. Consequently, while the motion starts at the same point on the target orbit, it begins at different times during the propagation.



**Figure 22:** Relative motion of a solar sail for different initial true anomaly values.

As  $\theta_0$  increases, once the initial location is outside of Earth's shadow, the positions of both orbit crossings move in the negative V-bar direction until  $\theta_0 = 180^\circ$ , where all left orbit crossings are located close to the target. Thus, the general motion of the sail shifts from moving in the positive V-bar direction to the negative V-bar direction. This shift can be explained by the decreasing duration during which the SRP acceleration acts against the sail's velocity direction before acting towards it as  $\theta_0$  increases from  $0^\circ$  to  $180^\circ$ . As an example, the trajectory of the chaser in the GEI frame and in the co-moving frame, as well as its orbital energy over time for the case  $\theta_0 = 120^\circ$  are shown in Figure 23, Figure 24 and Figure 20 respectively. After the start of the simulation, the sail flies towards the Sun for the first sixth of a revolution (red arc), leading to a reduction in orbital energy and a decrease of the periapsis due to a reduced orbital velocity. This leads to a backwards and downward motion of the sail, as seen in the co-moving frame. However, the decrease of orbital velocity and energy is less than the test case's (see Figure 20); as far as the test case, the SRP acceleration acted approximately two-thirds of a revolution against the velocity direction. Consequently, the periapsis of case  $\theta_0 = 120^\circ$  has a higher altitude, and the drift in the positive V-bar direction is reduced, placing the left orbit crossing closer to the target. Once the sail is flying away from the Sun (black and green arc), its apoapsis increases until it flies into the shadow of Earth. As the sail ascends towards its apoapsis, it starts to move in the negative V-bar direction and eventually moves behind the target, which places the right orbit crossing behind the target. As the sail flies towards the Sun (orange, blue and red arc), the orbital energy is reduced, and the periapsis decreases. The shift of both orbit crossings becomes more pronounced for larger  $\theta_0$ , as the duration in which the SRP acceleration acts against the sail's velocity direction before acting towards it decreases, gradually causing the orbit crossings to move in the negative V-bar direction.

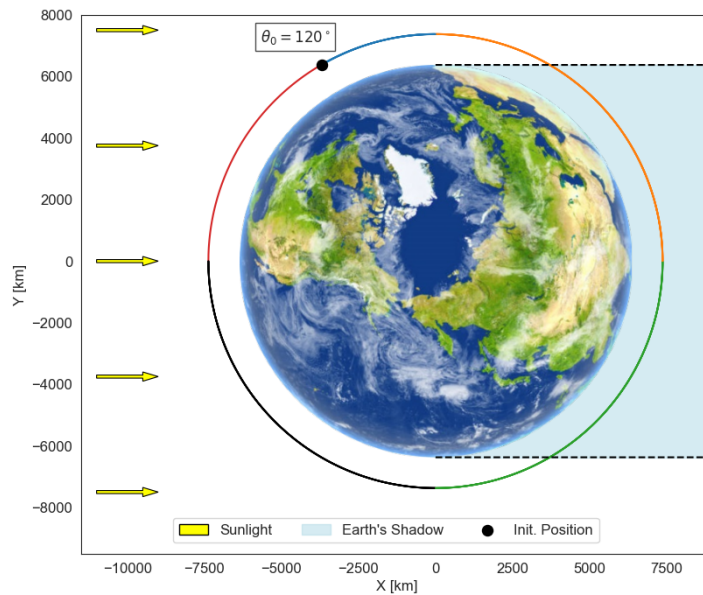


**Figure 23:** Trajectory of the chaser for  $\theta_0 = 120^\circ$  case in the GEI frame, highlighting different trajectory sections for discussion.

For a starting location of  $\theta_0 = 180^\circ$ , the sail is flying away from the Sun at the start of the simulation, leading to an increase in orbital energy and an initial increase in orbital velocity, increasing the apoapsis. Thus, the sail moves above and behind the target. Only after the sail emerges from Earth's shadow does the periapsis lower, leading to a drift back towards the target. Thus, during the first revolution. As  $\theta_0$  increases further, it can be seen that both orbit crossings move back towards the positive V-bar

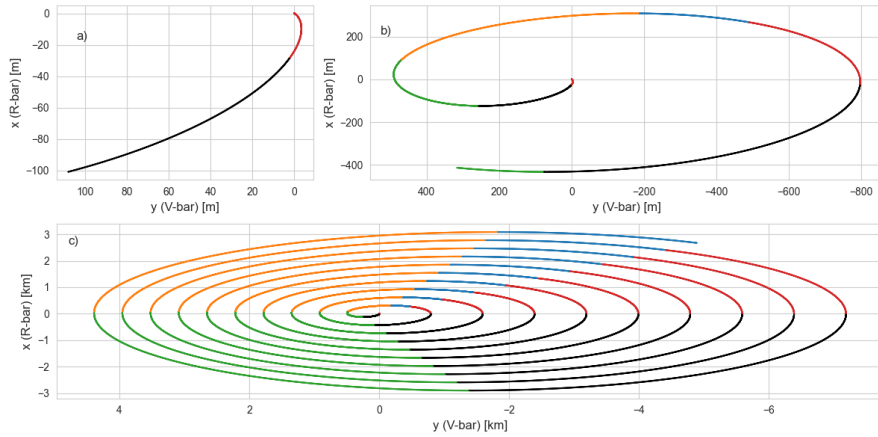


**Figure 24:** Trajectory of the chaser for case  $\theta_0 = 120^\circ$  in the co-moving frame, highlighting different trajectory sections for discussion: a) beginning of the movement; b) 1.5 Revolutions; c) 10 revolutions.

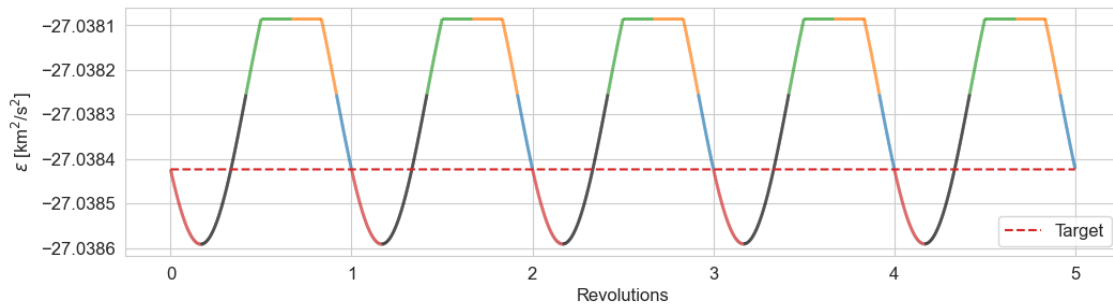


**Figure 25:** Orbital energy of the chaser of the test case, highlighting different sections for discussion.

direction until the starting location is again located in Earth's shadow. This is because the duration at which the SRP acceleration points in the direction of the velocity direction decreases before acting against it.

The analysis conducted in this section focused on varying the initial location of the chaser along the target orbit while keeping the sail's attitude constant with a cone angle of  $\alpha = 0^\circ$ , to assess the impact on the sail's motion relative to the target. It was observed that when the initial position is located in Earth's shadow, the resulting trajectory remains the same: with each revolution, the left orbit crossing moves further ahead of the target, and the periapsis and apoapsis decrease and increase, respectively. However, if the initial position is not in Earth's shadow, it affects the relative motion of the sail with respect to the target. As the initial true anomaly increases, both orbit crossings move in the negative V-bar direction, with the right orbit crossing reaching its maximum extent at a true anomaly of  $\theta_0 = 0^\circ$ . As the true anomaly increases further, the orbit crossings shift back in the positive V-bar direction.

This behaviour highlights the sensitivity of the sail's relative motion to its initial conditions when starting outside Earth's shadow. Changes in the initial true anomaly can lead to significant differences in the sail's trajectory relative to the target. This sensitivity has implications for mission planning and operational safety, especially when the sail is close to the target in its orbit:

- **Impact on Mating and Docking Operations:** Precise control over the sail's relative position is crucial during mating and docking procedures to avoid collisions and successfully capture the

debris object.

- **Influence on Departure Operations:** For departure manoeuvres, the sail's initial position can determine the ease with which it can safely distance itself from the target without unintended close approaches.
- **Utilisation in Trajectory Design:** By strategically choosing the initial true anomaly, mission planners can exploit this sensitivity to achieve desired relative motions without altering the sail's attitude. This could reduce the need for complex manoeuvres and conserve resources.

However, this sensitivity also means that unintended deviations from the planned initial conditions could lead to unfavourable trajectories, potentially increasing collision risks or requiring additional corrective manoeuvres. Therefore, accurate navigation, timing, and control are essential to account for and mitigate the effects of initial condition sensitivity.

The analysis in this section focused on varying the initial location of the chaser along the target orbit while keeping the attitude of the sail constant, with a cone angle of  $\alpha = 0^\circ$  and assessing the impact on the sail's motion relative to a target. It is observed that the resulting trajectory, when the initial position is located in Earth's shadow, is the same. With each revolution, the left orbit crossing moves further ahead of the target, while the periapsis and apoapsis decrease and increase, respectively. However, if the initial position is not located in Earth's shadow, it influences the relative motion of the target. As the initial true anomaly increases, both orbit crossings move in a negative  $V$ -bar direction, where the right orbit crossing is reaching its maximum extent at a true anomaly of  $\theta_0 = 0^\circ$ . As the true anomaly increases further, the orbit crossings move back in the positive  $V$ -bar direction. This behaviour could have an effect on and influence mating and docking as well as departure operations, as the sail will be in the same orbit as the target.

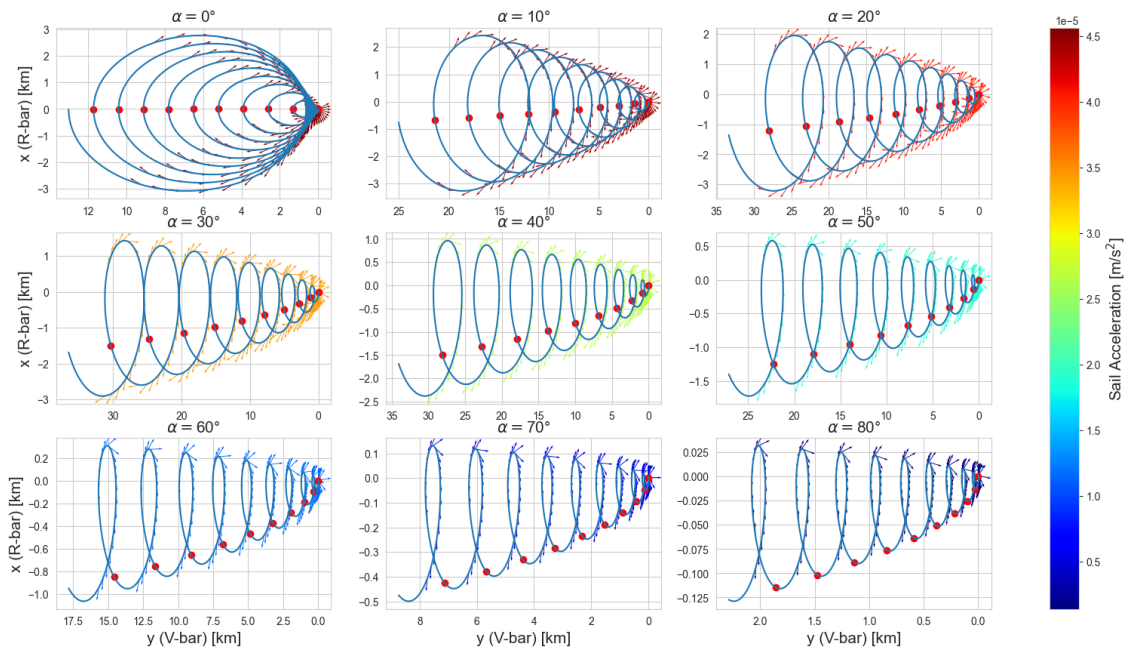
### 3.3. Cone Angle Analysis

For a solar sail, the only way to control the thrust magnitude and direction is by adjusting its attitude through changes in the cone and clock angles. Understanding how these attitude adjustments affect the sail's motion relative to a target is important for designing proximity operations in ADR missions. This section presents a parametric analysis investigating the impact of varying sail attitudes on its relative motion. Since this analysis focuses on the in-plane motion within the target's orbital plane, two specific cases are considered: one with a positive clock angle of  $\delta = 90^\circ$  and another with a negative clock angle of  $\delta = -90^\circ$ . These clock angles confine the sail's motion to the orbital plane, simplifying the analysis of in-plane dynamics.

For each of these two cases, nine different cone angles are investigated, ranging from  $\alpha = 0^\circ$  to  $\alpha = 80^\circ$  in increments of  $10^\circ$ . The case with  $\alpha = 0^\circ$  corresponds to the test case described in Section 3.1. For these analyses, the sail maintains a constant attitude throughout, and both the chaser and the target begin with an initial true anomaly of  $\theta_0 = 0^\circ$ . Furthermore, as the previous analysis in Section 3.2 revealed a sensitivity of the sail's relative motion to its initial position along the target's orbit, an additional investigation is conducted to examine the effects of varying the initial true anomaly. Specifically, for both the positive and negative clock angle cases, the sail's motion is analysed with increasing values of  $\theta_0 = 0^\circ$  at a constant cone angle of  $\alpha = 10^\circ$ .

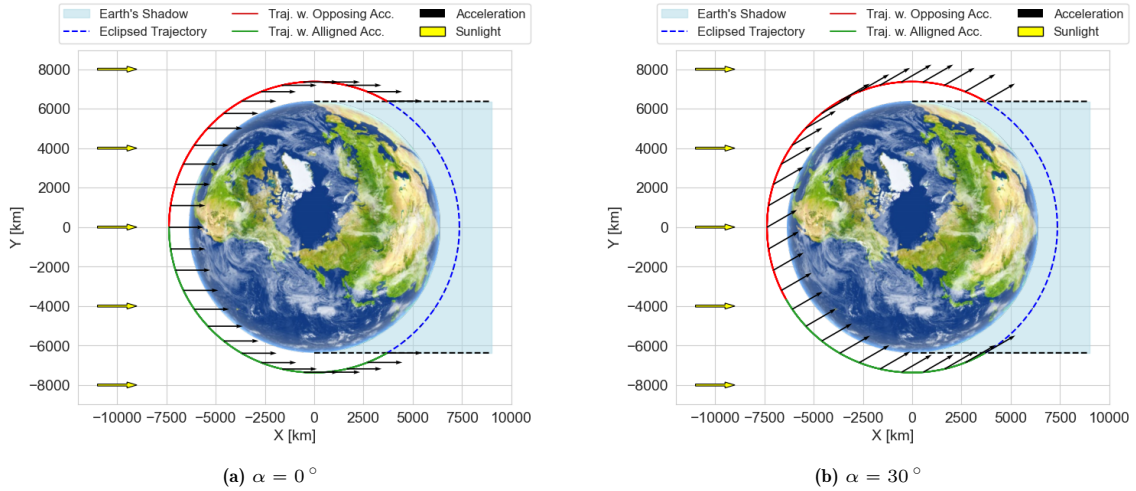
### 3.3.1. Positive Clock Angle

Figure 26 illustrates the relative motion of a solar sail for various constant cone angles at a constant clock angle of  $\delta = 90^\circ$ . As  $\alpha$  increases up to  $40^\circ$ , the sail covers more distance in the positive V-bar direction. This occurs because, during each revolution, the duration I, which the SRP acceleration opposes, increases the sail's velocity vector. In contrast, the duration when it aligns with the velocity vector decreases, as this part of the trajectory is now more eclipsed. An example is shown in Figure 27 for a cone angle of  $\alpha = 0^\circ$  and  $30^\circ$ . Consequently, the periapsis decreases faster than the apoapsis increases, as the lowest point of the trajectory decreases more rapidly than the highest point increases, as seen in the co-moving frame. This results in the sail having a higher relative velocity relative to the initial orbit at periapsis than at apoapsis, causing it to cover less distance when moving in the negative V-bar direction and more distance when moving in the positive V-bar direction. Therefore, the right orbit crossing shifts in the positive V-bar direction. However, as the cone angle continues to increase, the overall acceleration on the sail decreases, leading to slower changes in the sail's velocity and the periapsis and apoapsis altitudes. This reduction in acceleration leads to less distance covered in the V-bar direction. These two opposing effects, the increased distance due to longer periods of opposing acceleration and the decreased distance due to reduced overall acceleration, work against each other and initially result in more forward movement. However, beyond a cone angle of  $\alpha = 40^\circ$ , the reduced acceleration becomes the dominant factor, causing the total distance covered in the positive V-bar direction to decrease.



**Figure 26:** Relative motion of a solar sail for various cone angles for a constant clock angle of  $\delta = 90^\circ$ .

An alternative explanation involves changes in orbital energy and their impact on the orbital period. During each revolution, the sail's orbital energy first decreases and then increases as the SRP acceleration acts against and then along the velocity vector, respectively. However, because the sail spends more time decelerating than accelerating (due to longer periods of opposing acceleration), the net orbital energy does not return to its initial value but remains lower, as can be seen in Figure 28 for a cone angle of  $\alpha = 30^\circ$ . This gradual decrease in orbital energy reduces the semi-major axis and orbital period, resulting in a generally higher orbital velocity, shifting the trajectory in the positive V-bar direction. As



**Figure 27:** Trajectory for a constant sail attitude with  $\delta = 90^\circ$ , highlighting the part where the acceleration vector has a component opposing the velocity vector and where it aligns with the velocity vector for a)  $\alpha = 0^\circ$ ; b)  $\alpha = 30^\circ$

the cone angle increases, the rate of orbital energy decrease slows due to a lower acceleration, leading to less distance covered in the positive V-bar direction.

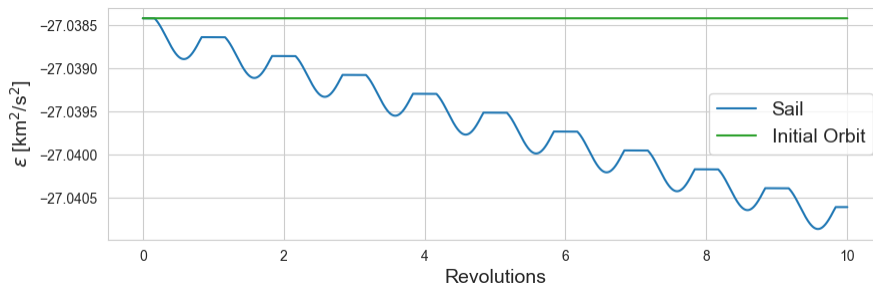


**Figure 28:** Orbital Energy of a solar sail with a constant sail attitude of  $\alpha = 30^\circ$  and  $\delta = 90^\circ$  and a starting location of  $\theta_0 = 0^\circ$ .

The initial position along the orbit,  $\theta_0$ , influences the sail's relative motion, as shown in the previous section. Figure 29 shows the relative motion of a sail with constant cone and clock angles of  $\alpha = 10^\circ$  and  $\delta = 90^\circ$ , respectively, for increasing values of  $\theta_0$ . It is noted that starting positions within Earth's shadow yield identical trajectories. As  $\theta_0$  increases up to  $180^\circ$ , the left orbit crossing in the first few revolutions shifts in the negative V-bar direction before eventually drifting in the opposite direction. This behaviour results from the interplay of two factors: first, the duration during which the SRP acceleration acts against the sail's velocity vector before switching to oppose it decreases, causing the right orbit crossing to move in negative V-bar direction (as explained in Section 3.2); second, the gradual reduction in the semi-major axis leads to a lower orbital period, allowing the sail to cover more distance in the positive V-bar direction. Thus, when the initial true anomaly increases further, the right orbit crossing moves back in the positive V-bar direction.

### 3.3.2. Negative Clock Angle

At a negative clock angle of  $-90^\circ$ , the trajectories of the solar sail for various cone angles are displayed in Figure 30. Similar to the positive clock angle case, the sail's relative motion is influenced by the duration during which the SRP acceleration aligns with or opposes its velocity vector. However, instead of longer

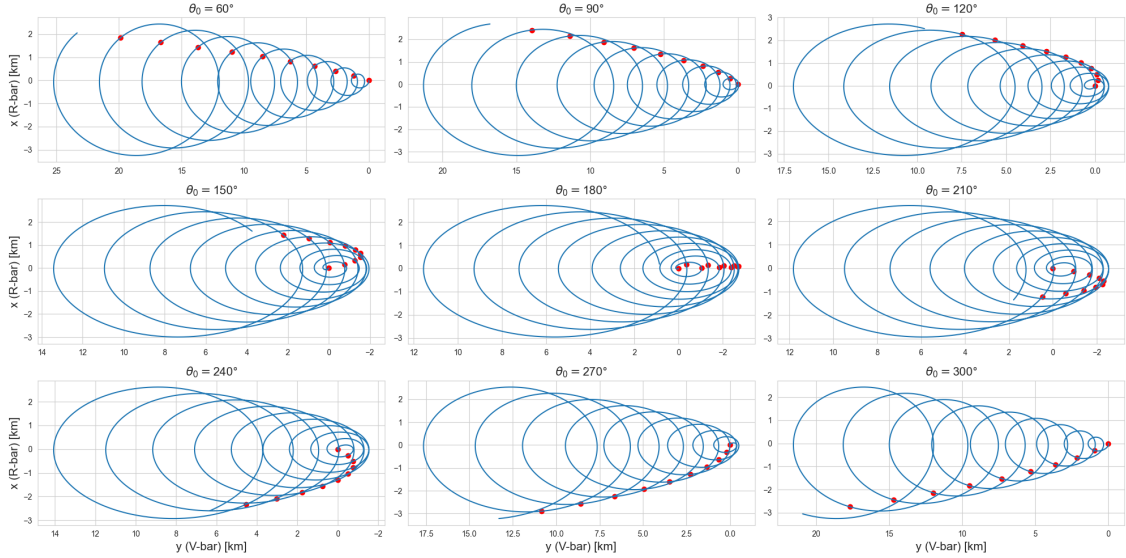


**Figure 29:** Relative motion of a solar sail with a constant cone and clock angle of  $\alpha = 10^\circ$  and  $\delta = 90^\circ$ , respectively, for increasing  $\theta_0$ .

periods of opposing acceleration, the sail experiences extended periods where the SRP acceleration has a component in the velocity direction. In this scenario, the sail initially moves forward in the positive V-bar direction due to flying towards the Sun, as discussed in the test case (see Section 3.1). For cone angles up to  $\alpha = 40^\circ$ , the sail eventually drifts behind the target, covering increasing distances in the negative V-bar direction. This behaviour occurs because, with increasing cone angles, the sail spends more time with the SRP acceleration aligned with its velocity vector, leading to a gradual increase in orbital energy and semi-major axis. Consequently, the altitude of the apoapsis increases faster than the periapsis decreases, causing the sail to lag behind the target in the co-moving frame. For cone angles above  $\alpha = 40^\circ$ , the distance covered in the negative V-bar direction decreases due to the reduced overall acceleration, similar to the effect observed in the positive clock angle case.

Figure 31 shows the relative motion of a sail for various  $\theta_0$  with a constant cone and clock angle of  $\alpha = 10^\circ$  and  $\delta = -90^\circ$ , respectively. It is again noted that starting locations positioned within Earth's shadow show identical trajectories. It can be seen that, while the initial true anomaly is increasing to  $\theta_0 = 180^\circ$ , the forward movement of the left orbit crossing decreases, shifting in the negative V-bar direction, resulting in a pure motion of the sail behind the target. Further increasing the initial true anomaly leads to a shift back in front of the target. For a positive clock angle of  $\delta = 90^\circ$ , it was the exact opposite. The general movement was in the positive V-bar direction, and the distance covered by the backward motion of the right orbit crossing had its maximum for  $\theta_0 = 180^\circ$ . However, the cause is the same and thus will not be restated.

### 3.4. Discussion

The purpose of the parametric analyses conducted in Section 3.2 and Section 3.3 was to gain insight into how the unique dynamics of a solar sail influence its relative motion during proximity operations with a target spacecraft. This section summarises the key findings and discusses their implications, particularly in the context of solar-sail far-range rendezvous operations.

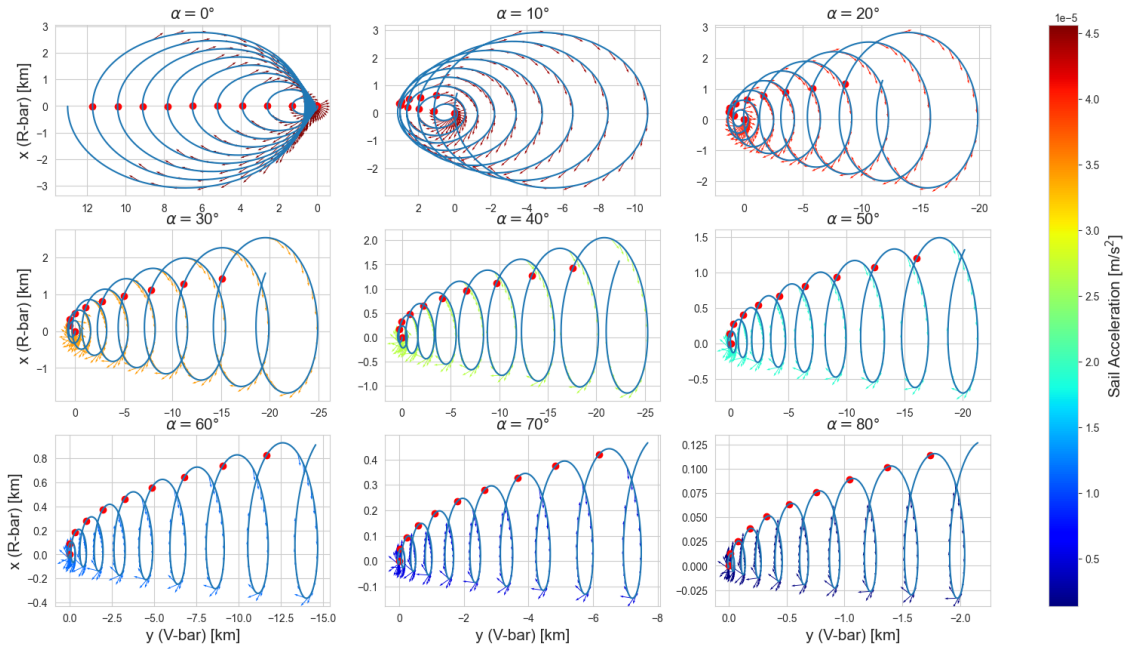


**Figure 30:** Relative motion of a solar sail for various cone angles for a constant clock angle of  $\delta = -90^\circ$ .

## Key Findings

Two parametric analyses were conducted: the first examined the effect of varying the initial true anomaly while keeping the sail cone angle constant, and the second explored the impact of different cone angles at constant clock angles. The key observations from these analyses are as follows:

- When the chaser is positioned below the target, it always moves in the positive V-bar direction, and vice versa; when it is located above the target, it moves in the negative V-bar direction.
- A lower periapsis of the chasers orbit results in more distance covered in the V-bar direction, and vice versa; a higher apoapsis allows the sail to cover more distance in the V-bar direction.
- As the chaser moves from apoapsis to periapsis, it travels in the negative R-bar direction, and the reverse occurs when moving from periapsis to apoapsis.
- At orbit crossings, the chasers velocity vector points in the positive R-bar direction at the left orbit crossing and in the negative R-bar direction at the right orbit crossing.

These findings are consistent with existing literature on proximity operations (Curtis, 2013; Fehse, 2003; Wakker, 2015).

## Solar-Sail Specific Observations

The analyses also revealed unique behaviours specific to solar-sail dynamics:

- The initial position of the solar sail on the target orbit significantly influences its relative motion, especially when part of its trajectory is eclipsed.
- For a constant sail attitude with a negative clock angle, both orbit crossings eventually drift in the negative V-bar direction. In contrast, the drift is in the positive V-bar direction for a positive clock angle.

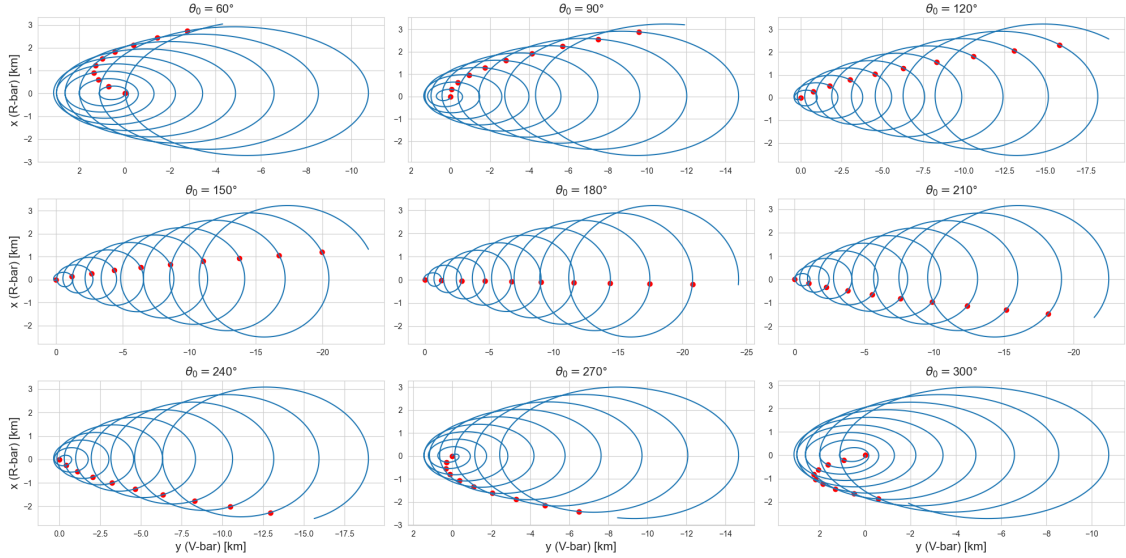


**Figure 31:** Relative motion of a solar sail with a constant cone and clock angle of  $\alpha = 10^\circ$  and  $\delta = -90^\circ$ , respectively, for increasing  $\theta_0$ .

- For a constant sail attitude with a positive clock angle, the semi-major axis continuously decreases, while for a negative clock angle, the semi-major axis continuously increases.
- As cone angles increase, the distance covered in the positive or negative V-bar direction first increases and then decreases.
- With larger cone angles, the periapsis decreases, and the apoapsis increases more slowly.
- For positive clock angles and an initial position of  $\theta_0 = 180^\circ$ , the right orbit crossing initially moves in the negative V-bar direction before shifting to the positive direction. This shift diminishes as  $\theta_0$  increases or decreases from this point. The inverse holds true for negative clock angles, where the most pronounced forward movement is observed at  $\theta_0 = 0^\circ$ .

However, it is important to note that the continuous decrease and increase for a constant sail attitude with a positive and negative clock angle, respectively, only occur when the sail's trajectory is partially eclipsed, as it depends on longer or shorter periods of opposing acceleration. Thus, it is expected that this effect would diminish for trajectories with a higher altitude, where less of the trajectory is eclipsed.

### Implications for Far-Range Rendezvous Operations

The findings from the parametric analyses have implications for designing hold and homing trajectories during far-range rendezvous operations with solar sails. The unique dynamics of solar sails, particularly their sensitivity to sail attitude and initial conditions, must be carefully considered to ensure mission success and operational safety.

One key observation is that a solar sail with a constant attitude and a positive or negative clock angle will drift away from the target due to the continuous increase or decrease of its semi-major axis. Specifically, for smaller cone angles, the sail covers more distance in the co-moving frame compared to higher cone angles, owing to the higher magnitude of the SRP acceleration. This means that the sail's relative motion is strongly influenced by its attitude, and by adjusting the cone angle, the rate and direction of drift can be controlled. To minimise unwanted drift during hold trajectories and keep the sail close to

the target within a designated hold volume, adopting a control profile with higher cone angles can be effective. Higher cone angles reduce the overall SRP acceleration, leading to slower changes in the sail's orbital elements and allowing the sail to stay in proximity to the target for a longer period of time.

Even if the semi-major axis returns to its initial value after one revolution, as is the case for a constant cone angle of  $\alpha = 0^\circ$ , the sail's eccentricity increases continuously, causing the sail to gradually distance itself from the target over time. Despite this, it could be possible to design trajectories where the sail moves in an elliptical motion around the target effectively performing a fly-around manoeuvre. As observed in Figure 22, cases with initial true anomalies between  $90^\circ$  and  $270^\circ$ , the sail remains in proximity to the target for an extended period of time, allowing for continuous observation.

For homing trajectories, the ability to induce drift in either the positive or negative V-bar direction by lowering or raising the sail's semi-major axis is particularly valuable. If far-range rendezvous operations start from an injection point located on the target orbit behind the target, reducing the semi-major axis can allow the sail to catch up to the target. Conversely, increasing the semi-major axis can help the sail lag behind the target if approaching from ahead. However, eventually, the semi-major axis should be matched with the target's to allow for a merge onto a hold trajectory, to reduce the drift and not too overshoot the target.

Safety remains a crucial part of planning far range rendezvous operations, as any risk of unintentionally passing the target closely or even colliding with it should be reduced. Even in the event of a malfunction the sail should be moving away from, or at least not get closer to the target. To mitigate this risk, the hold trajectory could be positioned ahead of or behind the target, creating a leading or trailing hold trajectory. By adopting a control profile with purely positive or negative clock angles, it can be ensured that the sail, when keeping a constant attitude, will eventually drift away from the target. This could be especially useful in cases of emergency, where the sail needs to distance itself from the target, by maintaining the current attitude, and thus reducing the risk of collision. However, it was shown that even with such a constant control profile, the sail could first drift towards the target, before moving away from it. Thus, while positioning the hold trajectory closer to the target improves observation capabilities, it requires balancing the distance to prevent the sail from drifting too close. The distance of the hold trajectory to the target should be based on the sail's potential drift distance when stuck in a specific orientation.

In summary, the analyses highlight the importance of understanding solar-sail dynamics and their sensitivity to sail attitude and initial conditions in the context of far-range rendezvous operations. By leveraging these dynamics through careful trajectory design and attitude control, mission planners can enhance safety and effectiveness in solar sail proximity operations.

# 4

## Hold Trajectory Analysis

Classical hold points are not feasible in solar sail proximity operations, as discussed in subsection 2.2.3. Due to the sail's large size, forces from atmospheric drag or SRP, especially if the sail is not positioned edge-wise to the Sun, will cause the sail to drift away from a fixed hold point. As an alternative, a hold trajectory is proposed, which allows the sailcraft to manoeuvre continuously, compensating for SRP and other perturbations while remaining in proximity to the target for an extended period. This approach keeps the sail close to the target and enables ongoing observation, system checks, and preparation for close-range rendezvous operations. In this chapter, the viability of such hold trajectories is explored.

Two types of hold trajectories are evaluated: encircling hold trajectories and leading/trailing hold trajectories. The encircling hold trajectory involves the sailcraft orbiting around the target, allowing for comprehensive observation from multiple angles, while the leading/trailing hold trajectory positions the sail ahead of or behind the target along the orbital path, offering safety advantages by reducing the risk of collision.

The chapter is structured as follows: first, the experimental setup is explained in Section 4.1, detailing the simulation parameters, the target and sail characteristics, and the initial conditions. Next, the analysis of the encircling hold trajectory is presented in Section 4.2, by first discussing a test case, followed by a parametric analysis of cone angle and turning rate restrictions. This is followed by an examination of the leading/trailing hold trajectory in Section 4.3, where the analysis is extended to clock angle constraints and an analysis where all constraints are combined. The safety of the optimised trajectories is assessed in Section 4.4, considering potential risks and emergency scenarios. Finally, the chapter concludes with a discussion of the results in Section 4.5, summarising the key findings and their implications for solar-sail far-range rendezvous operations.

### 4.1. Experiment Setup

This section describes the experimental setup used to analyse the hold trajectories for the solar sail.

The target object is assumed to be in a circular, equatorial low-Earth orbit at an altitude of 1000 km.

Unless otherwise stated, the target has an initial true anomaly of  $\theta_0 = 0^\circ$ , positioning it directly behind the Earth as viewed from the Sun. The sail has a lightness number of  $\beta = 7.7 \times 10^{-3}$ . Although InTrance does not require an initial guess for the steering strategy, the current implementation must provide the sail's initial state. The sail is initially placed in a Keplerian elliptical orbit with the same orbital period as the target. This elliptical orbit lies within the designated hold volume, and its eccentricity is determined by the size of the hold volume; larger hold volumes require a larger eccentricity. The sail's initial position is located along the negative x-axis, as seen in the co-moving frame, positioning the sail directly below the target.

Two types of hold trajectories, encircling and leading/trailing hold trajectories, are investigated by first examining a nominal case and then conducting a parametric analysis. The constraint conditions for each analysis are summarised in Table 1. For the nominal test cases, no constraints are imposed on the sail's attitude or turning rate. In this unconstrained scenario, the sail could, in theory, follow a Keplerian orbit while maintaining an edge-on orientation relative to the Sun. However, since the sail aims to maximise the time it remains within a dedicated hold volume over a finite amount of time, there is flexibility in its manoeuvring, and multiple control profiles can satisfy this condition. It is worth noting that as the hold volume becomes increasingly small and approaches the dimensions of the Keplerian orbit, only an edge-on attitude would allow the sail to stay within it indefinitely (see Figure A.5).

Analysis	$\alpha_{\max}$ [ $^\circ$ ]	$\Omega_{\max}$ [ $^\circ/\text{s}$ ]	$\delta$ [ $^\circ$ ]
Test Case	-	-	$\in [-180; 180)$
Cone Angle	60,65,70,75,80,85	-	$\in [-180; 180)$
Turning Rate	70	0.1, 0.25, 0.5, 1 and 2	$\in [-180; 180)$
Clock Angle	60,65,70,75,80,85	-	$\in (1; 179)$ and $\in (-179; -1)$
Combined	70	0.1, 0.25, 0.5, 1 and 2	$\in (1; 179)$ and $\in (-179; -1)$

**Table 1:** Constraint conditions for hold trajectory optimisation.

Operational constraints, such as cone angle limitations, may be imposed due to requirements for electrical power generation or thermal control, as discussed in subsection 2.1.3. For example, the NEA Scout mission had a cone angle constraint of  $\alpha_{\max} = 70^\circ$  (Heaton, Ahmad, & Miller, 2017). To analyse the impact of cone angle constraints on the size of the hold trajectory, seven maximum allowable cone angles are investigated:  $\alpha_{\max} = 60^\circ, 65^\circ, 70^\circ, 75^\circ, 80^\circ$  and  $85^\circ$ . Another constraint is the maximum angular turning rate of the sail, determined by the torque output of the attitude control system (Losada, 2024) and the sail's moment of inertia. For example, the ACS3 mission has a maximum turning rate constraint of  $\Omega_{\max} = 0.5^\circ/\text{s}$ . To investigate its impact on the size of the hold trajectory, five maximum allowable turning rates are analysed:  $\Omega_{\max} = 0.1^\circ/\text{s}, 0.25^\circ/\text{s}, 0.5^\circ/\text{s}, 1^\circ/\text{s}$  and  $2^\circ/\text{s}$ . However, if no constraints on the cone angle are imposed, the sail could simply orient edge-on to the Sun, which would not allow for a meaningful assessment of the turning rate's impact. Thus, a cone angle constraint of  $\alpha_{\max} = 70^\circ$  is imposed on the sail for the analysis of the maximum angular turning rate.

The analysis conducted in Section 3.3 revealed that for a constant sail attitude with a positive or negative clock angle, the sail would eventually drift in the positive or negative V-bar direction, potentially providing significant safety benefits when utilised in hold trajectories. To investigate the impacts of clock angle constraints on the hold trajectory, two scenarios are assessed: one where the clock angle is constrained to  $\delta \in (1^\circ; 179^\circ)$  and another where  $\delta \in (-179^\circ; -1^\circ)$ . Clock angles of  $0^\circ$  and  $\pm 180^\circ$  are

intentionally excluded, as previous analysis showed that the relative motion of the sail is dependent on the initial position in the GEI frame when maintaining a constant sail attitude. Again, to properly assess the impact, constraints on the cone angle are imposed as well. Lastly, an analysis is conducted in which all constraints are combined. For this, a maximum allowable cone angle of  $\alpha_{\max} = 70^\circ$  is chosen, along with purely positive or negative clock angles. Furthermore, the same turning rate constraints as previously are imposed. This comprehensive analysis allows for assessing the combined effects of operational constraints on the hold trajectory's size and feasibility.

The optimisation of the hold trajectories is conducted using InTrance. The setup of the simulation, including the propagation method and environmental factors, has already been discussed in Section 2.4. The specific settings and parameters used by InTrance for the optimisation for hold trajectories are provided in Appendix B. The input to the NC is based on the parameter tuning results from Figure A.5. For the hold trajectory optimisation, the NC receives the sails inertial Cartesian state, co-moving state, and the Sun-sail vector in the co-moving frame as input variables. Due to computational time constraints, each experimental scenario is only run once using a single random seed (Seed = 1) to initialise the optimiser. While this limits the exploration of potential variations, it still allows for an analysis of the primary characteristics and feasibility of the proposed hold trajectories within a reasonable time frame. To manage computational time, the simulation is run for ten target revolutions, which corresponds to 9.12 hours, with a step size of  $h = 10$  s.

## 4.2. Encircling Hold Trajectories

This section analyses the encircling hold trajectories and investigates the impact of the sail's operational constraints, specifically cone angle limitations and turning rate restrictions, on these trajectories. Initially, a nominal test case is presented to establish a baseline understanding of the sail's performance without any operational constraints. Following this, a parametric analysis is conducted by varying the maximum allowable values for these constraints and adjusting the sizes of the hold volume. The constraints are assessed individually to determine their specific influence on the trajectory.

Seven sizes of hold volumes are used for the analysis. The dimensions of the outer and inner ellipsoids defining each holding area, along with the initial conditions of the sail, are provided in Table 2. The semi-major and minor axes of the inner ellipsoid are set to 97% of those of the outer ellipsoid. This ratio was empirically chosen to allow for easy comparison of hold trajectories under different operational constraints. The initial Keplerian elliptical orbit, which lies within the hold volume, is positioned midway between the two ellipsoids. Clock angle constraints are not assessed in this section because their added safety benefits do not apply to encircling hold trajectories. As discussed in Section 3.4, even if the sail maintains a constant attitude, it would still pass close to the target, potentially causing a collision.

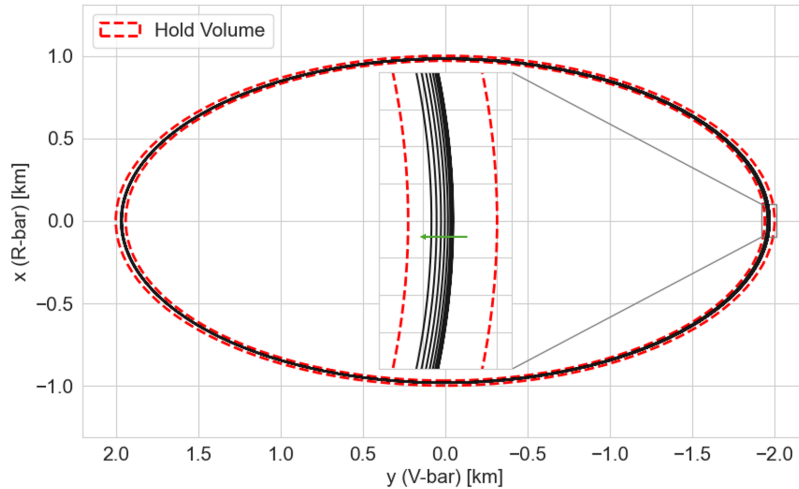
### 4.2.1. Test Case

For the test case of the encircling hold trajectory, no constraints are imposed on the sail's attitude or turning rate. The size of the safety ellipsoid for this test case is based on the safety zone used during rendezvous operations with the International Space Station. Specifically, the hold volume has a semi-major axis of 2 km along the target's orbital direction and a semi-minor axis of 1 km, corresponding to Case 5 in Table 2, which also lists the initial conditions for the hold trajectory optimisation.

Case	Outer Ellipsoid		Inner Ellipsoid		sail		
	Semi-Major	Semi-Minor	Semi-Major	Semi-Minor	$x_0$	$v_{y0}$	e
1	4000	2000	3880	1940	-1968.794	3.929	0.0002671
2	3500	1750	3395	1697.5	-1722.787	3.438	0.000233725
3	3000	1500	2910	1455	-1476.780	2.947	0.00020035
4	2500	1250	2425	1212.5	-1230.773	2.456	0.000166975
5	2000	1000	1940	970	-984.766	1.965	0.0001336
6	1500	750	1455	727.5	-738.574	1.474	0.0001002
7	1000	500	970	485	-495.331	0.988	0.0000672

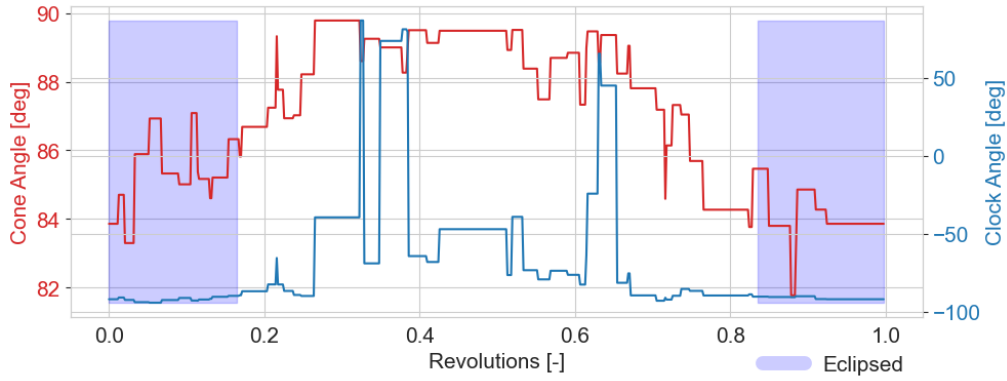
**Table 2:** Cases for the Analysis of Encircling Hold Trajectory

Figure 32 shows the optimised trajectory of the test case in the co-moving frame. While the sail remains within the hold volume throughout the simulation duration of ten revolutions, a drift in the positive  $V$ -bar direction can be seen. Additionally, it is observed that the optimised control profile repeats each orbital revolution (see Figure C3); therefore, only the control profile for the first revolution is presented in Figure 33. It is important to note that the sail's attitude, while it is eclipsed, does not influence the trajectory, as no SRP acceleration acts on it. When the sail is illuminated, the cone angle ranges between  $\alpha = 84^\circ$  and  $90^\circ$ , meaning the sail is oriented nearly edge-on to the Sun for the majority of the flight, resulting in a low acceleration magnitude. The clock angle exhibits multiple large instantaneous jumps from a negative to a positive clock angle and back. The clock angle ranges from  $\delta = -90^\circ$  to  $-50^\circ$  and from  $50^\circ$  to  $90^\circ$ , corresponding to a predominantly in-plane acceleration component.



**Figure 32:** Optimised trajectory of test case for encircling hold trajectory in the co-moving frame.

The trajectory in the GEI frame, including the SRP acceleration vector, is shown in Figure 34. During the first quarter of the revolution (orange arc), once the sail exits Earth's shadow, the SRP acceleration has a component opposite to the sail's velocity direction, leading to a decrease in orbital energy and, consequently, a reduction in the semi-major axis, as previously discussed in Chapter 3. However, due to the large cone angle, the overall acceleration is quite small, and the magnitude of the acceleration component opposing the velocity is reduced. In the second quarter of the revolution (blue arc), the cone angle increases to nearly  $\alpha = 90^\circ$ , positioning the sail almost edge-on to the Sun and thus minimising the SRP acceleration. Additionally, due to the repeated jumps in the clock angle during



**Figure 33:** Optimised control profile of test case for encircling hold trajectory over one orbital revolution.

this segment, the sail’s orientation changes by nearly  $180^\circ$  instantaneously, causing the acceleration component to alternate between opposing and aligning with the sail’s velocity direction. However, because the acceleration magnitude is minimal, these attitude changes do not significantly influence the trajectory.

After half a revolution, the cone angle decreases slightly, increasing the acceleration magnitude during the third quarter of the revolution (black arc). At the beginning of this phase, the acceleration vector aligns with the sail’s velocity vector, increasing the semi-major axis. The cone angle reaches its minimum of  $\alpha = 84^\circ$  just before the sail re-enters Earth’s shadow (green arc). As the acceleration is at its maximum (albeit still low due to the large cone angle), the semi-major axis decreases faster. While the sail’s acceleration is small throughout the revolution, the semi-major axis experiences a net decrease due to the control profile repeating each revolution, resulting in a continuous reduction of the semi-major axis over time.

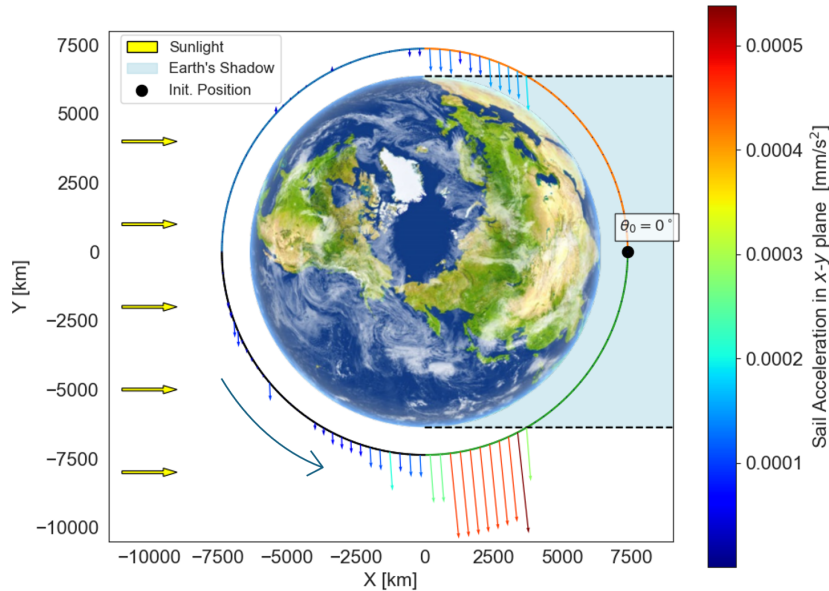


**Figure 34:** Optimised trajectory of test case for encircling hold trajectory in the GEI frame with parts of the trajectory highlighted for discussion.

The change in the semi-major axis of the trajectory over ten revolutions is shown in Figure 35. Periodic

behaviour is observed, with the semi-major axis increasing and decreasing twice per revolution. This variation does not correspond to the SRP acceleration acting on the sail but can be attributed to the use of the CW equations for the propagation. Since the CW equations are an approximation of the two-body dynamics, they introduce inaccuracies during propagation (see Section A.6), which can be seen as changes in the semi-major axis. Therefore, the small changes in the semi-major axis due to SRP acceleration are not readily apparent; nevertheless, the continuous decrease of the semi-major axis can still be observed. As discussed in Chapter 3, a decreasing semi-major axis results in the spacecraft drifting in the positive  $V$ -bar direction. Although the semi-major axis decreases by only approximately 50 cm over the ten revolutions, this is sufficient to induce a noticeable drift in the co-moving frame (see Figure 32), confirming the results obtained in the previous chapter.

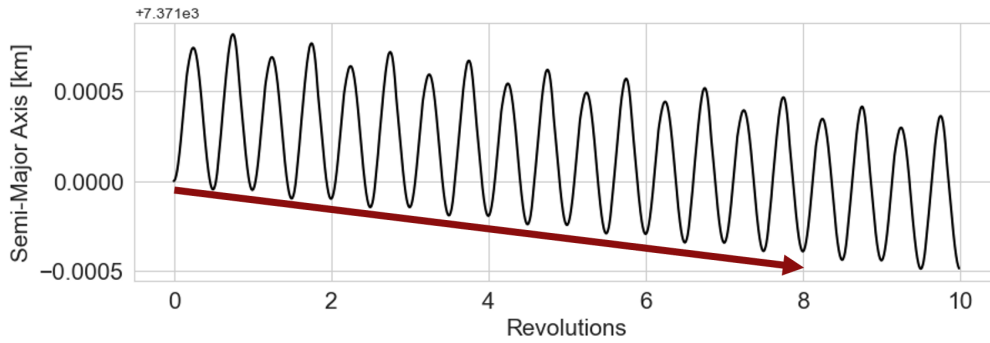


**Figure 35:** Change of semi-major of the optimised trajectory of test case for encircling hold trajectory.

While the sail remains within the hold volume with this control profile for the simulation duration of ten revolutions, if propagated for a longer time, the sail would eventually drift out of the hold volume into the safety zone. This occurs because the right orbit crossing drifts continuously closer to the target, potentially leading to a close approach or even a collision.

#### 4.2.2. Cone Angle Constraints

To assess the impact of cone angle constraints on encircling hold trajectories, six different cone angle restrictions are analysed, as shown in Table 1. The turning rate and the clock angle are left unconstrained. The results of the optimisation for each hold volume, as defined in Table 2 and each cone angle constraint, are presented in Table 3. The table shows the number of revolutions the sail spends inside the hold volume. Given a simulation duration of ten revolutions, the maximum time the sail can remain within the hold volume is ten revolutions. It can be seen that for cone angle restrictions of  $\alpha_{\max} = 70^\circ$  and above, the sail is able to spend the entire ten revolutions inside the hold volume. For cone angle restrictions  $\alpha_{\max} = 60^\circ$  and  $65^\circ$ , it can be seen that for smaller hold volumes, the sail spends less time in the hold volume.

For Case 7, which corresponds to the smallest hold volume, the optimised control profiles and the differences in semi-major axis relative to the target orbit are presented in Figure 36 for maximum cone angles of  $\alpha_{\max} = 60^\circ$ ,  $75^\circ$  and  $85^\circ$ . It is noted that all optimised control profiles repeat each orbital revolution; this is true for all upcoming optimised hold trajectories and will not be restated. Therefore, the control profiles are only shown for the first revolution while the sail is illuminated by the Sun.

For a maximum allowable cone angle of  $\alpha_{\max} = 85^\circ$ , the cone angle remains mostly constant at its

Case	$\alpha_{\max}$ [°]					
	60	65	70	75	80	85
1	8.79	10	10	10	10	10
2	7.75	10	10	10	10	10
3	7.60	10	10	10	10	10
4	6.99	9.46	10	10	10	10
5	4.87	8.43	10	10	10	10
6	3.99	7.12	10	10	10	10
7	2.64	5.95	10	10	10	10

**Table 3:** Number of revolutions sail spends inside hold volume with cone angle constraint.

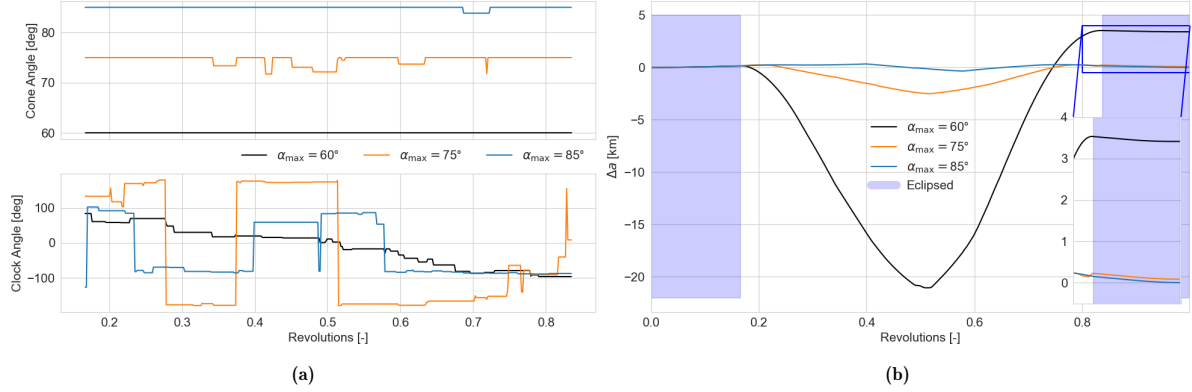


**Figure 36:** a) Optimised control profile and b) differences in semi-major axis relative to initial values for maximum cone angles of  $\alpha_{\max} = 60^\circ$ ,  $70^\circ$  and  $85^\circ$  for Case 7, as shown in Table 4

maximum allowable value, minimising the sail's acceleration. The clock angle exhibits instantaneous jumps from  $\delta = 90^\circ$  to  $\delta = -90^\circ$  and back, effectively turning the sail by  $180^\circ$ . While this increases the in-plane acceleration component, the overall acceleration magnitude is small because of the large cone angle. Consequently, the change in the semi-major axis is small, allowing the sail to remain within the hold volume for the entire simulation duration. However, the same inaccuracies due to the use of the CW equation, as discussed in subsection 4.2.1, are observed in the change of the semi-major axis. These inaccuracies are also apparent for  $\alpha_{\max} = 60^\circ$  and  $75^\circ$ . While the changes in the semi-major axis for these cases are larger, a variation in the semi-major axis is still observed during eclipse periods when the sail is not subject to SRP acceleration (see Figure 36 b)). For a maximum cone angle of  $\alpha_{\max} = 75^\circ$ , the cone angle also remains largely at its maximum value. To minimise the in-plane acceleration component, the clock angle is approximately at  $\delta = \pm 180^\circ$ . Only towards the end of the revolution do larger jumps in the attitude occur as the clock angle shifts increases from  $\delta = -180^\circ$  to  $\delta = 180^\circ$ . This control profile decreases the semi-major axis by approximately 2.5 m and then raises it back to its initial value by the end of the revolution, thus still inducing drift.

For a maximum allowable cone angle of  $\alpha_{\max} = 60^\circ$ , the sail is not able to spend the entire simulation time within the hold volume. While the cone angle remains constant at its maximum allowable value throughout the flight (see Figure 36 a)) to minimise the overall sail acceleration, it is observed that the in-plane acceleration is not minimised throughout the flight. However, to reduce the change in the semi-major axis, the clock angle starts from approximately  $\delta = 90^\circ$  at the beginning of the revolution and decreases to  $\delta = -90^\circ$ . As shown in Figure 37 a), this strategy largely reduces the acceleration component in the sail's velocity direction and directs it primarily in the radial direction, aiming to

minimise changes in the semi-major axis. However, the change in the semi-major axis is still larger than in the other two discussed cases (see Figure 36 b)). Moreover, during the first revolution, the semi-major axis is initially reduced but increases to a value higher than the target semi-major axis by the end of the revolution. Thus, over multiple revolutions, the semi-major axis continuously increases. This results in an initial drift in the positive V-bar direction due to the lower semi-major axis, followed by a drift in the negative V-bar direction as the semi-major axis increases, as illustrated in Figure 37 b).

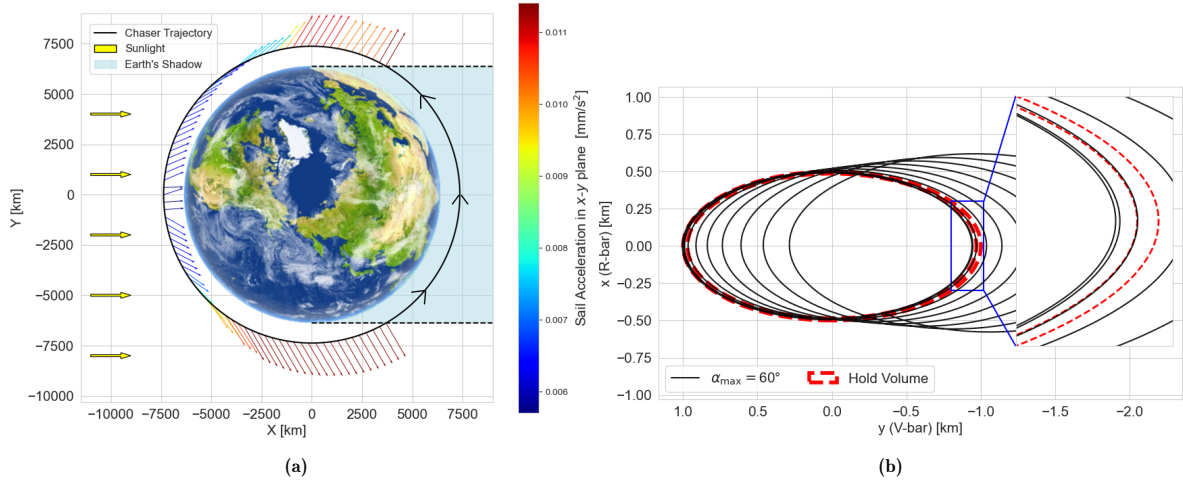


**Figure 37:** Optimised trajectory in a) inertial and b) co-moving frame for maximum cone angles of  $\alpha_{\max} = 60^\circ$  for Case 7, as shown in Table 4

In general, it can be observed that the sail acceleration is minimised by maintaining a cone angle close to the maximum allowable cone angle in all cases. Because of this, the clock angle does not play a vital role for large maximum allowable cone angles. Due to the already minimised acceleration, the change in the semi-major axis is also small, leading to a reduced drift, as seen in the co-moving frame, allowing the sail to remain within the hold volume for an extended period of time. As the maximum allowable cone angle decreases, the sail must adjust the clock angle to reduce the in-plane acceleration component. This is typically achieved by setting the clock angle to approximately  $\delta = 0^\circ$  or  $\delta = \pm 180^\circ$ , directing the acceleration out-of-plane. However, with smaller allowable cone angles, the change in the semi-major axis becomes more significant because the sail cannot effectively minimise the in-plane acceleration component. If the maximum allowable cone angle becomes too small, the sail cannot sufficiently reduce the in-plane acceleration through clock angle adjustments alone, resulting in larger differences in the semi-major axis. This leads to the spacecraft drifting out of the hold volume in a shorter amount of time. Larger hold volumes provide the sail with more space to manoeuvre and thus increase the time the spacecraft is able to spend inside the hold volume. Lastly, despite efforts to maintain the hold trajectory within the holding area, all trajectories eventually show a drift in the negative or positive V-bar direction, indicating the necessity for periodic correction manoeuvres to sustain the desired position relative to the target.

### 4.2.3. Turning Rate Constraints

To assess the impact of turning rate constraints on hold trajectories without a safety zone, six different turning rate restrictions are analysed, as shown in Table 1. Since a cone angle of  $\alpha = 90^\circ$  results in zero acceleration on the sail, no turning is required to maintain the sail within the hold volume; the sail

would simply follow its initial keplerian elliptical orbit. Therefore, to evaluate the impact of turning rate restrictions, the maximum allowable cone angle for this analysis is set to  $\alpha_{\max} = 75^\circ$ . Furthermore, for this maximum allowable cone angle, fast attitude changes at the end of the revolution were observed in the previous analysis (see Figure 36 a)).

For these constraint conditions, in all cases, the sail is able to remain within the hold volume for the entirety of the simulation period. As in the previous analysis, the cone angle remains constant at its maximum allowable value. However, whereas for the unconstrained turning rate, fast cone angle changes were observed, in the constraint case, the cone angle remains either at  $\delta = \pm 180^\circ$  or at  $\delta = 0^\circ$  throughout the flight, minimising the in-plane acceleration.

### 4.3. Leading/Trailing Hold Trajectories

In this section, the impact of cone and clock angle limitations and turning rate restrictions on hold trajectories located ahead of or behind the target is investigated. Since the sail no longer flies around the target, an inner safety zone is not required. Instead, a smaller hold volume becomes advantageous, as it keeps the sail closer to the target throughout its trajectory, allowing for better observation. First, a test case is examined to establish a baseline understanding of the sail's behaviour without any operational constraints during leading/trailing hold trajectories. Following this, a parametric study is conducted by varying the maximum allowable values for these constraints and adjusting the sizes of the hold volume. Each attitude constraint is assessed individually to determine its specific influence on the trajectory. For the analysis, eight hold volumes are examined. The dimensions of the ellipsoid defining each hold volume, along with the initial conditions for the sail, are provided in Table 4. The initial Keplerian elliptical orbit of the sail is positioned 2% inside the hold volume's ellipsoid. If it were positioned closer to the ellipsoid, inaccuracies due to the use of the Clohessy-Wiltshire (CW) equations would lead the chaser to drift out of the hold volume, even without additional accelerations acting on it. Furthermore, by placing the initial orbit relatively close to the ellipsoid, the impact of the constraints on the size of the hold trajectory can be assessed more easily.

Case	Outer Ellipsoid		Sail		
	Semi-Major Axis [m]	Semi-Minor Axis [m]	$x_{M,0}$ [m]	$dy_{M,0}$ [m/s]	e [-]
1	1000	500	-493.857	0.985	0.000067
2	750	375	-372.236	0.743	0.0000505
3	500	250	-246.929	0.493	0.0000335
4	250	125	-121.622	0.243	0.0000165
5	200	100	-95.823	0.191	0.000013
6	150	75	-69.287	0.138	0.0000094
7	100	50	-44.226	0.088	0.000006
8	50	25	-22.113	0.044	0.000003

**Table 4:** Test cases for encircling hold trajectory analysis

Although the hold volume is located ahead of or behind the target, the motion of the sail in both cases is the same, as the hold volume can be shifted along the orbit. Thus, only one analysis needs to be conducted for both hold volume positions. For this analysis, the hold volume is kept centred around the origin in the co-moving frame, effectively positioning the target object along the V-bar axis ahead of or behind the sail. This approach was chosen because, when using the CW equations, the accuracy

decreases with increased distance from the origin. Therefore, instead of shifting the hold volume in the negative or positive V-bar direction, the artificial target is moved along the V-bar axis. This keeps the hold volume on the target orbit without unnecessarily increasing the inaccuracy of the solution.

This section first presents the test case to illustrate the sail's behaviour without constraints. Then, it examines the impact of cone angle constraints, followed by an assessment of turning rate constraints. The solar-sail relative motion analysis in Chapter 3 revealed that using a purely positive or negative clock angle profile causes the sail to eventually drift in the positive or negative V-bar direction, respectively. An analysis is conducted to potentially exploit this phenomenon for increased safety during the hold trajectory by constraining the clock angle during the hold phase. Finally, the combined impact of these restrictions is investigated by simultaneously imposing angle and turning rate constraints, along with a negative clock angle constraint.

### 4.3.1. Test Case

For the test case of the leading/trailing hold trajectory, no constraints are imposed on the sail's attitude or turning rate. The hold volume has a semi-major axis of 500 m and a semi-minor axis of 250 m, corresponding to Case 3 in Table 2.

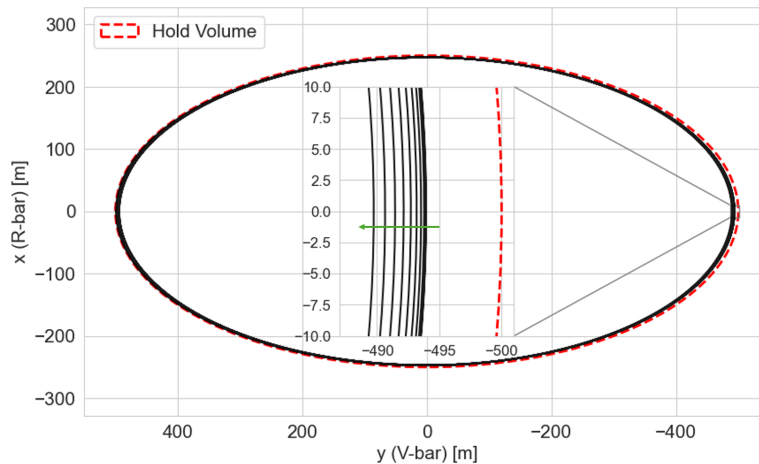


**Figure 38:** Optimised trajectory of test case for leading/trailing hold trajectories in the co-moving frame.

Figure 38 shows the optimised trajectory of the test case in the co-moving frame. The sail is able to stay within the hold volume for the entire simulation period, with only a minor drift observed in the positive V-bar direction. The optimised control profile is shown in Figure 39. The cone angle ranges between  $\alpha = 88^\circ$  and  $90^\circ$ , indicating that the sail is oriented nearly edge-wise to the Sun. This orientation minimises the acceleration on the sail to a nearly negligible level. Despite this, a minor drift is still observed in the co-moving frame. The cone angle exhibits erratic behaviour with large instantaneous jumps in attitude. However, due to the very small acceleration, this only leads to a very slow decrease of the semi-major axis, as shown in Figure C2, resulting in the previously mentioned drift. As discussed in subsection 4.2.1 for the test case of the encircling hold trajectory, the change in the semi-major axis is so small that inaccuracies dominate, and the decrease of the semi-major axis is only visible over multiple revolutions. It is noted that the change in the semi-major axis due to inaccuracies is smaller than in the previous test case (see Figure 35). This is because the size of the hold trajectory is smaller, and the sail's movement is closer to the origin of the co-moving frame, which increases the accuracy of

the CW equations, as discussed in subsection 2.2.4.

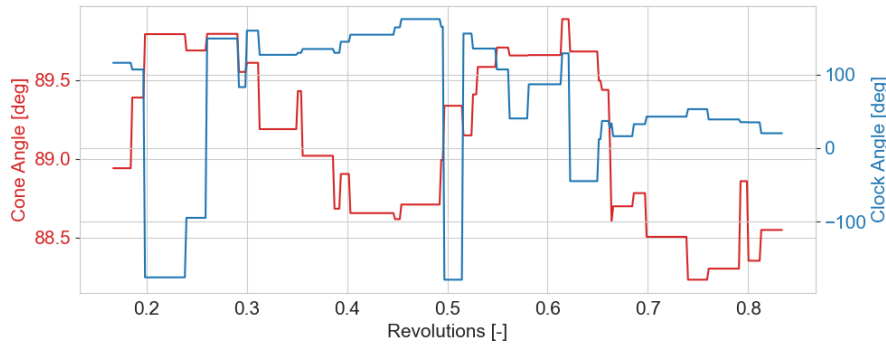


**Figure 39:** Optimised control profile of test case for leading/trailing hold trajectories over one orbital revolution.

### 4.3.2. Cone Angle Constraints

To assess the impact of cone angle constraints on hold trajectories without a safety zone, six different cone angle restrictions are analysed:  $\alpha_{\max} = 60^\circ, 65^\circ, 70^\circ, 75^\circ, 80^\circ$  and  $85^\circ$ . The results of the hold trajectory optimisation for each test case, as defined in Table 4, and each cone angle constraint are presented in Table 5. This table shows the number of revolutions the sail spends inside the hold volume. Given a simulation duration of ten revolutions, the maximum time the sail can remain within the target zone is ten revolutions.

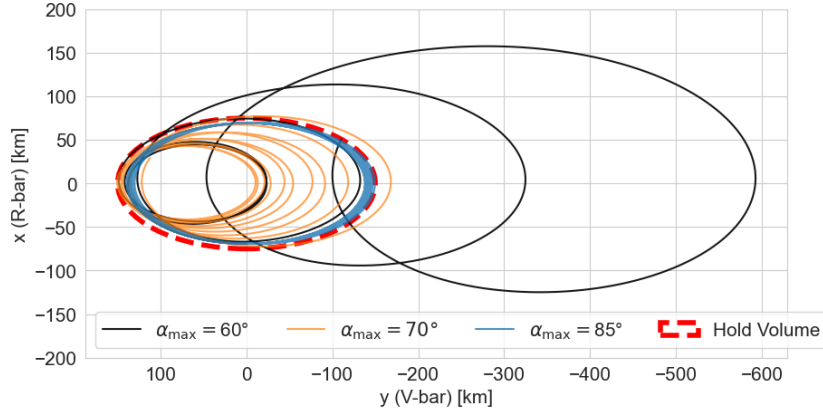
Case	$\alpha_{\max} [^\circ]$					
	60	65	70	75	80	85
1	10	10	10	10	10	10
2	9.49	10	10	10	10	10
3	8.06	10	10	10	10	10
4	4.97	8.15	10	10	10	10
5	3.94	7.14	10	10	10	10
6	3.35	5.71	9.50	10	10	10
7	2.39	3.63	7.21	10	10	10
8	1.19	2.07	3.49	8.13	10	10

**Table 5:** Number of revolutions sail spends inside hold volume with cone angle constraint.

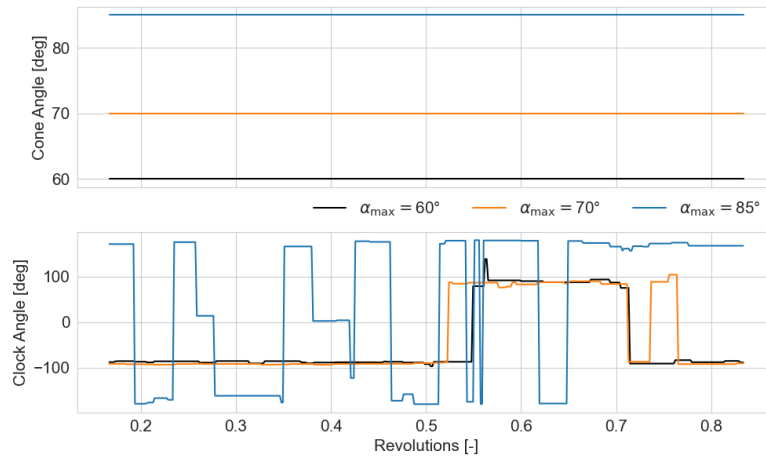
Table 5 shows that for maximum cone angles of  $\alpha_{\max} = 80^\circ$  and  $85^\circ$ , the sail consistently spends the maximum allowable time inside the hold volume across all test cases. Conversely, as the cone angle becomes more restricted and the hold volume decreases, the time the sail remains within the hold volume also diminishes. Specifically, with a maximum allowable cone angle of  $\alpha_{\max} = 60^\circ$ , only the largest hold volume (Case 1) enables the sail to maintain the maximum time within it. This trend can be explained by the fact that smaller hold volumes correspond to orbits with smaller eccentricities, approaching a Keplerian circular orbit as the hold volume diminishes. A Keplerian orbit can only be maintained with a cone angle of  $\alpha = 90^\circ$ , where no solar SRP acceleration acts on the sail. Therefore, when the hold volume is small, the sail cannot remain within it for an extensive period of time unless the cone angle allows for minimal or no SRP acceleration.

Figure 40 shows the optimised hold trajectories for Case 6 with maximum allowable cone angles of  $\alpha_{\max} = 60^\circ, 70^\circ$  and  $85^\circ$ . Their respective control profiles are presented in Figure 41. For a maximum

allowable cone angle of  $\alpha_{\max} = 85^\circ$ , the sail remains within the hold volume for the entire simulation period, exhibiting only a minor drift. This is because the sail operates at its maximum allowable cone angle throughout the flight, while the clock angle is maintained at  $\delta = \pm 180^\circ$ , minimising both the overall acceleration and the in-plane acceleration components.



**Figure 40:** Optimised hold trajectories for maximum cone angles of  $\alpha_{\max} = 60^\circ$ ,  $70^\circ$  and  $85^\circ$  for Case 6, as shown in Table 4



**Figure 41:** Sail control angles for optimised hold trajectories for maximum cone angles of  $\alpha_{\max} = 60^\circ$ ,  $70^\circ$  and  $85^\circ$  for Case 6, as shown in Table 4

In the case of  $\alpha_{\max} = 70^\circ$ , the sail also keeps the cone angle at its maximum allowable value to minimise the overall acceleration. However, the clock angle alternates between  $\delta = \pm 90^\circ$ , which maximises the in-plane acceleration component and requires the sail to turn by  $180^\circ$  instantaneously. This leads to a reduction in the eccentricity, as shown in Figure 42. Additionally, over one revolution, the sail's semi-major axis first decreases (see Figure 43), causing the sail's right orbit crossing to shift in the positive V-bar direction. Both effects result in an inward spiralling of the sail as seen in the co-moving frame, allowing the sail to maximise the time spent inside the hold volume. However, by the end of the revolution, the semi-major axis increases to a value higher than that of the target, leading to a gradual increase in the semi-major axis over the simulation period. Consequently, the sail eventually drifts into the negative V-bar direction while the eccentricity increases.

A similar control profile is observed for a maximum allowable cone angle of  $\alpha_{\max} = 60^\circ$ . Although the

sail decreases the overall acceleration by maintaining the cone angle at its maximum value, the in-plane acceleration component is increased due to the clock angle adjustments. Due to the smaller allowable cone angle, the change in the semi-major axis is more pronounced, causing the sail to drift in negative  $V$ -bar direction more quickly. This also leads to a faster increase in the eccentricity.

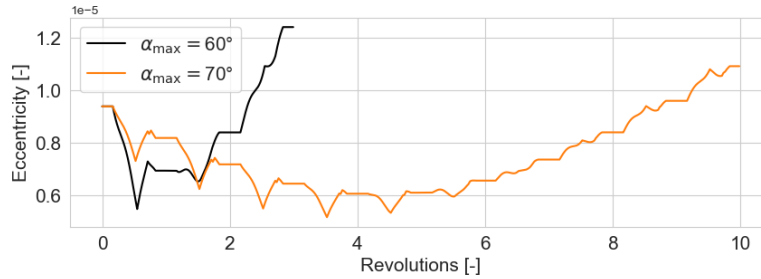


**Figure 42:** Eccentricity for optimised hold trajectories for maximum cone angles of  $\alpha_{\max} = 60^\circ$  and  $70^\circ$  for Case 6, as shown in Table 4

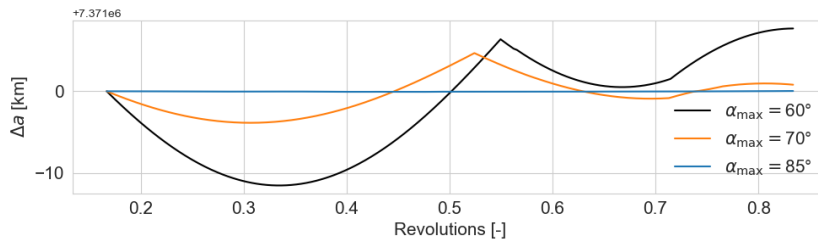


**Figure 43:** Difference in semi-major axis compared to target orbit for optimised hold trajectories for maximum cone angles of  $\alpha_{\max} = 60^\circ$  and  $70^\circ$  for Case 6, as shown in Table 4

The analysis demonstrates that larger maximum allowable cone angles, such as  $\alpha_{\max} = 80^\circ$  and  $85^\circ$ , enable the sail to spend more time within the hold volume, even for smaller target sizes. This is because, for larger cone angles, the SRP acceleration decreases, allowing for a more adaptable steering strategy that can maintain the sail within a smaller hold volume. Conversely, more restrictive cone angles, such as  $\alpha_{\max} = 60^\circ$ , result in larger minimum accelerations that may cause the sail to exit smaller hold volumes more quickly. Furthermore, the trajectories which remain within the hold volume for longer periods often feature clock angles around  $\delta = \pm 180^\circ$  or  $0^\circ$ , minimising in-plane acceleration. On the other hand, trajectories which are not able to stay within the hold volume for a longer period of time show clock angles alternating between  $\delta = -90^\circ$  and  $90^\circ$ , which leads to an initial reduction of the eccentricity, letting the sail spiral inwards before the change of the semi-major axis leads to a drift away from the hold volume.

### 4.3.3. Turning Rate Constraints

In this section, the impact of the solar sail's turning rate constraints on leading/trailing hold trajectories is analysed. The constrained conditions have been discussed in Section 4.1 and were shown in Table 1. The results of this analysis are shown in Table 6, which lists the number of revolutions the sail spends inside the hold volume for each case, including the scenario with no turning rate limitations ( $\Omega_{\max} = \infty$ ), representing the results shown in Table 5 for  $\alpha_{\max} = 70^\circ$ , for comparison.

Table 6 shows that, for all turning rate restrictions, the sail spends the maximum time inside the hold volume for test Cases 1, 2, and 3. As the hold volume size decreases and the turning rate becomes

Case	$\Omega_{\max}$ [ $^{\circ}/s$ ]					
	0.1	0.25	0.5	1	2	$\infty$
1	10	10	10	10	10	10
2	10	10	10	10	10	10
3	10	10	10	10	10	10
4	9.56	10	10	10	10	10
5	9.24	10	10	10	10	10
6	7.84	8.92	9.37	9.48	9.50	9.50
7	5.54	6.96	7.10	7.11	7.16	7.21
8	3.07	3.51	3.65	3.57	3.83	3.49

**Table 6:** Number of revolutions sail spends inside hold volume with turning rate constraint for a maximum allowable cone angle of  $\alpha_{\max} = 70^{\circ}$ .

more restricted, the time the sail spends inside the hold volume also decreases. For example, in case 6, without a turning rate restriction, the sail remains inside the hold volume for 7.21 revolutions. When the turning rate is limited to  $\Omega_{\max} = 0.1^{\circ}/s$ , this time decreases to 5.54 revolutions. In case 8, the sail spends more time inside the hold volume for all turning rate restrictions except  $\Omega_{\max} = 0.1^{\circ}/s$ , compared to the unrestricted scenario, which would speak against the previous statement. However, this variation is likely due to local minima in the optimisation process. By using a different seed (Seed=3) for the unconstrained case, a higher revolution count is achieved compared to the constrained cases.

For Cases where the sail is able to stay within the hold volume for the entire simulation period, control profiles are observed similar to the one described in Figure 41 for a maximum allowable cone angle of  $\alpha_{\max} = 85^{\circ}$  in the previous section. The cone angle is constant at its maximum allowable value, while the clock angle largely remains around  $\delta = \pm 180^{\circ}$ , which already minimises the amount the sail needs to rotate, while still able to minimise the overall SRP acceleration.

Figure 44 shows the optimised hold trajectory (a) and their corresponding sail control angles (b) for Case 7 and a maximum turning rate of  $\Omega_{\max} = 0.1^{\circ}$  and  $0.5^{\circ}$ , as well as the unrestricted case. In these cases, the sail is unable to stay within the hold volume over ten revolutions. For the cone angle, small changes up to  $\alpha = 2^{\circ}$  and  $\alpha = 1^{\circ}$  can be observed for a maximum turning rate of  $\Omega_{\max} = 0.1^{\circ}$  and  $0.5^{\circ}$  respectively. Nevertheless, it can be said that for these cases, the sail operates at its maximum allowable cone angle to reduce overall acceleration. Furthermore, as already explained in subsection 4.3.2, the cone angle exhibits instantaneous jumps from  $\delta = -90^{\circ}$  to  $\delta = 90^{\circ}$  and back for the unrestricted case, which leads to an initial decrease of the eccentricity and thus an inward spiralling as seen in the co-moving frame. When restrictions on the turning rate are imposed, the sail must gradually change its cone angle to reach the desired attitude. For a more restricted turning rate, it can be seen that the manoeuvre begins earlier, resulting in a more gradual change in the clock angle. This, however, leads to a faster drift out of the hold volume due to a smaller initial decrease in the eccentricity.

#### 4.3.4. Clock Angle Constraints

The safety analysis presented in Chapter 3 showed that maintaining a constant sail attitude with a positive clock angle causes the sail to drift in the positive V-bar direction. Conversely, a constant attitude with a negative clock angle results in drift in the opposite direction. This behaviour can be utilised by positioning the hold volume ahead of or behind the target. By adopting a consistently

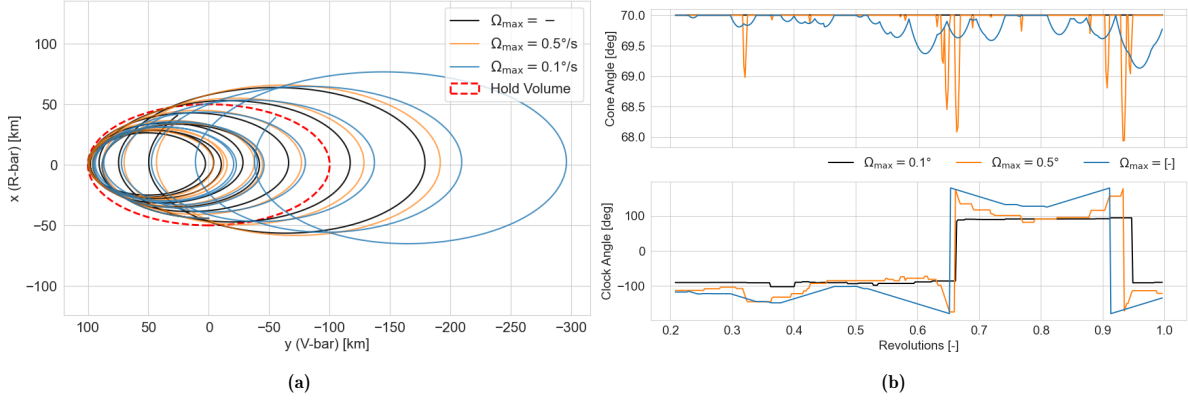


**Figure 44:** (a): Optimised hold trajectory and (b): corresponding sail control angles for turning rate restrictions of  $\Omega_{\max} = 0.1^\circ/\text{s}$  and  $0.5^\circ/\text{s}$  and the unrestricted turning rate for case 7, as shown in Table 4

positive or negative clock angle profile, it is possible to ensure that, in the event of technical issues or an urgent need to increase the distance between the sail and the target, the sail can hold its current attitude and naturally drift away from the target at any point along its trajectory.

The following analysis examines leading/ trailing hold trajectories resulting from purely positive ( $\delta \in (1; 179)$ ) and negative ( $\delta \in (-179; -1)$ ) clock angle profiles. The specific constrain conditions are shown in Table 1.

### Positive Clock Angle

Table 7 shows the results of the hold trajectory optimisation for a purely positive clock angle profile ( $\delta \in (1; 179)$ ). It can be seen that as the cone angle constraint becomes tighter and the hold volume smaller, the time the sail spends inside the target area decreases. The table furthermore indicates that the sail can stay within the tested hold volume for all ten revolutions only when the maximum cone angles are  $80^\circ$  and  $85^\circ$ , leading to a small SRP acceleration. However, for a maximum cone angle of  $80^\circ$ , the sail does not remain within the target area for the full ten revolutions in Cases 2, 3, 4, and 5. This result is surprising, given that solutions were found for smaller target areas (Cases 6 and 7) where the sail stayed in the hold volume for the entire duration. The differences in outcomes can likely be explained by local optima in the search space. With a different set of seeds (Seed = 4), hold trajectories were found, which let the sail stay within the target area for all ten revolutions in these cases.

Case	$\alpha_{\max} [^\circ]$					
	60	65	70	75	80	85
1	4.44	5.37	6.44	8.41	10	10
2	4.06	4.61	5.66	6.90	8.87	10
3	3.54	4.19	5.32	6.89	9.12	10
4	2.63	3.31	4.20	6.08	9.09	10
5	2.32	3.03	3.96	6.21	9.62	10
6	2.06	2.67	3.65	6.14	10	10
7	1.65	2.19	3.08	5.53	10	10
8	1.12	1.49	2.11	3.26	7.43	10

**Table 7:** Number of revolutions sail stays inside target area with cone angle constraint for a clock angle  $\delta \in (1; 179)$ .

In general, two types of trajectories can be observed: one that gradually shifts in the positive V-

bar direction due to a decrease in the semi-major axis and another that shifts in the negative V-bar direction due to an increase in the semi-major axis. For example, in Case 1 with maximum cone angles of  $\alpha_{\max} = 60^\circ$ ,  $70^\circ$  and  $85^\circ$ , the trajectories and their corresponding control profiles are shown in Figure 45. For  $\alpha_{\max} = 85^\circ$ , the cone angle remains constant throughout the flight, minimising overall acceleration. Additionally, the clock angle is largely at its minimum value, further reducing the in-plane acceleration and resulting in only minor drift.

In contrast, for  $\alpha_{\max} = 70^\circ$ , a drift in the negative V-bar direction is observed. In this case, the cone angle is mostly constant at its maximum allowable value, while the clock angle is adjusted to reduce the in-plane acceleration. Initially, this leads to a decrease in the semi-major axis, as the acceleration opposes the sail's velocity vector (see Figure 46). However, during the second half of the revolution, the cone angle increases to  $\alpha = 10^\circ$  for a brief period, which requires the sail to turn instantaneously. This change increases the magnitude of the SRP acceleration in the direction of the sail's velocity vector, leading to a rapid increase in the semi-major axis. After one revolution, the semi-major axis is higher than the target's by approximately  $\Delta a = 4$  km. Consequently, over multiple revolutions, the semi-major axis continues to increase, causing the sail to drift in the negative V-bar direction.

A similar decrease in the cone angle is observed for  $\alpha_{\max} = 60^\circ$ , but the adjustment is smaller, only decreasing to  $\alpha = 50^\circ$ . Thus, the increase in the semi-major axis during this part of the trajectory is less pronounced. At the end of the revolution, although the semi-major axis is above that of the target, the difference is smaller compared to the  $\alpha_{\max} = 70^\circ$  case. Therefore, due to the overall lower semi-major axis relative to the target, the sail drifts in the positive V-bar direction. However, since the semi-major axis still increases each revolution, propagating this control profile over a longer period would eventually cause the sail to drift back in the negative V-bar direction.

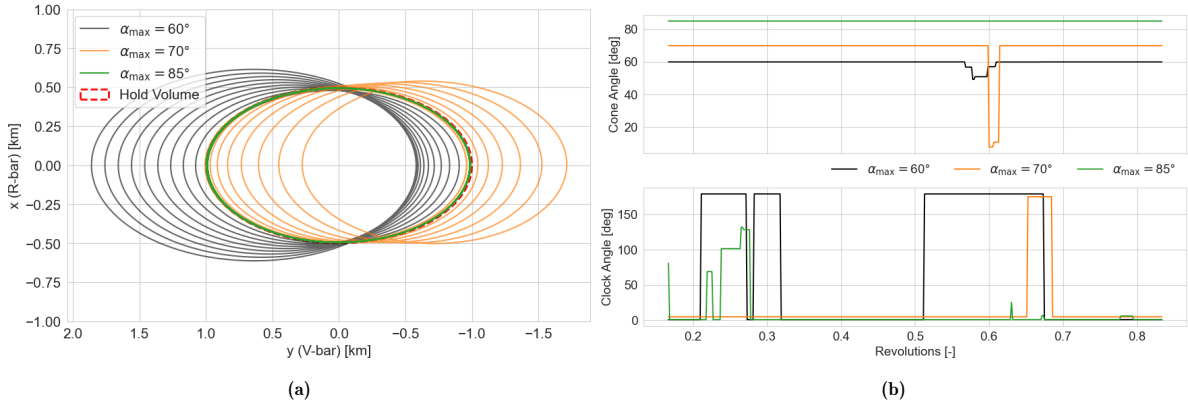


**Figure 45:** (a): Optimised hold trajectory and (b): corresponding sail control angles for positive clock angle restriction for maximum cone angles of  $\alpha_{\max} = 60^\circ$ ,  $70^\circ$  and  $85^\circ$  for case 1, as shown in Table 4

The analysis of a purely positive clock angle profile reveals that, compared to the unconstrained case, larger hold volumes are required for the same constraint on the cone angle. Only sails with large maximum allowable cone angles ( $\alpha_{\max} > 80^\circ$ ) were able to stay within the analysed hold trajectories. For smaller maximum allowable cone angles, the sail is not able to stay close to the target for a longer period of time. This makes leading hold trajectories with a positive clock angle restriction a less suitable alternative for prolonged stay for a control profile that repeats each revolution. Furthermore, it is shown that even if a constant sail attitude with a positive clock angle leads to a drift in a positive V-bar direction, a control profile can be established that increases the semi-major axis, eventually leading

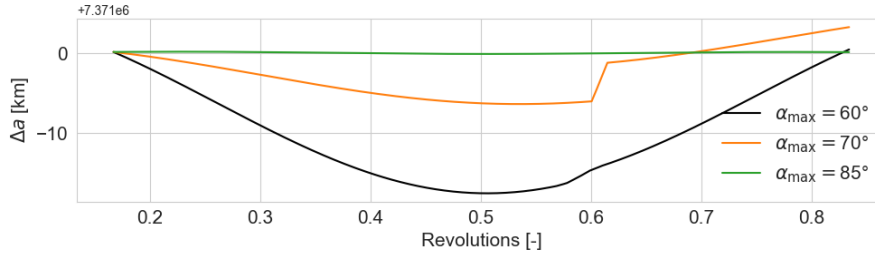


**Figure 46:** Difference in the semi-major axis compared to target orbit for maximum cone angles of  $\alpha_{\max} = 60^\circ$ ,  $70^\circ$  and  $85^\circ$  for Case 1, as shown in Table 4

to a drift in a negative V-bar direction.

### Negative Clock Angle

The results of the hold trajectory optimisation for a purely negative clock angle profile are presented in Table 8. As with the positive clock angle profile, it can be seen that smaller hold volumes and more restrictive cone angles reduce the time the sail can stay within the hold volume. However, unlike the positive clock angle profile, the negative profile allows smaller maximum cone angles to remain within smaller hold volumes for the maximum duration.

Case	$\alpha_{\max}$ [°]					
	60	65	70	75	80	85
1	9.86	10	10	10	10	10
2	8.80	10	10	10	10	10
3	7.15	10	10	10	10	10
4	4.43	7.12	10	10	10	10
5	3.63	6.07	9.39	10	10	10
6	2.63	4.73	7.92	10	10	10
7	1.6	3.39	5.99	10	10	10
8	1.15	1.56	2.84	6.37	10	10

**Table 8:** Number of Revolutions sail Spends Inside Target Area With Cone Angle Constraint for a clock angle  $\delta \in (-179; -1)$ .

The trajectories for Case 1 with maximum cone angles of  $\alpha_{\max} = 60^\circ$ ,  $70^\circ$  and  $85^\circ$ , along with their respective control profiles, are shown in Figure 47. With a maximum cone angle of  $\alpha_{\max} = 60^\circ$ , the sail begins to spiral inward due to a decrease in eccentricity, as previously explained in subsection 4.3.2. This inward spiralling is also observed in the other two trajectories but is less pronounced because the overall acceleration decreases with a larger allowable cone angle. Notably, this inward spiralling is not observed with a purely positive cone angle profile, yet when present, it allows for a prolonged stay within the hold volume. However, the semi-major axis increases gradually over multiple revolutions (see Figure C4), which would eventually lead to a drift in the negative V-bar direction. Furthermore, large instantaneous jumps in the sail attitude are still observed (see Figure 47 b)).

The analysis of a restricted, purely negative clock angle profile revealed that the time spent within the hold volume decreases as both the hold volume and maximum cone angle decrease. Nevertheless, unlike the positive clock angle profile, trajectories were found that remained within the hold volume for the entire simulation duration even with smaller maximum cone angles ( $\alpha_{\max} < 80^\circ$ ) and smaller hold volumes. This makes hold trajectories with a negative clock angle profile a more viable choice

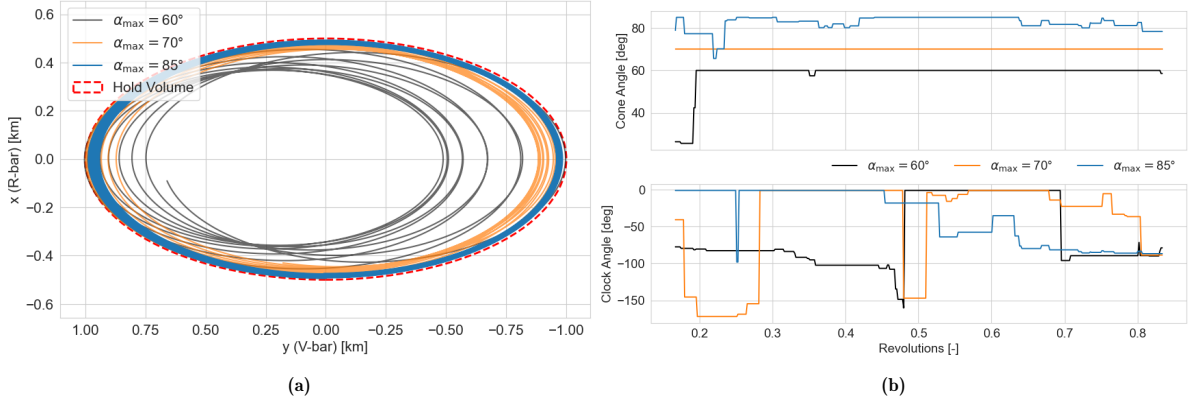


**Figure 47:** (a): Optimised hold trajectory and (b): corresponding sail control angles for negative clock angle restriction for maximum cone angles of  $\alpha_{\max} = 65^\circ$ ,  $75^\circ$  and  $85^\circ$  for case 1, as shown in Table 4.

than those with a purely positive clock angle profile, as the maximum distance between the sail and the target during the hold trajectory would be reduced, allowing for a closer observation of the target.

### 4.3.5. Combined Constraints

Previous analyses demonstrated that hold trajectories with purely negative clock angle profiles, when the hold volume is positioned behind the target, consistently drift away from the target, thereby satisfying safety constraints. However, these trajectories require large, instantaneous changes in the cone angle, raising concerns about their feasibility. To address this, restrictions on the sail turning rate are introduced. In the following analysis, a maximum cone angle of  $\alpha_{\max} = 70^\circ$  and a clock angle constraint of  $\delta \in (-179; -1)$  is imposed. Six sail turning rates are assessed:  $\Omega_{\max} = 0.1^\circ/\text{s}$ ,  $0.25^\circ/\text{s}$ ,  $0.5^\circ/\text{s}$ ,  $1^\circ/\text{s}$  and  $2^\circ/\text{s}$ , as already shown in Table 1.

Case	$\Omega_{\max} [^\circ/\text{s}]$					
	0.1	0.25	0.5	1	2	inf
1	10	10	10	10	10	10
2	10	10	10	10	10	10
3	10	10	10	10	10	10
4	7.81	8.07	8.11	8.15	7.82	10
5	6.52	6.64	6.65	6.71	6.85	9.39
6	5.05	5.06	5.13	5.20	5.49	7.92
7	3.16	3.19	3.26	3.26	3.29	5.99
8	1.71	1.86	1.90	1.93	1.93	2.84

**Table 9:** Number of revolutions sail spends inside target area with a cone angle constraint of  $\alpha_{\max} = 70^\circ$ , a clock angle constraint of  $\delta \in (-179; -1)$  and sail turning rates of  $\Omega_{\max} = 0.1^\circ/\text{s}$ ,  $0.25^\circ/\text{s}$ ,  $0.5^\circ/\text{s}$ ,  $1^\circ/\text{s}$  and  $2^\circ/\text{s}$ .

Table 9 presents the results of the hold trajectory optimisation, including a comparison with the Case of no turning rate restriction ( $\Omega_{\max} = \text{inf}$ ), representing  $\alpha_{\max} = 70^\circ$  as shown in Figure 4.3.4. For all turning rate constraints, the sail remains inside the hold volume for the maximum number of revolutions only in Cases 1-3. In contrast, without turning rate restrictions, the sail can maintain the maximum time in the hold volume starting from Case 4. This observation confirms the findings discussed in subsection 4.3.3. The anomaly observed in Case 4 with a turning rate of  $\Omega_{\max} = 2^\circ/\text{s}$  where the sail spends less time inside the hold volume compared to lower turning rates, can be attributed to local minima in the optimisation process. For a different seed (Seed=2), a higher revolution count is achieved.

For Case 2 and maximum turning rates of  $\Omega_{\max} = 0.1^\circ/\text{s}$ ,  $0.5^\circ/\text{s}$  and  $2^\circ/\text{s}$ , the optimised trajectories and corresponding control profiles are shown in Figure 48. The control profiles for all three cases exhibit similar behaviour. The cone angle remains near its maximum allowable value of  $\alpha_{\max} = 70^\circ$  throughout the revolution, only decreasing slightly at the beginning and end of each orbit. The clock angle stays nearly constant at  $\delta = -1^\circ$  until the end of the revolution. Consequently, even with the slightly increased acceleration at the start of the revolution, the in-plane acceleration remains minimal and does not significantly contribute to the already decreasing semi-major axis (see Figure 49).

Towards the end of the revolution, the cone angle decreases, leading to an increase in the in-plane acceleration component. This results in a faster rise of the semi-major axis, similar to the behaviour observed for  $\alpha_{\max} = 70^\circ$  under positive clock angle constraints (see Figure 45b and Figure 46). The cumulative difference between the semi-major axis of the sail and the target orbit is reduced, thereby mitigating drift as observed in the co-moving frame, as discussed in Chapter 3.

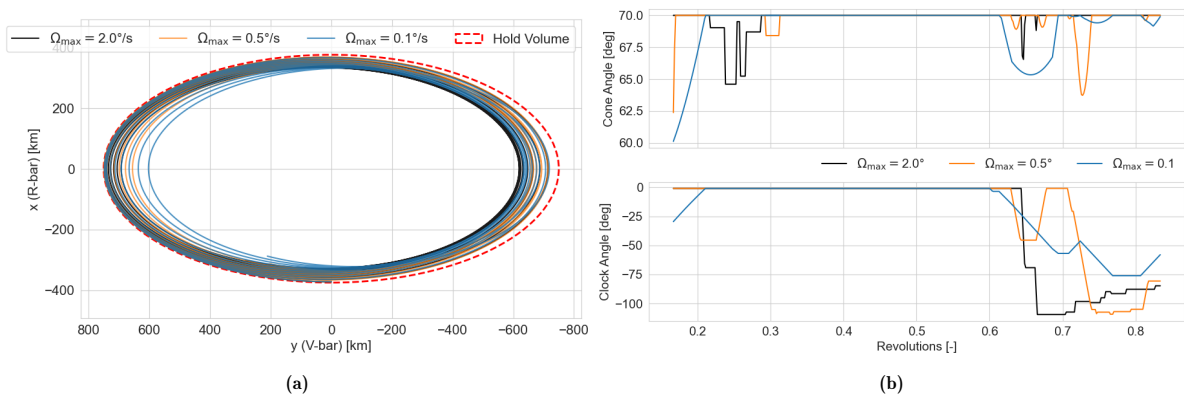


**Figure 48:** (a): Optimised hold trajectory and (b): corresponding sail control angles for combined constraints for maximum turning rates of  $\Omega_{\max} = 2.0^\circ/\text{s}$ ,  $0.5^\circ/\text{s}$  and  $0.1^\circ/\text{s}$  for Case 2, as shown in Table 9.

In contrast to the analysis of the negative clock angle constraints without turning rate limitations, which showed frequent large instantaneous attitude changes (see Figure 47b), the control profiles in Figure 48b show significant attitude changes only towards the end of the revolution. The rate of the attitude change becomes progressively slower as the maximum allowable turning rate decreases. Furthermore, these control profiles reduce the sail's eccentricity, as illustrated in Figure 50, causing the trajectories to spiral inward (see Figure 48a). This allows the sail to spend more time within the hold volume. However, as observed in previous cases (see Figure 46), the semi-major axis increases beyond that of the target orbit after the revolution. This gradually increases the semi-major axis, leading to an eventual drift in the negative V-bar direction.

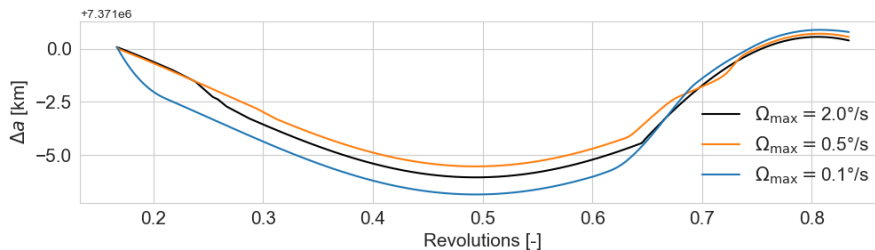


**Figure 49:** Difference in the semi-major axis compared to target orbit for  $\Omega_{\max} = 2.0^\circ/\text{s}$ ,  $0.5^\circ/\text{s}$  and  $0.1^\circ/\text{s}$  for Case 2, as shown in Table 9.

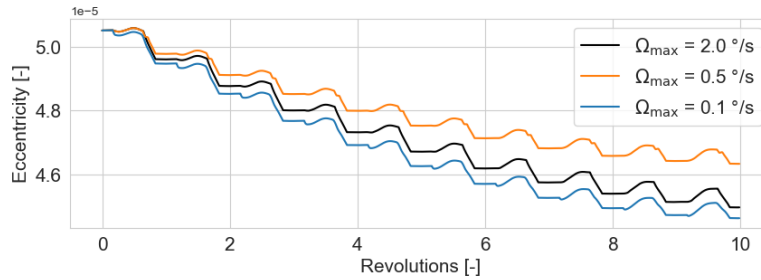


**Figure 50:** Eccentricity for optimised hold trajectories for  $\Omega_{\max} = 2.0^\circ/\text{s}$ ,  $0.5^\circ/\text{s}$  and  $0.1^\circ/\text{s}$  for Case 2, as shown in Table 9.

## 4.4. Safety Assessment

In an emergency, it is crucial for the solar sail to rapidly and safely increase its distance from the target. One method to achieve this is by quickly raising or lowering the semi-major axis, thereby inducing a drift in the negative or positive V-bar direction respectively. Figure 51 displays the trajectories in the co-moving frame for optimal semi-major axis raising and lowering manoeuvres with maximum cone angles of  $\alpha_{\max} = 60^\circ$ ,  $75^\circ$  and  $90^\circ$ , without restrictions on the turning rate, for an encircling hold trajectory (Case 1 as shown in  $\alpha_{\max} = 60^\circ$ ,  $75^\circ$  and  $90^\circ$ ). It can be seen that, in all cases, the sail passes through the safety zone and comes close to the target. For more constrained cone angles, the semi-major axis changes more slowly, leading to a slower drift in the negative or positive V-bar directions. This behaviour is consistent across all sizes of hold volumes for the encircling hold trajectory. Furthermore, if the sail becomes unresponsive and maintains a fixed attitude while following the hold trajectory, it will drift either towards or away from the target depending on the clock angle, as explained in Chapter 3. In both scenarios, the sail may pass through the safety zone, increasing the risk of collision. An example of this is shown in Figure C5.

For leading/trailing hold trajectories, a quick departure without passing the target is possible by performing an orbit lowering or raising manoeuvre, as described above, which causes the sail to drift away from the target in the positive or negative V-bar direction. However, in an emergency, following a strict control profile may not be feasible. If the sail becomes unresponsive and maintains a fixed attitude during the hold trajectory, the drift direction depends on the clock angle, as previously discussed. Without clock angle constraints, the sail could inadvertently drift towards the target under such circumstances.

To mitigate this risk, imposing a positive clock angle constraint for leading hold trajectories and a negative clock angle constraint for trailing hold trajectories ensures that if the sail becomes stuck in a certain attitude and cannot be controlled, it will move away from the target. This approach can be exploited in emergencies where the sail must quickly distance itself from the target. By simply maintaining its current attitude at any point during the hold trajectory, the sail will automatically drift away, eliminating the need for complex manoeuvres that could increase mission risk. For example, Figure 52 demonstrates this effect for Case 1 with a maximum allowable cone angle of  $\alpha_{\max} = 70^\circ$  and a positive clock angle profile (see subsection 4.3.4). In this case, a drift in the negative V-bar direction was observed due to an increase in the semi-major axis (see Figure 45a). Three points along the trajectory were selected and propagated for 15 revolutions, maintaining the sail's attitude at each point. The initial states and their respective control angles are listed in Table C2. All resulting trajectories drifted in the positive V-bar direction, confirming the findings of Section 3.3.

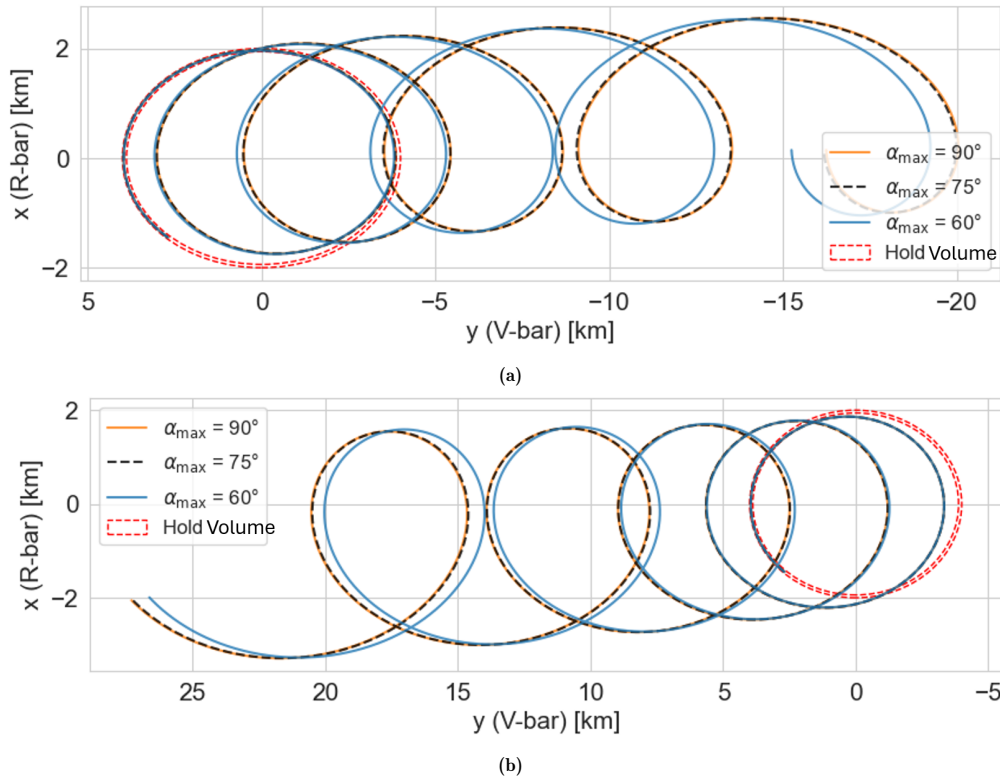


**Figure 51:** Trajectories to optimally a) raise and b) lower the semi-major axis for encircling hold trajectories.

Similarly, for a purely negative clock angle profile, the sail drifts in the negative V-bar direction. This is illustrated in Figure 53 for Case 1 with a maximum allowable cone angle of  $\alpha_{\max} = 70^\circ$  (see Figure 4.3.4). Again, three points along the trajectory were selected and propagated for 40 revolutions, maintaining the sail's attitude at each point. The initial states and corresponding sail attitudes are listed in Table C3. For States 1 and 3, a consistent drift in the negative V-bar direction is observed. However, for State 2, the sail initially drifts in the positive V-bar direction, reaching a maximum distance of 200 m from the hold volume over 11 revolutions before drifting back in the negative V-bar direction. These observations align with the previous findings (see Section 3.3).

## 4.5. Discussion

This chapter examined the feasibility of using hold trajectories for solar sails as an alternative to classical hold points in proximity operations, focusing on two types: encircling hold trajectories and leading/-trailing hold trajectories. The analysis explored the impact of various operational constraints, including cone angle limitations (to manage solar incidence for power generation or thermal control), turning rate restrictions (due to the torque limits of the attitude control system), and clock angle constraints. Additionally, the analyses sought to find favourable positions for the hold volume, considering safety factors. The key findings and their implications are discussed below.

An important observation from the analyses is that InTrance converged to control profiles, which repeat identically in each revolution. Furthermore, it is shown that sails with tight cone angle constraints rapidly drift out of small hold volumes for both types of hold trajectories. Consequently, sails with tighter cone angle constraints require larger hold volumes to remain close to the target for a longer

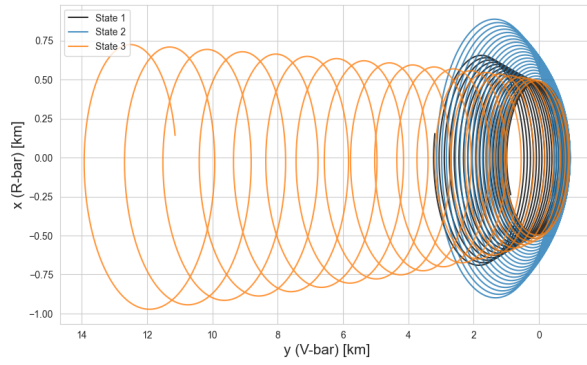


**Figure 52:** Safety analysis of sail trajectories with a constant sail attitude over 40 revolutions starting from the hold trajectory of case 1 with  $\alpha_{\max} = 70^\circ$  and a positive clock angle. Initial states are shown in Table C2

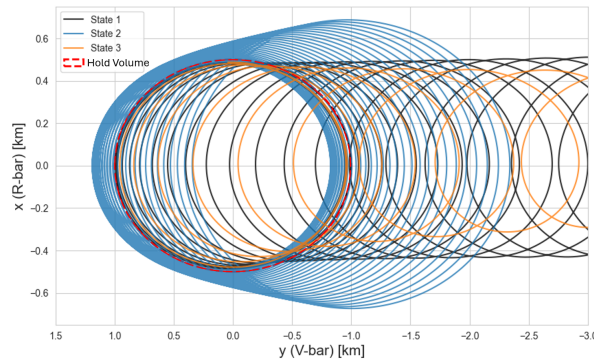


**Figure 53:** Safety analysis of sail trajectories with a constant sail attitude over 40 revolutions starting from the hold trajectory of case 1 with  $\alpha_{\max} = 70^\circ$  and a negative clock angle. Initial states are shown in Table C3

period of time. Moreover, for the majority of trajectories, the semi-major axis steadily increases or decreases with each revolution, even if the sail stays within its designated hold volume throughout the simulation period. This steady change in the semi-major axis eventually causes the sail to drift in the negative or positive V-bar direction, leading it out of the hold volume. This observation is independent of the constraints imposed on the sail or the size of the hold volume. It is also observed that sails with tighter cone angle constraints exhibit a faster change in the semi-major axis. Since nearly all trajectories maintain the cone angle at its maximum allowable value, tighter cone angle constraints result in larger overall acceleration, including a larger in-plane acceleration component, which leads to a faster change in the semi-major axis. However, during a revolution, the semi-major axis still changes, increasing or decreasing the eccentricity and thus inducing a shift in the left and right orbit crossings. Due to the smaller acceleration at larger cone angles, these changes are minimal, but they still cause the sail to eventually drift out of the hold volume. These shifts in the trajectory align with the analysis conducted in Chapter 3. Therefore, while a steering strategy that repeats each revolution can keep the sail within the hold volume for an extended period, the sail will eventually drift out. This occurs because the cumulative difference in the semi-major axis between the sail and the target orbit is not fully corrected within a single revolution, and the eccentricity changes are not sufficiently minimised to stabilise the trajectory.

To mitigate this drift, a potential solution is to utilise a control profile that repeats every two revolutions instead of each revolution. In this approach, during the first revolution, the control profile would slightly increase the semi-major axis while still trying to minimise the change to limit the induced shift of the

trajectory. In the next revolution, the semi-major axis is decreased below its initial value, inducing a drift in the opposite direction, effectively cancelling out the shift over multiple revolutions. At the same time, the change in eccentricity should also be minimised to decrease the sail's inward or outward spiralling, as seen in the co-moving frame. This approach could help maintain the sail within the hold volume indefinitely. Implementing such a strategy might even enable sails with tighter cone angle constraints to remain within smaller hold volumes, which would otherwise drift out more quickly. However, a minimal safety zone would still be required for encircling hold trajectories to account for potential deviations and uncertainties. Furthermore, smaller hold volumes necessitate a more agile sail, which may be constrained by the sail's operational capabilities, particularly its maximum turning rate, thus also limiting the minimum size of a leading/trailing hold volume.

Even if the proposed approach allows the sail to remain within the hold volume indefinitely, the encircling hold volume presents another problem. In case of an emergency, a quick and safe departure from the target object might not be possible. Although no dedicated trajectory optimisation was performed to avoid the safety volume during departure, experiments were conducted where the sail executed an optimal semi-major axis raising or lowering manoeuvre to increase the speed of drift away from the target. However, these resulting trajectories pass through the safety area, thereby posing a risk of collision. While departure over an inclined trajectory might be possible, thus avoiding the safety zone, executing a quick and safe departure in an emergency remains challenging. This difficulty arises because the control profile must be followed closely to avoid unintended drift toward the target, something that might not be feasible under emergency conditions. Similar issues apply when reaching the hold trajectory during the homing phase. An in-orbit-plane approach would lead the sail through the safety zone and potentially result in a close pass by the target object, increasing the collision risk. An inclined approach, where the orbits do not cross and the safety zone is avoided, might be a viable option. This approach is also known as a "walking ellipse" (Vavrina et al., 2019).

An advantage of encircling hold trajectories over the leading/trailing hold trajectory is the ability to observe the target from all sides, providing comprehensive data for missions requiring detailed inspections. For leading/trailing hold volumes, the target can only be observed from one side and limited angles as shown in Figure 54. This disadvantage is further amplified for smaller hold volumes as the angle of the line of sight to the target decreases. However, the persistent risk of the sail drifting toward the target poses significant safety concerns for encircling hold trajectories. In the event of an emergency or loss of control, it is difficult to ensure the sail can safely distance itself from the target without passing dangerously close.

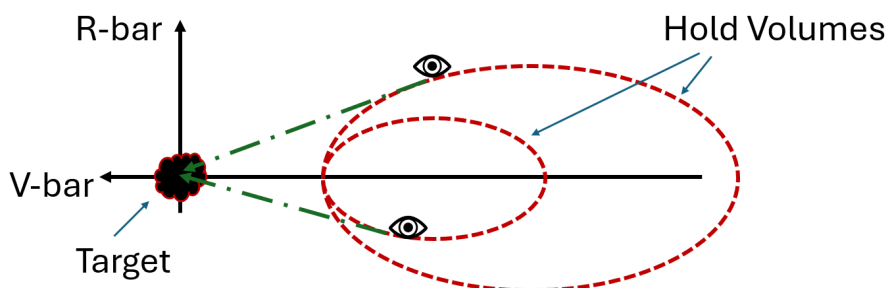


Figure 54: Line of sight on the target for trailing hold volumes.

In contrast, positioning the hold volume ahead of or behind the target allows the sail to perform an

orbit lowering or raising manoeuvre to quickly move in the positive or negative  $V$ -bar direction away from the target without passing it. Thus, considering safety, a leading or trailing hold volume is more advantageous. This also allows for a safe approach to a leading/trailing hold volume, as close passes to the target are avoided. Moreover, if precise steering is no longer possible, the sail can simply maintain a constant attitude with a positive or negative clock angle, causing it to naturally drift in the positive or negative  $V$ -bar direction over time. It should be noted that this behaviour is only possible if the trajectory passes through Earth's shadow (see Section 3.3). It has been shown that leading and trailing hold trajectories, which remain close to the target for an extended period of time, are possible, increasing safety even more. This way, if an emergency occurs or the sail needs to increase its distance to the target for other reasons at any point along the trajectory, the sail can maintain its current attitude, ensuring an eventual drift away from the target. This also removes the need for complicated departure manoeuvres. However, even with this advantage, the leading/trailing hold volume should maintain a minimum distance from the target. Maintaining a constant sail attitude with a positive or negative clock angle could still lead to an initial movement toward the target before eventually reversing direction. However, positioning the leading/trailing hold volume farther away from the target can hinder observability due to the increased distance between the sail and the target. This issue is further aggravated when using a less agile sail with a smaller maximum allowable cone angle, as such sails require larger hold volumes. Consequently, the point of the furthest approach is positioned even farther from the target, reducing the effectiveness of observations. One observed difference between leading and trailing hold trajectories is that leading hold trajectories require a larger hold volume than trailing hold trajectories for the same maximum allowable cone angle. Thus, the actual location of the hold volume in a mission depends on specific mission objectives. If closer proximity is required, a trailing hold volume may be preferable due to its ability to maintain a smaller hold volume given the same sail constraints.

The earlier proposed control profile, which repeats every two revolutions, could help mitigate this problem. By carefully managing the sail's semi-major axis and eccentricity over successive revolutions, it might be possible to reduce the size of the hold volume. It has been shown that, even under positive and negative clock angle constraints, the semi-major axis and eccentricity can be adjusted dynamically, potentially enabling the proposed manoeuvre even under these constrained conditions and, thus, remaining within the hold volume indefinitely. Furthermore, in leading/trailing hold trajectories, a safety zone within the encircled region of the hold trajectory is not required, so the minimum size of the hold volume is limited only by the sail's operational constraints. Reducing the hold volume's size not only brings the sail closer to the target, enhancing observation capabilities but also decreases the dispersion between the hold trajectory and the target orbit, a key objective during the homing phase of proximity operations (see subsection 2.2.2), by reducing the trajectory's eccentricity.

The analyses demonstrate that hold trajectories for solar sails are a feasible alternative to classical hold points, providing a means for the chaser to remain at a certain distance from the target for extended periods of time, even when accounting for the operational constraints of the sail. This capability provides opportunities to observe the target, perform system checks, and plan for upcoming close proximity operations. However, the design of these hold trajectories and the size and location of the hold volume must carefully consider operational constraints and safety implications. In-plane leading/trailing hold trajectories offer significant safety advantages compared to encircling hold trajectories, although they have the disadvantage of restricted observability of the target. In situations where parts of the trajectory

---

are eclipsed by Earth, employing a control profile with a purely negative or positive clock angle enables the sail, at any point during the trajectory, to keep its current attitude to ensure that it will eventually drift away from the target. This approach is particularly useful in the event of loss of control or in an emergency situation where precise steering may not be possible, as the sail can remain in its current attitude and still safely distance itself from the target. Ultimately, the choice of hold volume size and trajectory design depends on the mission's specific objectives and the sail's operational constraints. By prioritising safety and incorporating strategies to manage drift, solar sails can effectively maintain hold trajectories during proximity operations and reduce the risk of unintended approaches toward the target.

# 5

## Homing Trajectory Analysis

In traditional rendezvous missions, the homing phase involves manoeuvring the chaser spacecraft from a starting point several tens of kilometres away to a designated hold point near the target to reduce trajectory dispersion. The previous chapter established that hold trajectories are a viable alternative to classical hold points for solar-sail proximity operations. Positioning the hold volume ahead of or behind the target object reduces the risk of collision, thereby improving mission safety. Thus, reaching a hold volume and merging onto a hold trajectory becomes the main objective of the homing phase for solar-sail missions. Building upon these findings, this chapter investigates whether the trajectory optimisation tool InTrance, equipped with newly added functionalities, is suitable for optimising solar-sail homing trajectories that lead into a hold trajectory.

In this chapter, a homing trajectory is first optimised. The sail starts from an injection point located on the target orbit behind the target and should merge onto a trailing hold trajectory. Subsequently, to verify whether the optimisation is accurate enough, the final state of the optimised homing trajectory is used as the initial state for optimising a hold trajectory. If the hold trajectory optimisation converges successfully from this initial state, it indicates that the homing trajectory is accurate enough for practical purposes. Lastly, the results are discussed.

### 5.1. Homing Trajectory Optimisation

In this section, an initial investigation is conducted into the use of InTrance for homing trajectory optimisation of solar sails. The analysis assumes that the target object is in a circular, equatorial LEO at an altitude of  $\tilde{h} = 1000$  km. The target has an initial true anomaly of  $\theta_0 = 0^\circ$ , locating it behind the Earth as seen from the Sun. Initially, the sail is located behind the target along the x-axis as seen in the co-moving frame at  $x_0 = -10$  km and thus initially remains stationary with respect to the target. The sail has a lightness number of  $\beta = 7.7 \times 10^{-3}$ , and no operational constraints are imposed on it. Furthermore, the sail is targeting a trailing hold trajectory, which is obtained from a previous optimisation conducted in the prior chapter (refer to Table 4, Case 3, with  $\alpha_{\max} = 85^\circ$ ). The hold trajectory is centred around the origin of the co-moving frame to reduce inaccuracies due to the use of the CW equations. From this hold trajectory, ten states from the first revolution, equally spaced in

time, are selected as potential target states. These states are presented in Table 10.

Targeted State	x [m]	y [m]	z [m]	$v_x$ [m/s]	$v_y$ [m/s]	$v_z$ [m/s]	$\alpha$ [deg]	$\delta$ [deg]
1	-246.9285	0.0000	0.0000	0.0000	0.4927	0.0000	-35.6	64.3
2	-199.7384	290.3647	0.0000	0.1448	0.3985	0.0000	-35.5	65.7
3	-76.2682	469.6915	0.0588	0.2337	0.1516	0.0005	-57.3	71.7
4	74.7272	469.5362	0.7532	0.2296	-0.1509	0.0017	-50.9	70.9
5	194.3548	293.2657	2.1405	0.1381	-0.3892	0.0022	-93.3	79.3
6	237.9898	11.3843	3.0240	-0.0039	-0.4758	0.0004	-168.6	81.5
7	189.8389	-267.3613	2.5517	-0.1438	-0.3795	-0.0018	-121.2	85.0
8	68.6714	-435.7770	1.1136	-0.2280	-0.1373	-0.0023	-14.6	75.4
9	-78.8826	-429.1502	0.1391	-0.2246	0.1576	-0.0008	-30.4	75.7
10	-195.9178	-250.3682	-0.1240	-0.1349	0.3911	-0.0003	-27.6	68.2

**Table 10:** Targeted states used for homing trajectory optimisation

The objective of the homing trajectory optimisation is to minimise both the state deviation to one of the targeted states, including the sail's attitude and the time of flight (ToF), thereby creating a multi-objective optimisation problem, as explained in Eq. 2.3.3. In such cases, there is no single optimal solution; instead, a Pareto front represents the set of optimal trade-offs between objectives. However, the optimisation time for holding trajectories using InTrance is considerable (over 30 hours per run), so it is impossible to investigate the solution space thoroughly enough to produce a complete Pareto front within the given time frame. Consequently, only a limited number of optimisation runs could be conducted. Five runs were performed for this experiment, each initialised with a different random seed to explore different regions of the solution space. A maximum ToF of 40 revolutions (approximately 70 hours) of the target object was chosen for the homing trajectory optimisation. The maximum allowable errors for this optimisation were empirically chosen and set to  $\Delta r_{f,\max} = 20$  m for the final position error and  $\Delta v_{f,\max} = 0.01$  m/s for the final velocity error (as detailed in Eq. 2.3.3). Effectively, this means that only once these error constraints are met does the optimisation proceed to minimize the time of flight and align the sail's attitude. Before satisfying these constraints, the optimisation focuses solely on minimising the relative position and velocity errors. It is observed that if the maximum allowable errors are chosen to be smaller, the final distance and relative velocity deteriorate. The results obtained from these optimisation runs are presented in Table 11.

Seed	Targeted State	ToF [h]	$\Delta r_f$ [m]	$\Delta v_f$ [m/s]	Final Relative Attitude [°]
1	2	47.39	18.7	0.00448	10.8
2	3	43.59	17.667	0.00234	31.7
3	3	65.04	16	0.00814	15.6
4	10	53.79	17.99	0.0028	31.7
5	10	60.69	14.69	0.00586	9.48

**Table 11:** Results of the homing trajectory optimisation for an unrestricted solar sail.

All five trajectories satisfy the maximum allowable errors for the final position and velocity. Specifically, the final position errors  $\Delta r_f$  range from 14.69 m to 18.70 m, and the final velocity errors  $\Delta v_f$  range from 0.00234 m/s to 0.00814 m/s. The optimisations targeted different states on the hold trajectory, predominantly states 3 and 10, indicating no ideal location for merging onto the hold trajectory. Among the results, Seed 5 achieved the smallest final position error with  $\Delta r_f = 14.69$  m and also had the lowest

relative attitude dispersion of  $9.48^\circ$ . Seed 2 achieved the lowest final velocity error of  $\Delta v_f = 0.00234$  m/s and the shortest ToF of 43.59 h. The ToF for the homing trajectories ranges from approximately 43.6 hours to 65 hours. Considering that the initial distance to cover is around 10 km, these durations are substantial. However, when the maximum ToF is reduced, it is observed that the final distance and relative velocity errors increase. Specifically, starting from a maximum ToF of below 30 hours, the maximum allowable errors are no longer met (see Table C4).

Figure 55 and Figure 56 show the homing trajectory in the co-moving frame and the corresponding control profile from the optimisation run using seed 2, respectively. It is noted that, once again, the control profile repeats itself each revolution, similar to what was seen in the hold trajectory analysis as discussed in Chapter 4. The corresponding trajectory in the GEI frame, including the sail acceleration, is shown in Figure 57. It can be seen that the lowest point corresponding to the periapsis, as seen in the co-moving frame, steadily decreases while the highest point, the apoapsis, steadily increases. However, the periapsis decreases faster than the apoapsis increases, indicating an overall decrease in the orbit's semi-major axis. This behaviour can be explained by examining the sail's control angles throughout each revolution:

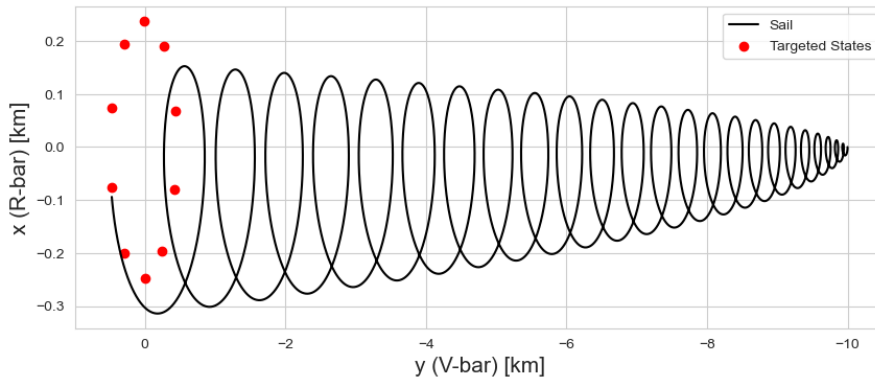


Figure 55: Homing trajectory in the co-moving frame.

- **First Third of the Revolution (see Figure 57; green arc):** During this phase, the sail is flying toward the Sun. The clock angle is approximately  $\delta = -90^\circ$ , corresponding to an in-plane acceleration, for most of this period, with the cone angle ranging between  $\alpha = 65^\circ$  and  $70^\circ$ . This configuration results in increased acceleration opposite to the direction of velocity, effectively decreasing the orbit's periapsis and the semi-major axis (see Figure 58).
- **Second Third of the Revolution (see Figure 57; black arc):** In this phase, the cone angle becomes quite large, sometimes even having an edge-wise attitude towards the Sun, reducing the overall acceleration acting on the sail. Consequently, the sail's trajectory and the semi-major axis are only slightly affected during this period (see Figure 58).
- **Final Third of the Revolution (see Figure 57; orange arc):** As the sail moves away from the Sun, the clock angle shifts to approximately  $\delta = 90^\circ$ , again corresponding to an in-plane acceleration, with the cone angle ranging between  $\alpha = 70^\circ$  and  $80^\circ$ . This generates an acceleration in the direction of velocity, leading to an increase in the apoapsis and the semi-major axis (see Figure 58). However, because the cone angle is quite large (resulting in a smaller effective acceleration), the increase in the apoapsis is less pronounced than the decrease in the periapsis observed during the first third of the revolution.

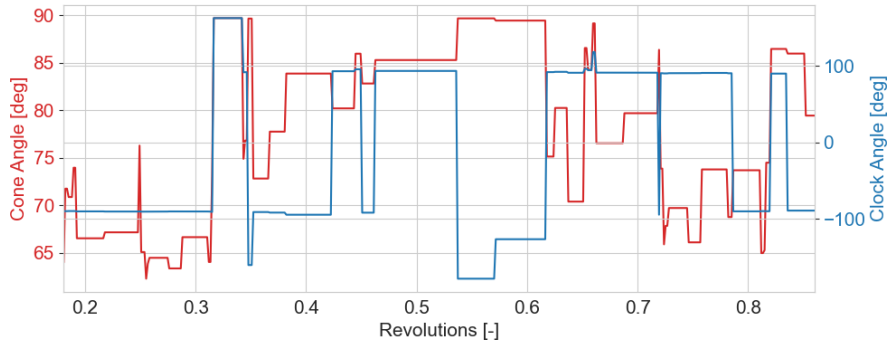


Figure 56: Repeating control profile for homing trajectory.

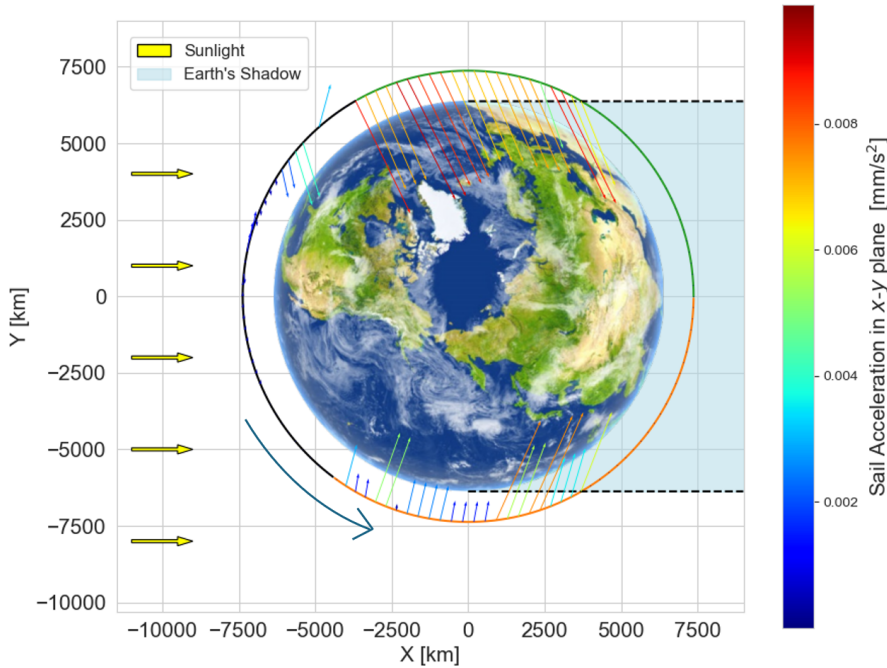
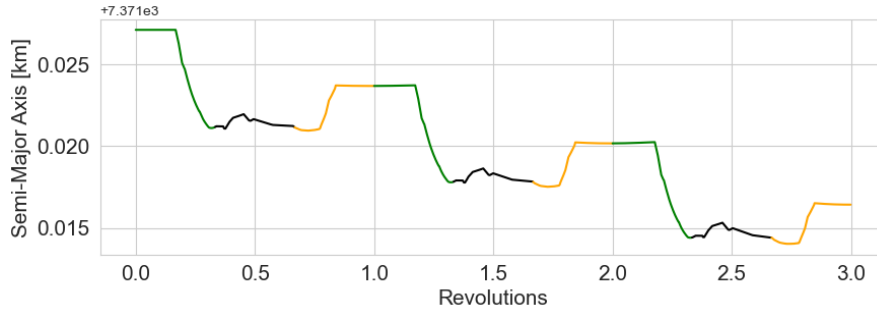


Figure 57: Homing trajectory, with sections of it highlighted for discussion, in the GEI frame, including the SRP acceleration acting on the sail.

Thus, the semi-major axis decreases continuously over the flight, as shown in Figure 58. However, it can be seen that initially, the sail has a semi-major axis of  $\tilde{a} = 7371.026$  km, even though the target orbit has a semi-major axis of  $\tilde{a} = 7371$  km. This slight difference arises from the coordinate transformation from the co-moving frame to the GEI frame to Keplerian elements. The sail's initial location is on the V-bar, which is directed towards the target's orbital velocity vector and thus does not lie directly in the target orbit. Nevertheless, the steady decrease of the semi-major axis during the flight is unaffected by this initial discrepancy. As explained in Section 3.3, reducing the semi-major axis causes the sail to drift in the positive V-bar direction, bringing it closer to the target. The relatively long flight time can also be attributed to the gradual decrease in the semi-major axis. Over the entire flight, the semi-major axis is reduced by approximately 100 m. This small reduction is sufficient to induce the necessary drift toward the target while still meeting the final maximum allowable errors since the targeted hold trajectory has the same semi-major axis as the target object. Achieving a shorter ToF would require a faster reduction in the semi-major axis. However, this would decrease the accuracy of the final state because the semi-major axis would be reduced significantly below that of the targeted hold trajectory.



**Figure 58:** Change in the semi-major axis of optimised homing trajectory, obtained with Seed 2 for the first three revolutions.

This also explains the increase in final position and relative velocity errors when the maximum ToF is decreased (as shown in Table C4). Furthermore, the decreasing periapsis and increasing apoapsis lead to an increasing eccentricity of the homing trajectory over time. Specifically, the eccentricity grows from an initial value of zero (for a circular orbit) to a final value of  $\tilde{e} = 3.19 \times 10^{-5}$ . In comparison, the targeted hold trajectory has an eccentricity of  $\tilde{e} = 2.0035 \times 10^{-4}$  (refer to Table 4, Case 3). Additionally, the homing trajectory's final periapsis and apoapsis are lower than those of the targeted hold trajectory. These discrepancies indicate that, while the set final maximum errors are met, the inaccuracies might be too large to merge onto the hold trajectory. Similar trends are observed in the other optimised trajectories shown in Table 11.

## 5.2. Hold Trajectory Optimisation

To verify if the accuracy of the obtained homing trajectory is sufficient to merge onto a hold trajectory, the final state of a homing trajectory is used to optimise a hold trajectory. For this experiment, the final state of the homing trajectory obtained by Seed 2 (see Table 11) is shown in Table 12 and the resulting, optimised hold trajectory in the co-moving frame and the corresponding control profile in Figure 59 and Figure 60, respectively.

x [m]	y [m]	z [m]	$v_x$ [m/s]	$v_y$ [m/s]	$v_z$ [m/s]
-93.90842	469.57080	-0.91777	0.23396	0.14931	0.00097

**Table 12:** Final state of the homing trajectory obtained with Seed 2, used as the initial state for the hold trajectory optimisation.

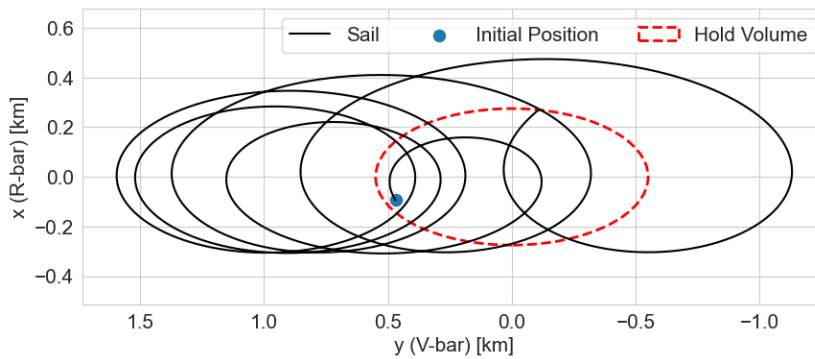


**Figure 59:** Optimised hold trajectory in the co-moving frame, starting from the final state of the homing trajectory obtained with Seed 2.

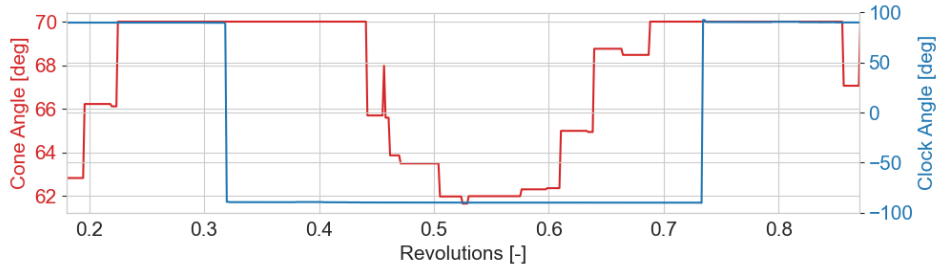


**Figure 60:** Sail control angles over time for the optimised hold trajectory starting from the final state of the homing trajectory obtained with seed 2.

It can be observed that the sail is not able to stay within the hold volume. Instead, the sail initially drifts in the positive V-bar direction and eventually back in the negative V-bar direction. During this process, the apoapsis continuously increases while the periapsis remains nearly constant. This behaviour is due to the sail's cone angle profile, which increases the time during which the acceleration points in the velocity direction. Additionally, since the acceleration is in-plane, the magnitude of the acceleration is maximised. As a result, the sail's semi-major axis continuously increases from an initial value smaller than the target orbit, eventually surpassing it (see Figure 61). This increase in the semi-major axis leads to the observed motion, as the optimiser still tries to maximise the time spent within the hold volume. This experiment was repeated using the final states of the other homing trajectories, leading to similar results. Therefore, even though the maximum allowable errors in position and velocity are met, the accuracy of the homing trajectories is insufficient to effectively merge onto a hold trajectory within the targeted hold volume. The discrepancies in orbital elements, particularly the semi-major axis and eccentricity, prevent the sail from reaching a desired hold trajectory.

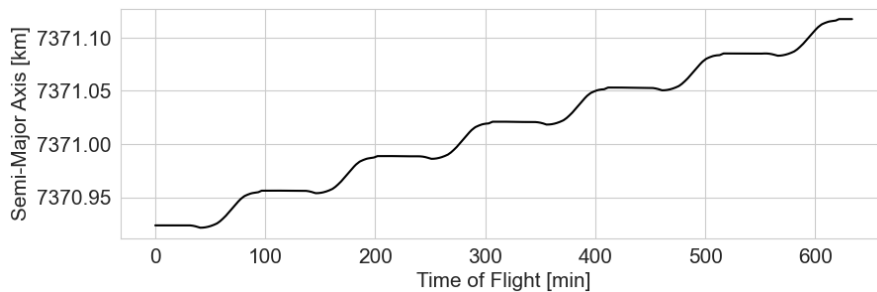


**Figure 61:** Change in the semi-major axis of optimised hold trajectory, starting from the final state of the homing trajectory obtained with Seed 2 (see Table 12).

## 5.3. Discussion

The experiments conducted in this chapter aimed to explore the feasibility of using the trajectory optimisation tool InTrance for designing homing trajectories for solar sails. Specifically, the goal was to assess whether InTrance's newly added functionalities could optimize homing trajectories that enable a solar sail to merge seamlessly onto a hold trajectory.

The optimisation results demonstrated that InTrance can find homing trajectories that meet the set maximum allowable errors for the final position and velocity in the co-moving frame. However, despite satisfying these constraints, the accuracy of the optimised trajectories is insufficient to allow for a seamless merge onto the hold trajectory. This shortcoming is due to the limitations of InTrance's

current configuration. It is observed that InTrance only converges to solutions where the control profile repeats each revolution. This repetitive control strategy poses a problem in the context of homing trajectories. A control profile is used, which decreases the semi-major axis of the sail’s orbit to initiate a movement in the positive  $V$ -bar direction towards the hold volume (when targeting a trailing hold volume behind the target). Consequently, the sail arrives at the hold volume with a semi-major axis smaller than the targeted hold trajectory. This discrepancy prevents the sail from directly merging onto the hold trajectory. A similar issue is expected to appear when targeting a leading hold volume ahead of the target. In this case, when the sail is initially located ahead of the hold volume, it must increase its semi-major axis to move towards the hold volume in the negative  $V$ -bar direction. Again, the sail would arrive with a semi-major axis different from the hold trajectory, restricting a seamless transition. Thus, the main problem is that with the current setup, InTrance seems to only identify control profiles that repeat every orbit, which restricts its ability to adjust the semi-major axis to align with the orbital parameters of the target trajectory at the point of merging. As a result, InTrance, in its current configuration, cannot be used to design homing trajectories that fully meet the requirements of the homing phase for solar sails, which necessitate precise matching of both position and orbital elements upon arrival.

Notably, InTrance has previously demonstrated the ability for multi-revolution steering strategies (Dachwald, 2005). One possible cause for the current shortcoming could be the NC input set used in the optimisation process. The values of the state input in the GEI frame are significantly larger than other inputs, potentially overshadowing them and causing the NC to neglect smaller but crucial state variables. A common solution to this issue is input normalisation, where the magnitude of the input set is scaled so that each input has a similar range (Liao & Carneiro, 2016). Normalisation could help ANNs by ensuring that all inputs contribute proportionally to the output, preventing dominance by inputs with larger magnitudes. An initial experiment was conducted to normalise the NC inputs to optimise homing trajectories. However, this did not make a significant difference in the optimisation results, indicating that other factors may also contribute to the issue and that further investigation is needed to make a proper assessment. Another potential problem might be the input set itself. In the experiments conducted Section 5.1, the inputs to the NC included the state vectors in both the GEI and co-moving frames and the Sun-sail vector in the co-moving frame. This information may be insufficient for the NC to learn and understand the problem effectively. Providing the NC with additional key information, such as the sail’s semi-major axis, eccentricity, or other orbital elements, might enhance its ability to generate more effective control strategies.

In addition to input-related issues, the neural network architecture may impact InTrance’s performance. Currently, the NC employs a network with one hidden layer consisting of 30 neurons (see Section B.3). While this configuration has been sufficient for previous problems involving solar-sail trajectory optimisation (Dachwald, 2005), more complex problems may require larger or deeper networks. Studies have shown that more complex tasks often necessitate neural networks with additional layers or more neurons per layer to capture patterns and dependencies in the data (Judd, 1990; Liu et al., 2017). By expanding the network architecture, the NC may be better equipped to learn the nuanced control strategies needed for accurate homing trajectory optimisation, potentially overcoming the current limitations observed with InTrance.

Furthermore, while InTrance can meet the final constraints of  $\Delta r_{f,\max} = 20$  m for the final position error

and  $\Delta v_{f,\max} = 0.01$  m/s for the final relative velocity during the optimisation of homing trajectories, these constraints are not sufficient to allow for a seamless merge onto the hold trajectory. When tighter final constraints are imposed (below  $\Delta r_{f,\max} = 20$  m and  $\Delta v_{f,\max} = 0.01$  m/s), InTrance is unable to meet them, and the solution deteriorates, while still outputting a repeating control profile. To address this issue, a possible solution is to split the homing phase into three distinct stages, each with specific objectives and control strategies. Taking the example of a sail targeting a trailing hold volume situated behind the target, the phases would be as follows:

- **Departure Phase:** In this initial phase, the sail departs from its starting location, the insertion point. The primary objective would be to decrease the semi-major axis of the sail's orbit. By lowering the semi-major axis, the sail induces a drift in the positive V-bar direction, moving it towards the hold volume (and the target). The magnitude of the decrease in the semi-major axis determines the drift rate; the larger the decrease, the faster the sail approaches the hold volume. However, this also means that in the event of loss of control, the sail may eventually pass the target object, posing a collision risk. Therefore, safety considerations must be considered when selecting the extent of the semi-major axis reduction. During this phase, the sail could adjust its eccentricity to match the hold trajectories.
- **Cruising Phase:** At the start of the cruising phase, the sail is already moving towards the hold volume with the reduced semi-major axis and adjusted eccentricity. The objective of this phase would be to maintain these orbital parameters, keeping the semi-major axis and eccentricity constant, to continue drifting towards the hold volume at a controlled rate. The control profile during this phase should focus on minimising deviations and ensuring the sail remains on the planned path, even if attitude constraints are imposed.
- **Merging Phase:** The arrival phase begins as the sail approaches the hold volume. The goal would be to increase the semi-major axis to match the target orbit and the hold trajectory. This adjustment must begin before reaching the hold volume, as the sail will continue to drift in the positive V-bar direction until its semi-major axis equals that of the target.

A separate control profile would be needed to achieve the specific goals of each phase. Implementing such a multi-phase strategy would require InTrance to optimise trajectories with varying control profiles across different stages, which with the current setup seems not possible.

# 6

## Conclusion and Recommendations

This thesis explores the feasibility of using solar sails for active debris removal (ADR) missions to clean up space debris in a sustainable manner. By investigating far-range rendezvous operations, the study aims to address the research gap in solar sail proximity operations, specifically bridging the gap between the phasing and close-range rendezvous phases while considering the sail's operational constraints. This chapter evaluates the results based on the research questions stated in Chapter 1 and provides recommendations for future work.

### 6.1. Conclusion

By introducing hold trajectories as an alternative to classical hold points, the research provides insights into how solar sails can continuously steer to prolong their stay relative to a target object. Furthermore, key challenges associated with the sail's operational constraints are addressed. This section answers the research questions posed at the outset of this thesis.

*1) Can hold trajectories replace classical hold points for solar sail far-range rendezvous operations?*

This thesis demonstrates that hold trajectories can effectively replace classical hold points in solar sail far-range rendezvous operations. Two types of hold trajectories are investigated (see Figure 62): encircling hold trajectories and leading/trailing hold trajectories.

*Encircling hold trajectories* involve the spacecraft performing a continuous fly-around manoeuvre around the target while staying within a designated hold volume. The hold volume is defined as the spatial region within which the chaser must remain during the hold phase. It consists of an inner and outer ellipsoid; the inner ellipsoid effectively functions as a safety zone that the spacecraft should not enter to minimise the risk of collision. In this configuration, the spacecraft can observe the target from all angles. *Leading/trailing hold trajectories* position the hold volume ahead of or behind the target along the orbital path and consist only of an outer ellipsoid. In this configuration, it is more advantageous to reduce the size of the hold trajectory to minimise the maximum distance to the target, allowing for better observability. One disadvantage is that the target, if non-rotating, can only be observed from

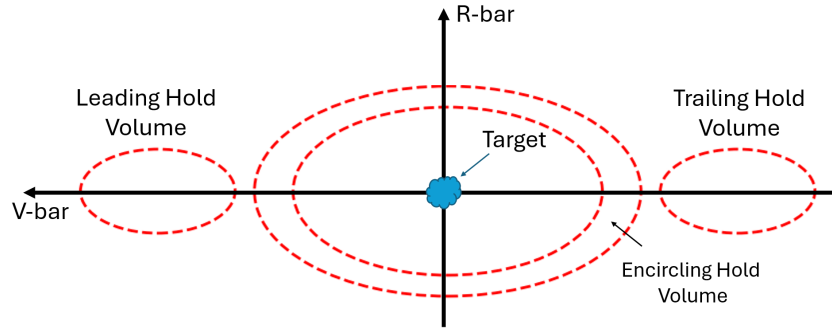


**Figure 62:** Encircling and leading/trailing hold volumes

one side.

The study considers hold trajectories that lie in the target's orbital plane. It is shown that solar sails could stay within designated hold volumes for extended periods of time, with only minor drifts observed depending on the sail's operational constraints. Control profiles are identified, which minimise the in-plane acceleration component to reduce drift. While these strategies may gradually change orbital inclination over time, they allow the solar sail to stay within the designated hold volume to perform observations or to prepare for the next phases of rendezvous operations.

2) *How do safety considerations and the sail's operational constraints affect the size and position of hold trajectories?*

The size and position of hold trajectories are significantly influenced by safety considerations and the operational constraints of the solar sail, such as maximum cone angle and turning rate. It is found that:

- A solar sail with larger cone angle constraints requires a larger hold volume to remain within it for extended periods. To precisely follow an orbit and counteract solar radiation pressure, the sail must orient edge-wise to the Sun. As the maximum allowable cone angle decreases, the minimal solar radiation pressure force that can be achieved increases, necessitating more space for manoeuvring.
- Tighter constraints on the sail's turning rate demand larger hold volumes because less agile sails cannot adjust their orientation as quickly. These two factors compound, requiring even larger hold volumes for sails with both larger cone angles and lower agility.

Safety is paramount in proximity operations, particularly for ADR missions involving passive targets incapable of evasive manoeuvres. The study shows that:

- *Encircling hold trajectories* in the same orbital plane as the target pose safety risks. In emergency situations, quick and safe departure is challenging because the sail may pass through the safety zone, increasing the risk of collision.
- *Leading/trailing hold trajectories* offer improved safety. Departures can be managed by adjusting the semi-major axis to rapidly increase the distance from the target without drifting towards it. However, in the event of loss of control, there remains a risk of the sail drifting towards the target.

To mitigate collision risk, limiting the clock angle to purely positive or negative values is proposed. This limitation leads to a minor but constant increase in the semi-major axis when using positive clock angles

and a decrease when using negative ones if the solar sail keeps a constant attitude. Consequently, this constraint ensures that the sail naturally drifts away from the target in an emergency by maintaining the current attitude, removing the need for complex evasive manoeuvres. It has been shown that, under this constraint, the sail can still manoeuvre within a designated hold volume for extended periods of time. However, this behaviour is only possible if parts of the trajectory are eclipsed.

In conclusion, leading/trailing hold volumes with a constrained clock angle profile are identified as the safer options for solar-sail proximity operations.

### *3) Can a preliminary homing trajectory for solar sails be designed with InTrance?*

The investigation revealed that, with the current implementation of InTrance and with the used input set for the neurocontroller (NC) and the current NC architecture, designing preliminary homing trajectories for solar sails that originate from an injection point on the target orbit and seamlessly lead into a hold trajectory is not possible. InTrance appears to converge exclusively to steering strategies that repeat every orbital revolution, which is insufficient for the more complex manoeuvres required for a homing trajectory.

To approach the target from an injection point located behind it, the chaser spacecraft must first reduce its semi-major axis to enter a lower orbit, inducing a drift towards the target. Then, to merge on the desired hold trajectory, the semi-major axis must be raised again to match the target's. Furthermore, the eccentricity must also be increased to allow for a seamless merge onto the targeted hold trajectory. This process requires at least two distinct steering strategies: One that lowers the semi-major axis to initiate the drift towards the target and a second one to raise the semi-major axis to align with the hold trajectory to stop the drift and merge onto the hold trajectory seamlessly.

InTrance, as it is used in this research, may be limited by a number of factors. First, the choice of the NC's input set might not provide sufficient information to learn and understand the problem of effectively generating a control profile for homing trajectories. While the spacecraft's state in the geocentric equatorial inertial reference frame and in the co-moving frame is provided, key information, such as the sail's semi-major axis, eccentricity, or other orbital elements, might be missing. Furthermore, the currently used architecture of the NC might be insufficient to learn such a complex problem. A larger network may be required to learn the nuanced control strategies needed for accurate homing trajectories. While InTrance is a valuable tool for certain mission designs, it cannot, in its present form, design the required homing trajectories for solar sails in ADR missions that necessitate multi-phase manoeuvres.

## **6.2. Recommendations**

While this study has demonstrated the potential of solar sails in far-range rendezvous operations for ADR missions, several challenges and limitations have been identified that require further investigation. Addressing these issues is crucial to ensure mission safety and effectiveness before advancing to the subsequent phases of solar-sail proximity operations, such as close-range rendezvous and docking. This section outlines key recommendations and areas for future work to overcome the identified problems and enhance the application of solar sails in ADR missions.

## 1) Exploration of Inclined Hold Trajectories

While leading/trailing hold trajectories with a clock angle constraint have been shown to enhance safety by ensuring the solar sail drifts away from the target, this safety feature is only effective when the trajectory passes through Earth's shadow. However, many debris objects are situated in orbits that do not experience significant eclipses, such as sun-synchronous orbits, which are constantly illuminated, or high-altitude orbits like Geostationary Earth Orbit, where eclipses are brief and infrequent. In these cases, the safety benefits of the clock angle constraint are diminished or absent. Future work could explore the use of inclined hold trajectories, which could have the following benefits:

- **Improved Safety:** By introducing an inclination to the hold trajectory, the chaser spacecraft can avoid the target's orbital plane, significantly reducing the risk of collision. This inclination allows for quick and safe departure paths, and even in the event of loss of control, any forward or backward drift would not result in a close pass by the target, depending on the inclination angle. The inclined trajectory effectively separates the chaser's path from the target's orbit, which could increase overall mission safety.
- **Improved Observability:** The increased safety provided by an inclined orbit opens the possibility of implementing encircling hold trajectories without endangering the chaser spacecraft. With the chaser orbiting at an inclination relative to the target, it can perform a fly-around manoeuvre that offers improved observability of the debris object from multiple angles.
- **Prolonged stay within hold volume:** Previous findings indicated that with a control profile repeating each revolution, the chaser eventually drifts out of the hold volume, as the semi-major axis can not be held constant. A proposed solution involves designing a control profile that increases the semi-major axis during one revolution and decreases it during the subsequent revolution, resulting in a net zero change over two revolutions. However, this strategy requires a steering approach that, when in the same orbital plane as the target, could lead to the chaser drifting toward the target in the event of losing control. However, an inclined orbit would mitigate this risk and make it feasible to allow the sail to stay within the hold volume indefinitely.

Exploring inclined hold trajectories thus offers significant potential for improving the safety, observability, and operational duration of solar-sail ADR missions. Future research should focus on optimising these trajectories and developing suitable control strategies to fully utilise these advantages.

## 2) Homing Trajectory Design

In the homing trajectory analysis conducted in this work, it was shown that a control profile repeating each revolution cannot be used to design an entire homing trajectory when the injection point is located on the target orbit. To seamlessly merge onto a hold trajectory, a multi-phase steering strategy is necessary. Therefore, future work should focus on achieving a successful transfer from the injection point to the hold volume. A proposed design for a homing trajectory when the injection point is located behind the targeted hold volume should proceed as follows:

- **Departure:** The departure phase aims to initiate movement towards the target by decreasing the semi-major axis. The greater the reduction, the faster the drift towards the target. The eccentricity could also be increased during this phase to match the targeted hold trajectory.
- **Cruising:** Once the desired semi-major axis is achieved, the cruising phase begins. Given that the sail's operational constraints may not allow edge-wise positioning towards the Sun, it is essential

to keep the semi-major axis and eccentricity as constant as possible to ensure a smooth drift towards the target.

- **Merging:** In the merging phase, the semi-major axis is increased to match the targeted hold trajectory. This adjustment must occur before reaching the hold volume because, even while increasing the semi-major axis, the sail continues to drift in the positive V-bar direction.

To properly merge onto a hold trajectory, the final distance and relative velocity to a state on the hold trajectory must be sufficiently small. It is shown that tolerances of 20 m in position and 0.01 m/s in velocity were not sufficient for a seamless merge, suggesting that stricter constraints are necessary. Investigating how small these constraints need to be to merge successfully onto the hold trajectory is an important area for future research.

In the current configuration and with the input sets used, InTrance always appears to converge to a repeating control profile and thus cannot find a trajectory that successfully merges onto a hold trajectory. The issue might stem from an unsuitable choice of input parameters, as they may be heavily problem-dependent. Adjusting these input sets may improve the optimisation outcomes. Previous research has shown that InTrance can generate more complex, multi-phase steering strategies for a wide range of mission scenarios (Dachwald, 2005). Therefore, further research could be conducted to adapt InTrance for this problem, as the software is flexible and can be utilised for different mission scenarios in proximity operations with only minor modifications to the codebase.

To assess InTrance's performance for this optimisation problem, potentially more robust optimisation algorithms such as PSOPT (Becerra, 2010) should also be considered. These algorithms might offer enhanced optimisation capabilities but would require an initial guess for the steering strategy, a requirement that is not necessary when using InTrance. The need for an initial guess reduces the degree of freedom InTrance provides, which is considered one of its main advantages. Exploring both approaches could provide valuable insights into the most effective methods for homing trajectory optimisation.

### 3) Enhancing the Simulation Model

This work conducted an initial analysis focusing on demonstrating the feasibility of solar-sail hold and homing trajectories rather than providing a full-fledged trajectory design. As a result, a simplified environmental model was used, and assumptions were made to simplify the model further to concentrate on the fundamental dynamics. However, several enhancements to the model should be considered in future work to improve the accuracy of the simulations. Below, three possible areas are proposed:

- **Perturbations:** The spacecraft is influenced by various perturbations such as atmospheric drag, albedo radiation, third-body perturbations, and geopotential anomalies like Earth's oblateness ( $J_2$ -effect). Including all these perturbations simultaneously would significantly increase the complexity of the model and could obscure the impact of each individual factor. Therefore, it is recommended to incorporate perturbations incrementally, starting with those with the most significant influence. Atmospheric drag is the first perturbation that should be included, as it has a considerable impact on spacecraft in Low Earth Orbit (Wakker, 2015), especially for solar sails, which have a large frontal area. While an unconstrained sail may be turned edge-wise to the Sun to reduce the solar radiation pressure force acting on it, this orientation still exposes the sail to atmospheric drag. As the drag force is always directed, opposing the velocity direction, it leads to a decline in the semi-major axis and, thus, to an eventual drift in the positive V-bar direction.

Including atmospheric drag in the simulation would provide a more accurate representation of the sail's behaviour over time.

- **Propagator/ Integrator:** The current model uses the Clohessy-Wiltshire equations to propagate the chaser in the co-moving frame. Although this approach offers computational advantages, the accuracy of the trajectory suffers as the spacecraft moves farther from the frame's origin and as the propagation time increases. Switching to a two-body equation of motion and integrating it with the RK45 ODE can drastically improve accuracy, particularly at larger distances. However, this would increase the computational load, potentially lengthening optimisation times. For close-range rendezvous manoeuvres or docking operations, where distances are small, the CW equations may still provide sufficient accuracy while offering computational advantages.
- **Sail Model:** The ideal sail model used to describe the force exerted by solar radiation pressure on the sail could be enhanced by employing an optical force model. The optical force model considers the sail's reflective, absorptive, and transmissive properties, as well as the sail's temperature. This approach would account for the transverse component of the solar radiation pressure force exerted on the sail, which is neglected in the ideal model that assumes the force is aligned with the sail's normal vector. Incorporating the optical force model would improve the accuracy of the simulation. However, the previously mentioned factors, atmospheric drag and higher-fidelity orbital dynamics, are likely to have a more significant impact on the overall accuracy and should be prioritised.

By enhancing the simulation model to include these factors, future research can provide more accurate and reliable results, enabling better assessment of control strategies and mission feasibility. These improvements are essential for advancing from initial feasibility studies to detailed mission planning and design for solar sail active debris removal missions.

#### 4) Investigation of Subsequent Proximity Phases

This work focused on bridging the gap between the phasing phase and close-range proximity operations by investigating hold trajectories as alternatives to classical hold points and conducting an initial analysis of homing trajectories. It was demonstrated that observing the target safely from a distance is feasible using hold trajectories. This capability could already benefit regular ADR missions by allowing the chaser spacecraft to investigate the characteristics of the debris object, such as its shape, rotation rate, and surface properties.

However, to fully explore the potential of solar sails in active debris removal, it is necessary to investigate whether they can capture orbital debris. Achieving this requires exploring the subsequent phases of proximity operations beyond far-range rendezvous, specifically close-range proximity operations, mating, and docking procedures. In these phases, safety becomes even more critical due to the large area of the sail and its limited agility, which could pose significant hazards during close interactions with the target debris.

One of the key challenges in these subsequent phases is the need to detumble the debris object before attempting mating or docking. Many debris objects are tumbling uncontrollably, and attempting to capture such an object with a solar sail directly could result in the sail itself starting to spin. This unintended rotation could cause damage to the sail's delicate structure, including its slender booms and large, thin membrane, potentially compromising the mission.

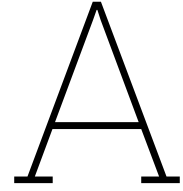
# Bibliography

- Astroscale. (2024). Space Debris Fly-Around Observation [Online; accessed October 19, 2024]. <https://astroscale.com/astrocales-adras-j-continues-to-make-history-successfully-demonstrates-fly-around-observations-of-space-debris/>
- Bäck, T., & Schwefel, H.-P. (1993). An overview of evolutionary algorithms for parameter optimization. *Evolutionary computation*, 1(1), 1–23.
- Bastida Virgili, B., & Krag, H. (2009). Strategies for active removal in leo. *Fifth European Conference on Space Debris*, 672, 53.
- Becerra, V. M. (2010). Solving complex optimal control problems at no cost with PSOPT. *2010 IEEE international symposium on computer-aided control system design*, 1391–1396.
- Bianchi, C., Niccolai, L., Mengali, G., & Ceriotti, M. (2024). Preliminary design of a space debris removal mission in leo using a solar sail. *Advances in Space Research*.
- Bonnal, C., & McKnight, D. S. (2017). *Iaa situation report on space debris 2016*. International Academy of Astronautics (IAA).
- Buchs, R., & Florin, M.-V. (2021). Collision risk from space debris: Current status, challenges and response strategies.
- Caudill, M., & Butler, C. T. (1990). *Naturally intelligent systems*. MIT press.
- Chai, R., Savvaris, A., Tsourdos, A., Chai, S., & Xia, Y. (2019). A review of optimization techniques in spacecraft flight trajectory design. *Progress in aerospace sciences*, 109, 100543.
- Chen, X.-q., & Yu, J. (2017). Optimal mission planning of geo on-orbit refueling in mixed strategy. *Acta Astronautica*, 133, 63–72.
- Choi, J. H., Park, C., & Lee, J. (2024). Mission planning for active removal of multiple space debris in low earth orbit. *Advances in Space Research*.
- Conway, B. A. (2010). *Spacecraft trajectory optimization* (Vol. 29). Cambridge University Press.
- Curtis, H. D. (2013). *Orbital mechanics for engineering students*. Butterworth-Heinemann.
- Dachwald, B. (2005). Optimization of very-low-thrust trajectories using evolutionary neurocontrol. *Acta Astronautica*, 57(2-8), 175–185.
- Dachwald, B., Ohndorf, A., & Wie, B. (2006). Solar sail trajectory optimization for the solar polar imager (spi) mission. *AIAA/AAS Astrodynamics Specialist Conference and Exhibit*, 6177.
- European Space Agency. (2023a). Mitigating space debris generation [Online; accessed March 04, 2024]. [https://www.esa.int/Space\\_Safety/Space\\_Debris/Mitigating\\_space\\_debris\\_generation](https://www.esa.int/Space_Safety/Space_Debris/Mitigating_space_debris_generation)
- European Space Agency. (2023b). Space Environment Statistics [Online; accessed February 19, 2024]. <https://sdup.esoc.esa.int/discosweb/statistics/>

- European Space Agency. (2024). Space Debris by the Numbers [Online; accessed October 19, 2024]. [https://www.esa.int/Space\\_Safety/Space\\_Debris/Space\\_debris\\_by\\_the\\_numbers](https://www.esa.int/Space_Safety/Space_Debris/Space_debris_by_the_numbers)
- Fehse, W. (2003). *Automated rendezvous and docking of spacecraft* (Vol. 16). Cambridge University Press.
- Galván, E., & Stapleton, F. (2023). Evolutionary multi-objective optimisation in neurotrajectory prediction. *Applied Soft Computing*, *146*, 110693.
- Goodman, J. L. (2006). History of space shuttle rendezvous and proximity operations. *Journal of Spacecraft and Rockets*, *43*(5), 944–959.
- Grigorescu, S. M., Trasnea, B., Marina, L., Vasilcoi, A., & Cocias, T. (2019). Neurotrajectory: A neuroevolutionary approach to local state trajectory learning for autonomous vehicles. *IEEE Robotics and Automation Letters*, *4*(4), 3441–3448.
- Gurfil, P. (2023). Spacecraft rendezvous using constant-magnitude low thrust. *Journal of Guidance, Control, and Dynamics*, *46*(11), 2183–2191.
- Hainaut, O. R., & Williams, A. P. (2020). Impact of satellite constellations on astronomical observations with eso telescopes in the visible and infrared domains. *Astronomy & Astrophysics*, *636*, A121.
- Heaton, A., Ahmad, N., & Miller, K. (2017). Near earth asteroid scout solar sail thrust and torque model. *International Symposium on Solar Sailing (ISSS)*.
- Hudson, J. S., & Kolosa, D. (2020). Versatile on-orbit servicing mission design in geosynchronous earth orbit. *Journal of Spacecraft and Rockets*, *57*(4), 844–850.
- Jalali, S. M. J., Hedjam, R., Khosravi, A., Heidari, A. A., Mirjalili, S., & Nahavandi, S. (2020). Autonomous robot navigation using moth-flame-based neuroevolution. *Evolutionary Machine Learning Techniques: Algorithms and Applications*, 67–83.
- Johnson, L., Whorton, M., Heaton, A., Pinson, R., Laue, G., & Adams, C. (2011). Nanosail-d: A solar sail demonstration mission. *Acta astronautica*, *68*(5-6), 571–575.
- Judd, J. S. (1990). *Neural network design and the complexity of learning* (Vol. 2). MIT press.
- Kelso, T., et al. (2009). Analysis of the iridium 33-cosmos 2251 collision. *Advances in the Astronautical Sciences*, *135*(2), 1099–1112.
- Kessler, D. J., Johnson, N. L., Liou, J., & Matney, M. (2010). The kessler syndrome: Implications to future space operations. *Advances in the Astronautical Sciences*, *137*(8), 2010.
- Ketkar, N., Moolayil, J., Ketkar, N., & Moolayil, J. (2021). Convolutional neural networks. *Deep learning with Python: learn best practices of deep learning models with PyTorch*, 197–242.
- Lemmens, S., & Letizia, F. (2020). Space traffic management through environment capacity. *Handbook of Space Security: Policies, Applications and Programs*, 845–864.
- Liao, Z., & Carneiro, G. (2016). On the importance of normalisation layers in deep learning with piecewise linear activation units. *2016 IEEE winter conference on applications of computer vision (WACV)*, 1–8.
- Liu, W., Wang, Z., Liu, X., Zeng, N., Liu, Y., & Alsaadi, F. E. (2017). A survey of deep neural network architectures and their applications. *Neurocomputing*, *234*, 11–26.

- Losada, F. G. (2024). Maximum torque of reaction wheels used by lightsail-2 and asc3.
- Macdonald, M., & McInnes, C. R. (2005). Analytical control laws for planet-centered solar sailing. *Journal of Guidance, Control, and Dynamics*, 28(5), 1038–1048.
- Mark, C. P., & Kamath, S. (2019). Review of active space debris removal methods. *Space policy*, 47, 194–206.
- McInnes, C. R. (2004). *Solar sailing: Technology, dynamics and mission applications*. Springer Science & Business Media.
- Rodrigues, O. (1840). Des lois géométriques qui régissent les déplacements d'un système solide dans l'espace, et de la variation des coordonnées provenant de ces déplacements considérés indépendamment des causes qui peuvent les produire. *Journal de mathématiques pures et appliquées*, 5, 380–440.
- Russell, C. T. (1971). Geophysical coordinate transformations. *Cosmic electrodynamics*, 2(2), 184–196.
- Samek, W., Montavon, G., Lapuschkin, S., Anders, C. J., & Müller, K.-R. (2021). Explaining deep neural networks and beyond: A review of methods and applications. *Proceedings of the IEEE*, 109(3), 247–278.
- Sato, T. (1999). Shape estimation of space debris using single-range doppler interferometry. *IEEE transactions on geoscience and remote sensing*, 37(2), 1000–1005.
- Schaub, H., Jasper, L. E., Anderson, P. V., & McKnight, D. S. (2015). Cost and risk assessment for spacecraft operation decisions caused by the space debris environment. *Acta Astronautica*, 113, 66–79.
- Shan, M., Guo, J., & Gill, E. (2016). Review and comparison of active space debris capturing and removal methods. *Progress in aerospace sciences*, 80, 18–32.
- Sharma, S., Sharma, S., & Athaiya, A. (2017). Activation functions in neural networks. *Towards Data Sci*, 6(12), 310–316.
- Shirazi, A., Ceberio, J., & Lozano, J. A. (2018). Spacecraft trajectory optimization: A review of models, objectives, approaches and solutions. *Progress in Aerospace Sciences*, 102, 76–98.
- Swingler, K. (1996). *Applying neural networks: A practical guide*. Morgan Kaufmann.
- Tsuda, Y., Mori, O., Funase, R., Sawada, H., Yamamoto, T., Saiki, T., Endo, T., & Kawaguchi, J. (2011). Flight status of ikaros deep space solar sail demonstrator. *Acta astronautica*, 69(9-10), 833–840.
- Union of Concerned Scientists. (2023). Number of Satellites in GEO [Online; accessed February 20, 2024]. <https://www.ucsusa.org/resources/satellite-database#.W7WcwpMza9Y>
- Vavrina, M. A., Skelton, C. E., DeWeese, K. D., Naasz, B. J., Gaylor, D. E., & Dsouza, C. (2019). Safe rendezvous trajectory design for the restore-l mission. *Advances in the Astronautical Sciences*, 168, 3649–3668.
- Wakker, K. F. (2015). Fundamentals of astrodynamics. *TU Delft Repository, Delft*.
- Wetherell, N. (2022). Optimization of orbital trajectories using neuroevolution of augmenting topologies.
- Wie, B. (2004). Solar sail attitude control and dynamics, part 1. *Journal of Guidance, Control, and Dynamics*, 27(4), 526–535.

- 
- Wilkie, K., & Fernandez, J. (2023). Advanced composite solar sail system (acs3) mission update. *The 6th International Symposium on Space Sailing*.
- Wu, Y.-c., & Feng, J.-w. (2018). Development and application of artificial neural network. *Wireless Personal Communications*, 102, 1645–1656.



# Verification and Validation

The first appendix discusses the verification and validation of the major methods applied during this thesis work.

## A.1. Coordinate Transformations

During this work, coordinate transformations from the inertial frame to the co-moving frame and back had to be carried out. To verify the transformation algorithm, reference (Curtis, 2013) was used.

The state of the target and the chaser in the inertial frame are shown in Table A1. The transformed co-moving state, rounded to match the precision of the reference, and the error is shown in Table A2. The errors, when transforming the obtained co-moving state back into the inertial frame compared to the initial state, are shown in Table A3. Given that all errors are within acceptable limits, it can be said that the implemented transformation logic works correctly.

	$X_I$ [km]	$Y_I$ [km]	$Z_I$ [km]	$dX_I$ [km/s]	$dY_I$ [km/s]	$dZ_I$ [km/s]
Target	-266.77	3865.8	5426.2	-6.4836	-3.6198	2.4156
Chaser	-5890.7	-2979.8	1792.2	0.935 83	-5.2403	-5.5009

**Table A1:** Inertial state of target and chaser for Verification of coordinate transformation from inertial to co-moving frame

	$x_M$ [km]	$y_M$ [km]	$z_M$ [km]	$dx_M$ [km/s]	$dy_M$ [km/s]	$dz_M$ [km/s]
Curtis, 2013	-6701.2	6828.3	-406.26	0.316 67	0.111 99	1.2470
Own Results	-6701.2	6828.28	-406.236	0.316 667	0.112 04	-5.5009
Error [%]	$-3.2 \times 10^{-4}$	$3.1 \times 10^{-4}$	$5.92 \times 10^{-3}$	$-4.198 \times 10^{-2}$	$-4.267 \times 10^{-2}$	$3.64 \times 10^{-3}$

**Table A2:** Transformed co-moving state of chaser and error for the verification of coordinate transformation from inertial to co-moving frame

	$X_I$	$Y_I$	$Z_I$	$dX_I$	$dY_I$	$dZ_I$
Error [%]	$-1.54395 \times 10^{-14}$	0.0	$6.34342 \times 10^{-14}$	$-1.06772 \times 10^{-13}$	$1.69490 \times 10^{-14}$	0.0

**Table A3:** Error of coordinate transformation from co-moving to inertial frame

## A.2. Force Model

Within this work, the ClohessyWiltshire equations have been used, to propagate a spacecraft within the co-moving frame and thus the force model within InTrance required an update.

The CW equations were first implemented into a Python script, which was then verified using multiple references (Fehse, 2003) (Curtis, 2013). An example of this verification is shown in Figure A1. It can be seen that the obtained results are the same as the reference (Curtis, 2013).

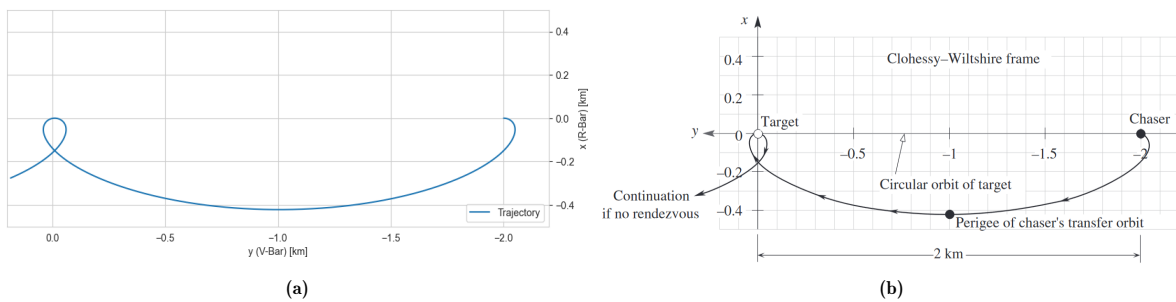


**Figure A1:** Comparing the propagation of an initial condition for results originating from a) thesis work b) (Curtis, 2013)

The force model implemented in InTrance was validated by generating a trajectory with InTrance and using the resulting sail attitude within the already verified Python-script to re-propagate the trajectory. The position and velocity in  $x$ -,  $y$ - and  $z$ -direction of the re-propagated trajectory in Python (left column), the outcome of InTrance (centre column) and the difference between those two are presented in Figure A2 and Figure A3 respectively. In both cases, a build-up of numerical errors is observed. With such accuracy, it can be concluded that the force model was correctly implemented into InTrance.

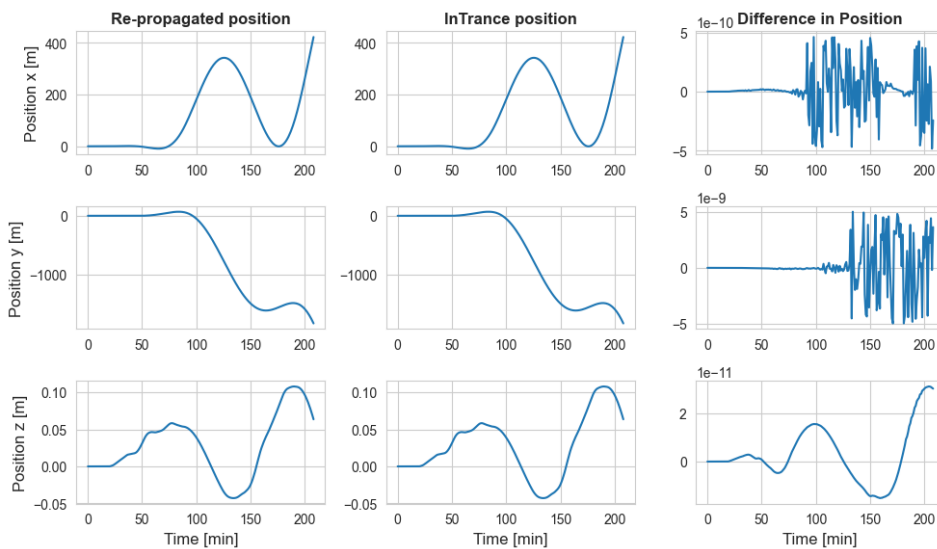


**Figure A2:** Verification of co-moving position of the new force model.

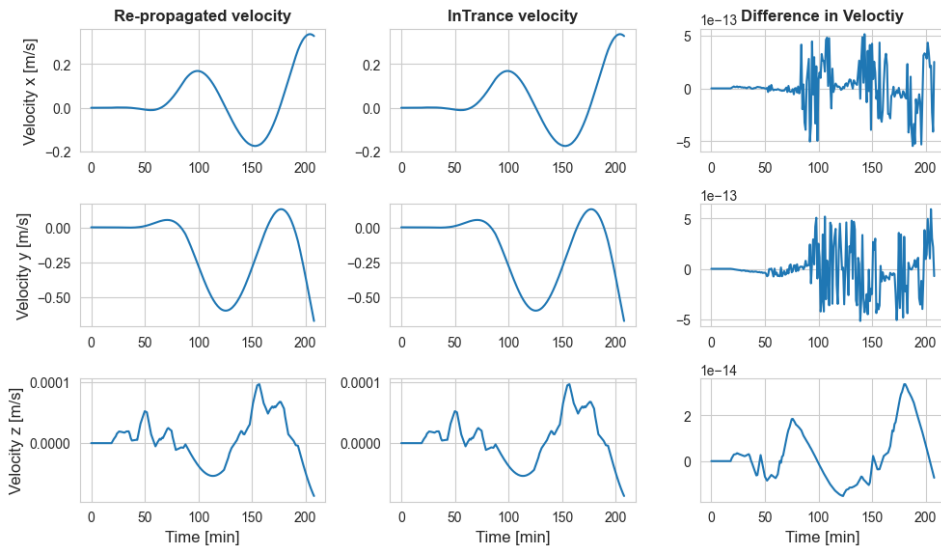


Figure A3: Verification of co-moving velocity of the new force model.

### A.3. Cylindrical Shadow Model

In this thesis, a cylindrical shadow model was employed. Several Keplerian orbits around Earth with varying properties were propagated to validate this model. At each step, the spacecraft's position relative to the shadow was assessed, and the results were plotted. An example is shown in Figure A4. The eclipsed part of the trajectory is highlighted with a dotted line. It can be seen that only the segments of the trajectory within the shadow are highlighted, demonstrating that the model has been implemented correctly.

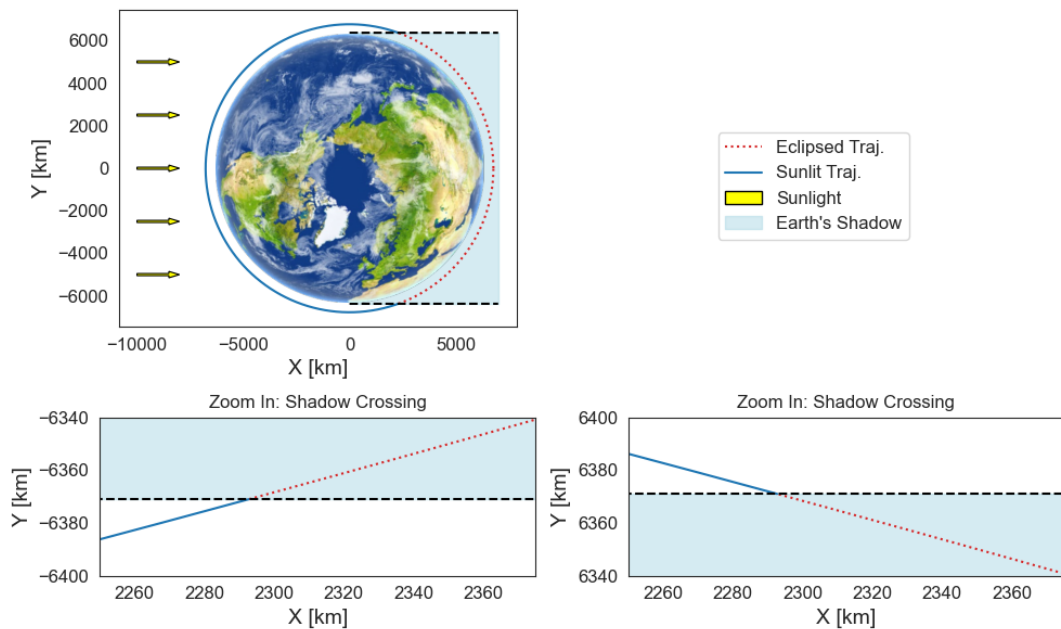
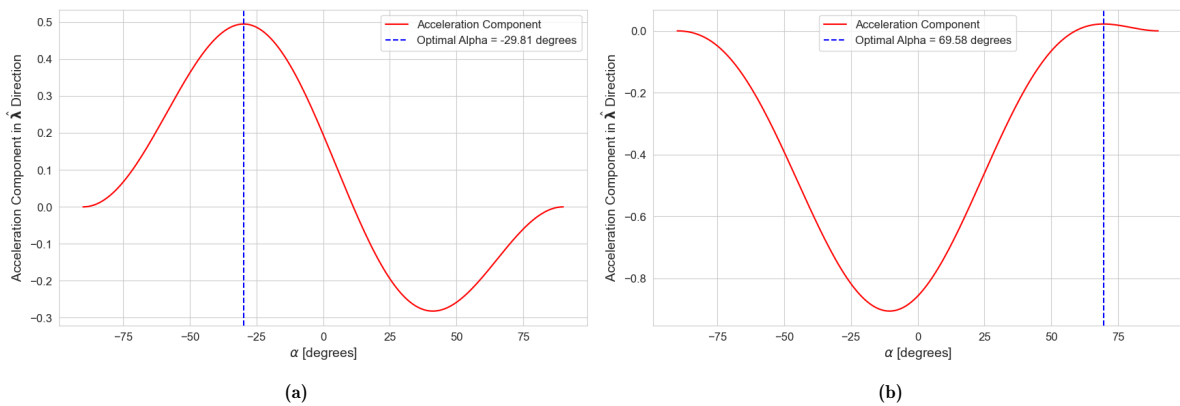


Figure A4: Keplerian orbit around Earth for Verification of Shadow Model

## A.4. Locally Optimal Steering

InTrance was initially designed to optimise Sun-centred missions. To allow for planet-centred missions, the calculation of the locally optimal steering had to be updated. To verify the implemented algorithm, the SRP acceleration in the direction of different  $\hat{\lambda}$  for various cone angles was calculated and the behaviour of the resulting acceleration components was observed. With the equations for the locally optimal steering, the optimal cone angle which maximises the acceleration component along  $\hat{\lambda}$  was calculated. By plotting the acceleration as a function of the cone angle, it can be visually verified that the optimal cone angle corresponds to the peak of the acceleration curve.

It is sufficient to plot a 2D case, as the sail acceleration magnitude does not depend on the sail clock angle. Figure A5 shows the acceleration component in the direction of two different  $\hat{\lambda}$ . The dashed line indicates the optimal cone angle, corresponding to the maximum point on the curve, verifying the accuracy of the implemented algorithm.



**Figure A5:** Acceleration components in the direction of a)  $\hat{\lambda} = [1, -5]$  and b)  $\hat{\lambda} = [-5, 3]$  and their respective optimal cone angles

## A.5. Trajectory Optimisation

In this thesis, two trajectory types are optimised: hold and homing trajectories. Following, the verification of both trajectory types is elaborated.

### Homing Trajectory

To verify the optimisation of the homing trajectory, a control profile was propagated in Python over two revolutions, which maximises the increase in the semi-major axis over time by maximising the solar radiation pressure force along the velocity vector. The final state from this propagation was then used as the target state for optimisation with InTrance, with the simulation time extended to four revolutions. To minimise the transfer time to this state, the same control profile needed to be followed. The optimal control profile and the profile optimised by InTrance are shown in Figure A6. It can be seen that InTrance successfully identifies the same control profile, demonstrating its capability to optimise homing trajectories.

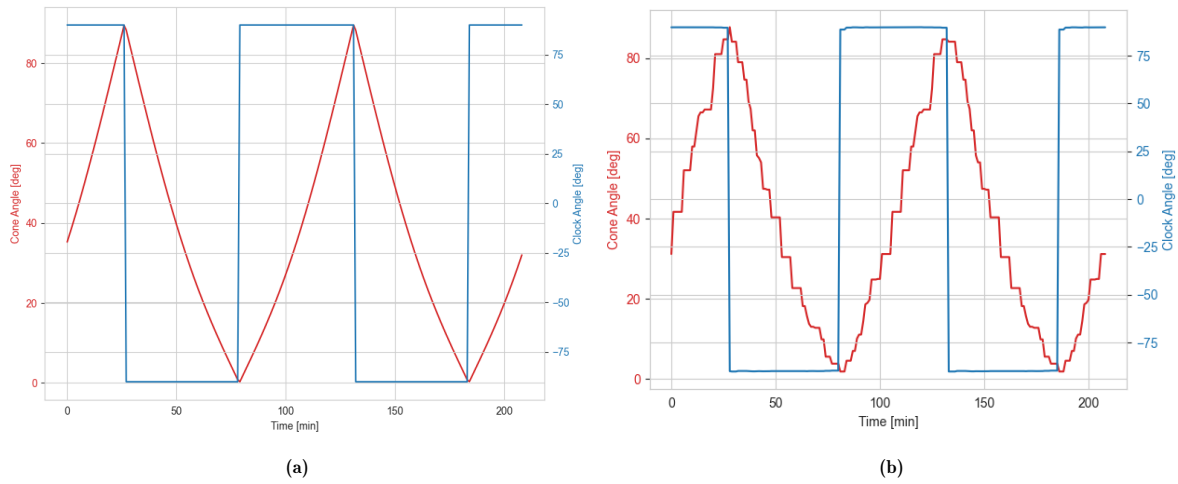


**Figure A6:** Comparing the a) optimal control profile for an optimal semi-major axis raising trajectory to b) the control optimised by InTrance

## Hold Trajectory

To verify the optimisation of the hold trajectory, the hold area was reduced to encompass an elliptical Keplerian orbit around the target narrowly. The initial state of the spacecraft was set in this elliptical orbit. To maximise the time spent within the hold area, the sail needed to maintain an edge-wise orientation to the Sun, thereby minimising the solar radiation pressure force and ensuring adherence to the Keplerian orbit, which required a constant cone angle of  $\alpha = 90^\circ$ .

The resulting control profile is shown in Figure A7. It can be seen that the sail maintains a constant cone angle of  $\alpha = 90^\circ$ , remaining edge-wise to the Sun. Additionally, because the sail does not experience a solar radiation pressure force due to its edge-wise attitude, variations in the clock angle have no effect on the trajectory. Therefore, it can be concluded that InTrance successfully identifies an optimal solution, demonstrating its capability to optimise hold trajectories.

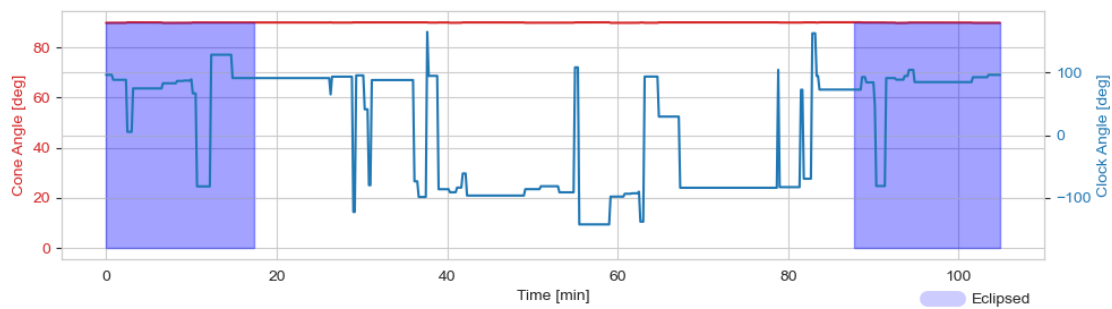


**Figure A7:** Resulting sail attitude of hold trajectory for verification

## Parameter Tuning

The optimal NC input set is anticipated to be problem-dependent. Effective parameter tuning is critical to optimising the performance of the ENC, as it directly affects the efficiency and success of the trajectory optimisation process. The choice of the input set can significantly influence search space exploration, convergence rate, and final solution quality. Identifying the best input set out of the 17

available combinations is crucial for achieving precise and efficient trajectory optimisation for both hold and homing trajectories.

Because the population of the ENC for the optimisation process is initialised randomly, the results can depend on the specific seed used. Five runs are conducted using different seeds to properly assess the robustness of each input set. This approach ensures that the observed performance is not an artefact of a particular random initialisation but rather reflects the general effectiveness of the input set under varying conditions. To determine the optimal input set, the search and convergence behaviour across all combinations is evaluated. The final state's accuracy, measured by how closely the optimiser can approach the targeted state, is also analysed for homing trajectory optimisation.

The assessment of search behaviour involves evaluating the frequency of terminal constraint satisfaction during search space scan epochs essentially, how often the terminal constraint is met during the ten initial search space scans. For homing trajectories, this is quantified by the final distance and relative velocity to the target. In contrast, the hold trajectory is based on the maximum ToF inside the target area. Each search space scan involves exploring the initial hypercube to identify an optimal steering strategy before narrowing the search space. The initial population is initialised at random for each scan to enhance diversity. A higher frequency of terminal constraint satisfaction across scans indicates a superior NC input set, suggesting that the input set effectively guides the search toward viable solutions.

Convergence behaviours are evaluated by determining the number of reproductions required for the solution to converge, leading to the termination of optimisation. This assessment provides insight into the efficiency of different input sets in guiding the optimisation process toward an optimal solution. The quality of the homing trajectory optimisation is further assessed by examining the final distance and relative velocity to the targeted state. A closer final state to the target indicates a more effective NC input set. To assess robustness, each input set is tested with five different seeds due to the stochastic nature of the optimisation process. This comprehensive analysis of search behaviour, convergence, and final state quality ensures the identification of the most effective input set for homing trajectory optimisation.

The respective validation cases for each trajectory type are used. The configurations for InTrance, the EA, the NC, the SC and the Simulation are shown in Section B.1, Section B.2, Section B.3, Section B.5 and Section B.4, respectively. These settings have been demonstrated to produce reliable results (Dachwald, 2005).

The following abbreviations are used for the input types:

1. State of the Chaser:
  - GCI Frame: C
  - Co-Moving Frame: M
2. Targeted State:
  - Co-Moving Frame: T
3. Sun-Sail Unit Vector in the Co-Moving Frame: S
4. Eclipse Factor: E

### Homing Trajectory

To determine the optimal input set for homing trajectory optimisation, the validation case described in Section A.5 is used. To assess the results' robustness and consistency, each input set is run for five different seeds.

Table A4 presents the results of the input set analysis for homing trajectory optimisation. It can be seen that input sets with a higher average frequency of meeting the terminal constraint during search space scan epochs generally exhibit lower reproduction counts, indicating faster convergence. For instance, input sets like CMTE (26 738 reproductions) and CMS (27 755 reproductions) demonstrate efficient convergence with frequencies of 5.2 and 4.8, respectively. Conversely, input sets with low frequencies, or those that never meet the terminal constraint during search space scans at all, tend to have significantly higher reproduction counts, such as COS (97,757 reproductions) and COTES (95,257 reproductions).

Input Set	Average of Five Runs				Std. Dev.		Best		Successful Seeds
	Rep.	Freq.	$\Delta r_f$ [m]	$\Delta v_f$ [m/s]	$\Delta r_f$ [m]	$\Delta v_f$ [m/s]	$\Delta r_f$ [m]	$\Delta v_f$ [m/s]	
C	87875	0.0	26.2	10.0e-3	0.212	15.5e-9	25.8	10.0e-3	0
CM	29179	4.6	0.699	349e-6	0.288	144e-6	0.293	146e-6	5
CME	30858	4.6	0.938	469e-6	0.431	215e-6	0.320	160e-6	5
CMES	28704	4.8	1.07	533e-6	0.818	409e-6	0.450	225e-6	5
CMS	27755	4.8	1.43	713e-6	2.01	1.01e-3	0.308	154e-6	5
CMT	35855	3.6	1.71	853e-6	1.87	937e-6	0.291	146e-6	5
CMTE	26738	5.2	1.13	567e-6	0.849	424e-6	0.401	200e-6	5
CMTES	32836	3.6	0.545	273e-6	0.268	134e-6	0.329	165e-6	5
CMTS	31848	4.2	0.961	480e-6	0.406	203e-6	0.336	168e-6	5
M	74485	0.0	21.6	9.77e-3	2.52	315e-6	18.4	9.21e-3	2
ME	72515	0.2	19.5	9.26e-3	3.17	1.11e-3	14.3	7.14e-3	2
MES	83647	0.0	22.7	9.92e-3	2.55	111e-6	19.4	9.72e-3	2
MS	97757	0.2	20.6	9.46e-3	4.00	491e-6	17.4	8.71e-3	3
MT	72038	0.0	25.1	9.91e-3	3.76	172e-6	19.1	9.57e-3	1
MTE	82577	0.0	24.7	10.0e-3	2.43	4.00e-9	22.3	10.0e-3	0
MTES	94648	0.0	23.3	10.0e-3	1.46	48.0e-9	20.9	10.0e-3	0
COTS	81107	0.0	25.0	9.86e-3	3.92	286e-6	18.6	9.29e-3	1

**Table A4:** Analysis of input sets for homing trajectory optimisation across five runs

A clear distinction is observed between input sets using the state of the chaser in the GCI frame (C) and those that do not. All input sets using the chaser's state in the GCI frame can meet the final constraint for all five runs during the optimisation process, except for the input set C. Input sets that do not use the chaser's state in the GCI frame meet the final constraint less frequently, with sets like MTE and MTES never able to reach the terminal constraints. This suggests a performance advantage for sets using the chaser's state in the GCI frame, as they achieve lower final distances and relative velocities to the target state. The superior performance of these input sets can be attributed to the calculation of  $\hat{\lambda}$ , which is derived directly from the NCs output in the GCI frame. As described in subsection 2.1.2, the solar sail's ideal cone and clock angles are calculated based on  $\hat{\lambda}$ . Thus, providing the NC with the chaser's state information in the GCI frame enhances its learning and decision-making capabilities, allowing it to more effectively determine the optimal sail attitude. The poor performance of input set C can be attributed to its lack of information about the chaser in the co-moving frame, which is essential for calculating the fitness based on the distance and relative velocity to the targeted state in that frame.

The best-performing input sets with the lowest average final distance and velocity are:

- CMTES ( $\Delta r_f = 0.545$  m and  $\Delta v_f = 273e-6$  m/s)
- CM ( $\Delta r_f = 0.699$  m and  $\Delta v_f = 349e-6$  m/s)
- CME ( $\Delta r_f = 0.938$  m and  $\Delta v_f = 469e-6$  m/s)

However, the input set CME has a higher standard deviation in the final distance and relative velocity than the other two, indicating less consistency in performance. The best solution is found with input set CMT ( $\Delta r_f = 0.291$  m and  $\Delta v_f = 146 \times 10^{-6}$  m/s). However, this input set exhibits a large standard deviation for both final distance and relative velocity, indicating a lack of robustness. Notably, for all input sets, the best final distance and relative velocity for each input set are achieved using the same seed, although the seed varies between different input sets. For example, for input set CM, the best results are from seed 2, while for CME, the best results are from seed 5.

Overall, the analysis identifies CMTES and CM as potentially optimal input sets due to their frequent satisfaction of the terminal constraint during search space scans, low reproduction counts, and overall comparatively good final distances and relative velocities to the targeted state. These sets demonstrate a balanced combination of effective convergence and precision.

### Hold Trajectory

To determine the optimal input set for hold trajectory optimisation, the verification case as shown in Figure A.5 is used. To assess the results' robustness and consistency, each input set is run for five different seeds.

Table A5 displays the results of the input set analysis for hold trajectory optimisation. It can be seen that, as before, during the homing trajectory optimisation, the input sets that frequently satisfy the terminal constraint during search space scan epochs tend to converge with fewer reproductions. For instance, the input set C stands out, achieving the terminal constraint with an average of 8.2 times out of a possible 10 search space scan epochs and requiring the fewest average reproductions (14 299.6) to converge. All other input sets show a reproduction number that is 1.5 to 2.5 times higher, with a lower frequency of satisfying the terminal constraints.

Interestingly, there is no significant performance advantage for input sets incorporating the chaser's state in the GCI frame, as observed in the homing trajectory optimisation. While input set C performs well, others, like CME and CMT, do not show comparable results. This suggests that in hold trajectory optimisation, the chaser's state information in the GCI frame does not provide a consistent advantage. The variability in results implies that other factors, such as the complexity of the trajectory or the specific initial conditions, may have a more significant impact on optimisation performance. It is also noteworthy that even input sets which did not meet the terminal constraint during the initial search space scan often satisfied it after one to three epochs during the first downsizing of the search space. This suggests that while immediate constraint satisfaction in the initial scans is beneficial, subsequent optimisation processes can still achieve successful convergence.

In conclusion, the results of the hold trajectory optimisation indicate that while some input sets like C are effective in meeting the terminal constraint and converging quickly, there is less overall consistency in performance trends compared to homing trajectory optimisation. This suggests a more complex interaction between input set composition and optimisation efficiency.

Input Set	Average of Five Runs	
	Rep.	Freq.
C	14299.6	8.20
CM	34280.6	2.40
CME	31781.8	2.00
CMES	34120.8	2.40
CMS	26832.2	1.40
CMT	26283.8	1.40
CMTE	30203.8	0.80
CMTES	30036.6	1.20
CMTS	27994.0	0.40
M	29404.0	2.60
ME	30827.4	2.40
MES	28314.2	2.60
MS	28315.4	2.60
MT	32716.2	2.40
MTE	34726.0	1.40
MTES	33059.4	1.80
MTS	31673.2	1.40

**Table A5:** Analysis of input sets for hold trajectory optimisation across five runs

## A.6. Accuracy Assessment and Step Size Selection for CW Equations

The ClohessyWiltshire equations describe a simplified model of orbital relative motion in which the target is in a circular orbit. They are a linearisation of the two-body dynamics and thus provide only an approximate solution (Curtis, 2013). This approximation introduces inaccuracies that grow as the spacecraft moves farther from the origin. To assess the precision of the CW equations, a baseline trajectory is computed using the RK45 ODE solver with a small step size of  $h = 0.05$  s. The position differences between the RK45 solution and the CW solution are then evaluated for various step sizes of the CW propagator. The results are shown in Figure A8. It can be seen that increasing the step size leads to greater inaccuracies in the simulation results. Since high precision is not critical for the purposes of this analysis, a step size of  $h = 10$  s is selected for all simulations. This choice minimises the runtime while still providing reasonable accuracy.

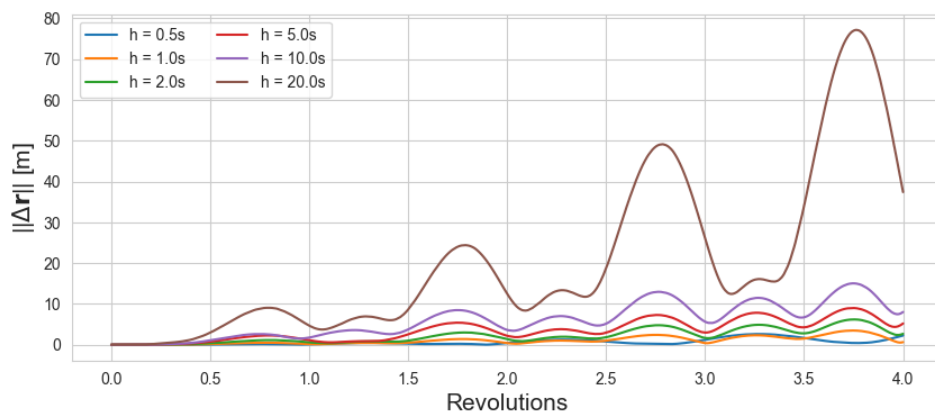


**Figure A8:** Position difference  $\|\Delta\mathbf{r}\|$  between the 2-body and Clohessy-Wiltshire propagations over 4 orbital revolutions for different step sizes.

## A.7. Runtime Efficiency Comparison of Propagation Methods

In optimisation processes, it is important to consider the computational effort required by simulations to reduce runtime. The runtime of propagating the CW equations is compared to that of propagating the two-body dynamics using the RK45 integrator. For this comparison, a spacecraft is propagated for three revolutions with a semi-major axis of  $a = 7371$  km (ToF = 18 892 sec) with step sizes of  $h = 1$  s, 2 s, 5 s, 10 s, 15 s, 20 s, 30 s, 40 s, 50 s and 100 s. To ensure that the results are robust and minimise the impact of random fluctuations, each simulation is run ten times, and the average runtime is computed. The results are shown in Figure A9. The CW equation has five to six times lower runtime than the RK45 integrator. The significant reduction in computational effort makes the CW equations ideal for computationally constrained scenarios where precision is less essential.

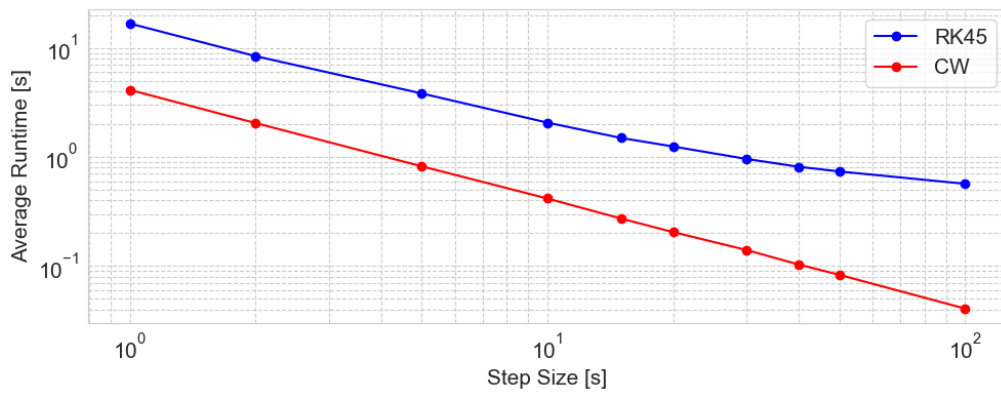


**Figure A9:** Average runtime comparison between the RK45 integrator for two-body dynamics and the Clohessy-Wiltshire (CW) equations across various step sizes.

# B

## InTrance

This appendix provides the configuration files used in InTrance. These files contain all the necessary parameters required to perform the optimisation for hold and homing trajectories. The parameters labelled with "TBD" are problem-dependent and are specified in the analysis sections.

### B.1. InTrance Configuration

<b>Parameter</b>	<b>Value</b>
RANDOM_SEED	1
COMMAND	optimize NC
SIM_PARAM_FILE	input_SIM.sim
SC_PARAM_FILE	input_SC.sim
NC_PARAM_FILE	input_NC.sim
EA_PARAM_FILE	input_EA.sim
COLDSTART	YES

### B.2. Evolutionary Algorithm Configuration

<b>Parameter</b>	<b>Value</b>
SEARCH_SPACE_HYPERCUBE_SIZE	1.0
HYPERCUBE_SHRINKING_FACTOR	0.5
POPULATION_SIZE	50
SEARCH_SCAN_EPOCHS	10
FITNESS_FUNCTION_TYPE	J_OR
CHROMOSOME_MUTATION_PROBABILITY	0.8
SELECTION_PRESSURE_ON_TIME	0.0
HYPERCUBE_UPPER_LIMIT	1.0e-4

### B.3. Neurocontroller Configuration

Parameter	Value
SC_TYPE	solar sail
NORMALISE_NC_INPUT	no
INCLUDE_GA_NEURONS	TBD
CARTESIAN_INPUT	TBD
COMOVING_INPUT	TBD
COMOVING_TARGETED_INPUT	TBD
SUN_VECTOR_INPUT	TBD
SHADOW_INPUT	TBD
NC_INPUT	full
HIDDEN_LAYERS	1
NEURONS_IN_HIDDEN_LAYER1	30
NC_OUTPUT	direct
TRANSFER_FUNCTION	sigmoid
SPHERICAL_INPUT	no
ORBITAL_ELEMENTS_INPUT	no

### B.4. Simulation Configuration

Parameter	Value
SIM_START_TIME_MIN	51544.5
SIM_START_TIME_MAX	51544.5
NUM_REVOLUTIONS	TBD
STEP_SIZE	10
INITIAL_CENTRAL_BODY	earth
INITIAL_STATE	comoving
INITIAL_BODY_NAME	earth
INITIAL_COMOV_POS_X	TBD
INITIAL_COMOV_POS_Y	TBD
INITIAL_COMOV_POS_Z	TBD
INITIAL_COMOV_VEL_X	TBD
INITIAL_COMOV_VEL_Y	TBD
INITIAL_COMOV_VEL_Z	TBD
TARGET_STATE	TBD
TARGETED_HOLD_TRAJECTORY_DATA	targeted_hold_trajectory_data.csv
OPTIMISE_TARGETED_ATTITUDE	TRUE
TARGET_SEMIMAJOR_AXIS	7371000.0
TARGET_ECCENTRICITY	0.0
TARGET_INCLINATION	0.0
TARGET_LONGITUDE_OF_NODE	0.0
TARGET_ARGUMENT_OF_PERICENTER	0.0
TARGET_MEAN_ANOMALY	0.0
TARGETED_COMOV_POS_X	0.0
TARGETED_COMOV_POS_Y	0.0
TARGETED_COMOV_POS_Z	0.0

*Continued on next page*

<b>Parameter</b>	<b>Value</b>
TARGETED_COMOV_VEL_X	0.0
TARGETED_COMOV_VEL_Y	0.0
TARGETED_COMOV_VEL_Z	0.0
TARGETED_DIST_MAX	20.0
TARGETED_RELVEL_MAX	0.01
INNER_A	TBD
INNER_B	TBD
INNER_C	TBD
OUTER_A	TBD
OUTER_B	TBD
OUTER_C	TBD
INTEGRATOR	CW
MAX_RELATIVE_ERROR	1e-6
MAX_ABSOLUTE_ERROR	1e-6

## B.5. Spacecraft Configuration

<b>Parameter</b>	<b>Value</b>
SC_TYPE	solar sail
LIGHTNESS_NUMBER	7.7E-3
OPTICAL_SAIL_MODEL	ideal sail
MAX_CONE_ANGLE	TBD
MIN_CLOCK_ANGLE	TBD
MAX_CLOCK_ANGLE	TBD
MAX_TURNING_RATE	TBD

## Additional Figures and Tables

### C.1. Characteristics of Solar Sail Relative Motion

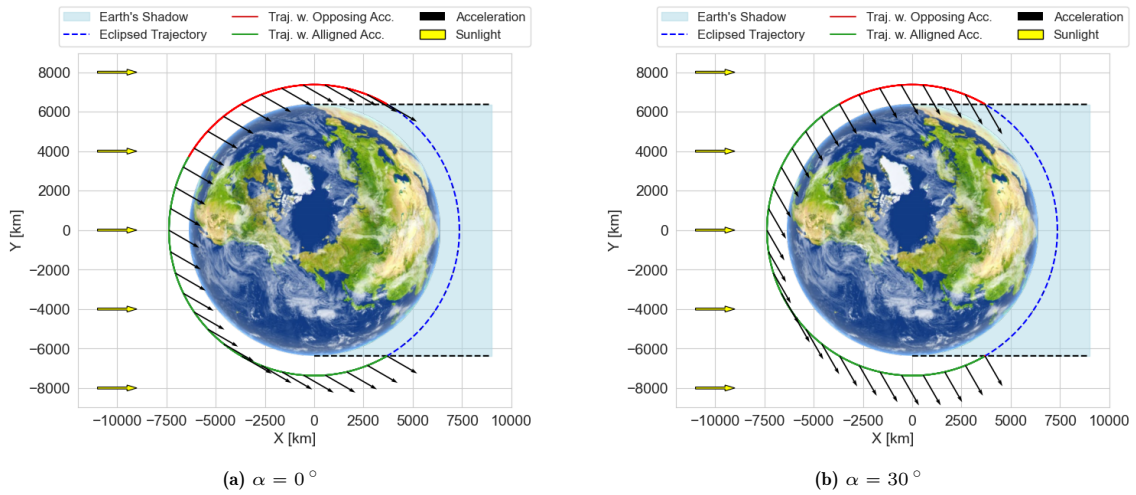


**Figure C1:** Trajectory for a constant sail attitude with  $\delta = -90^\circ$ , highlighting the part where the acceleration vector has a component opposing the velocity vector and where it aligns with the velocity vector for a)  $\alpha = 30^\circ$ ; b)  $\alpha = 60^\circ$

### C.2. Hold Trajectory Analysis

State	$t$ [s]	$x_M$ [m]	$y_M$ [m]	$z_M$ [m]	$dx_M$ [m/s]	$dy_M$ [m/s]	$dz_M$ [m/s]	$\alpha$ [°]	$\delta$ [°]
1	1340	-455.94	3830.23	0.21	1.911	0.910	0.001	70	11.8
2	3520	1829.76	-1424.81	8.93	-0.718	-3.654	0.003	70	-5.9
3	3110	1964.44	150.47	7.36	0.070	-3.923	0.004	70	12.4

**Table C1:** Initial states and corresponding sail attitude laying on the hold trajectory of Case 1 as seen in Table 2 with a maximum cone angle of  $70^\circ$ .

### C.3. Homing Trajectory Analysis

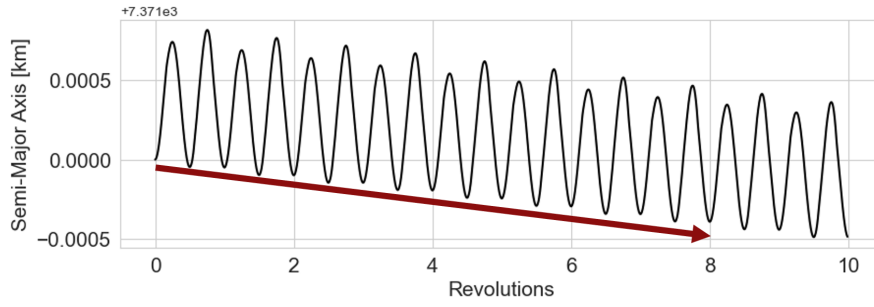


Figure C2: Change of semi-major of the optimised trajectory of test case for leading/trailing hold trajectory.

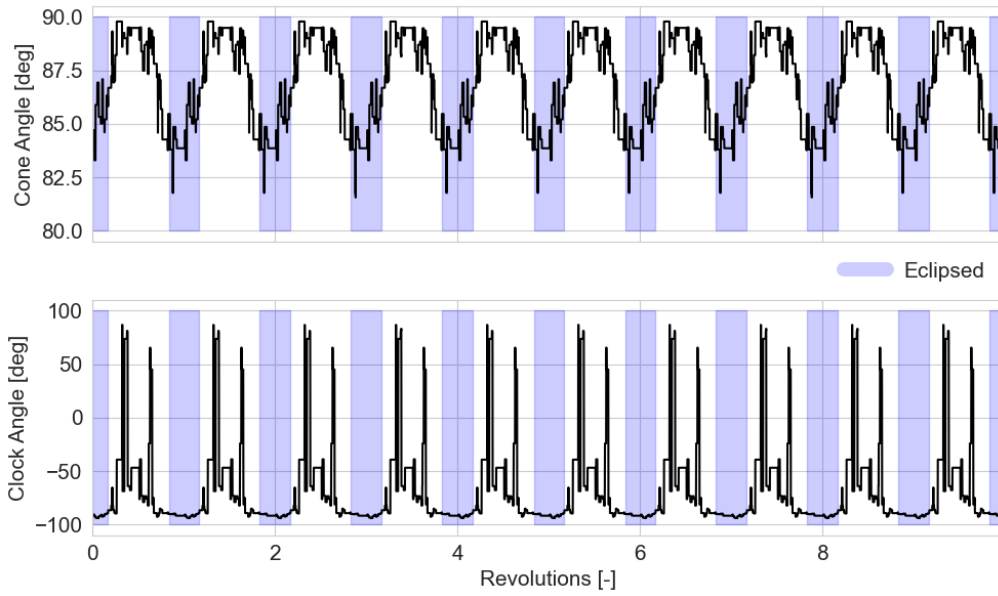


Figure C3: Optimised control profile of test case for encircling hold trajectory.

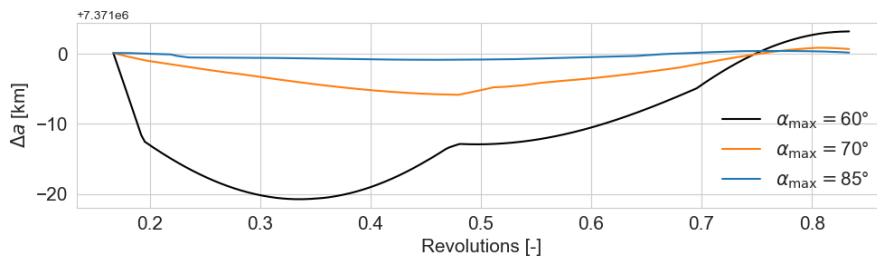
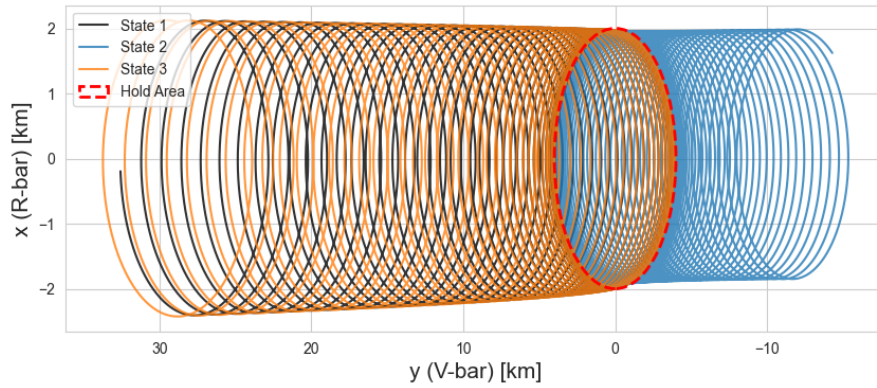


Figure C4: Change of semi-major of the optimised trajectory or negative clock angle restriction for maximum cone angles of  $\alpha_{\max} = 65^\circ$ ,  $75^\circ$  and  $85^\circ$  for case 1, as shown in Table 4.

State	$t$ [s]	$x_M$ [m]	$y_M$ [m]	$z_M$ [m]	$dx_M$ [m/s]	$dy_M$ [m/s]	$dz_M$ [m/s]	$\alpha$ [°]	$\delta$ [°]
1	1210	-238.180	865.230	0.001	0.432	0.475	0.000	60	1
2	3230	487.102	-78.226	7.906	-0.046	-0.975	0.004	60	1
3	3840	373.231	-589.419	14.315	-0.315	-0.748	0.003	60	14

Table C2: Initial conditions and corresponding sail attitudes for safety analysis of trajectories under a positive clock angle profile, showing the effect of different sail attitudes on drift in the V-bar direction.



**Figure C5:** Trajectories for a constant sail attitude with the initial state laying on the hold trajectory, as shown in Table C1

State	$t$ [s]	$x_M$ [m]	$y_M$ [m]	$z_M$ [m]	$dx_M$ [m/s]	$dy_M$ [m/s]	$dz_M$ [m/s]	$\alpha$ [°]	$\delta$ [°]
1	1340	-114.555	960.705	-0.020	0.479	0.228	-0.001	70	-172
2	1780	99.973	966.660	-0.765	0.480	-0.201	-0.003	70	-1
3	3110	487.220	42.549	1.030	0.013	-0.975	0.004	70	-147

**Table C3:** Initial conditions and corresponding sail attitudes for safety analysis of trajectories under a negative clock angle profile, showing the effect of different sail attitudes on drift in the V-bar direction.

Max. ToF [Rev.]	Targeted State	Final Error Met	ToF [h]	$\Delta r_f$ [m]	$\Delta v_f$ [m/s]	Final rel. Attitude [°]
5 (8.7h)	3	<b>X</b>	7.31	46.99	0.011	70.8
10 (17.5h)	4	<b>X</b>	16.05	49.49	0.009	97.7
20 (34.9h)	1	<b>X</b>	43.58	20.38	0.01	50.0
30 (52.45h)	10	<b>✓</b>	51.54	18.48	0.0074	19.99
35 (61.2h)	3	<b>✓</b>	47.44	16.46	0.0034	46.39

**Table C4:** Results of the homing trajectory optimisation for an unrestricted solar sail for different maximum simulation times.